STUDY OF FREEZE-CAST POROUS SILICA NANOPARTICLE-BASED COMPOSITES

WENLE LI

Dissertation submitted to the faculty of the Virginia Polytechnic Institute and State University in partial fulfillment of the requirements for the degree of

Doctor of Philosophy
In
Materials Science and Engineering

Kathy Lu, Committee Chair
John Y. Walz, Co-Chair
Guoquan Lu
William Ducker

July 02, 2012
Blacksburg, VA

Keywords: Silica, Kaolinite, Freeze casting, Porous microstructure, Strength

Study of Freeze-Cast Porous Silica Nanoparticle-Based Composites

Wenle Li

ABSTRACT

Porous silica-based nanocomposites are promising ceramics, as they exhibit high specific surface area, highly porous network, and a surface that can be easily functionalized. This dissertation describes the results of a study on the formation and properties of porous silica nanoparticle-based composites, using techniques of freeze casting and sintering. Kaolinite platelets and silica nanorods were added into the nanoparticle system, and their effects on modifying the porous microstructures and physical properties were investigated.

During freeze casting, homogeneous microstructures with highly interconnected porosity are fabricated. Kaolinite addition results in large and more interconnected pores, while added silica nanorods cause a pore morphology evolution from circular to elongated spherical pores with increasing aspect ratio. The specific surface areas (area/mass) of the particles are conserved during freeze casting and values for the resulting composites can be accurately predicted using the area and mass of the components assuming conservation of area. Both kaolinite platelets and silica nanorods effectively improved the strength of the freeze cast green composites as they distribute any applied stress over a larger portion of the sample.

Upon sintering, added kaolinite is found to modify the sintering behavior of the silica nanoparticles and a transitioning interfacial phase is identified when sintering temperature is above 1250°C. This new phase contributes to the further enhancement of strength and this strengthening effect depends on composition and initial solids loading. After sintering at 1250°C for 1 h, a ceramic containing 10 vol% kaolinite and 8 vol% silica has a maximum strength while maintaining a ~69% porosity. The kaolinite-silica composites with lower solids loading exhibit faster sintering (e.g. larger shrinkage, more extensive thickening of the pore walls), which, in turn, results in a rapid increase in mechanical strength.

Based on the understanding of the composite properties and the underlying principles, a novel method for creating nanocomposites with precisely controllable specific surface area is developed. With repeated nanoparticle suspension infiltration, freeze drying, and sintering, the specific surface area can be varied from less than one to well over 100 m^2/g, demonstrating potential application as liquid membranes.

This work is dedicated to the memory of my grandparents, who brought me up and supported me in their lives but cannot join this celebration.

Zhenguo Yang (Maternal), 12/1929 to 09/1998

Xiumin Zhao (Maternal) 1933 to 01/1990

Yuzhu Ma (Paternal) 09/1935 to 12/2009

This dissertation is also dedicated to my grandfather (Paternal), Xuezeng Li, who continuously supports me both spiritually and physically.

ACKNOWLEDGEMENTS

First, I would like to express my deeply appreciation to my parents, grandparents, and all other family members. They raised me up and continuously support me for more than twenty-five years, which brought me to who I am today. Studying abroad for three years, I owe them a lot for not being able to keep together. I regret with all my life for not being around when my grandma passed away.

I acknowledge the great emotional support from my girlfriend, Yating Chai, and her family. Her love is the strength that keeps me moving on. It is she who always being with me, especially during the hard times. She has been helping me make the most important decisions, since we met each other as undergraduates.

Thanks Virginia Tech, she provides me a wonderful place for both academic work and personal life. More important, here I got the opportunity to work with Dr. Kathy Lu and Dr. John Y. Walz, the most important two persons for my graduate study. It is a great asset for me to work simultaneously with two professors. Their complementary academic styles made me grew rapidly in research skills such as experimental problem solving, scientific paper writing, and literature search. Their support, patience, and guidance in the past three years are greatly appreciated. I would also like to thanks Dr. Guoquan Lu and Dr. William Ducker for kindly being my advisory committee members. They not only directed me in specific scientific problems, but also advised me in career planning.

The financial support from National Science Foundation under grant CBET-0827246, and the American Chemical Society Petroleum Research Fund, grant 47421-AC9 is greatly acknowledged. Assistance from the Nanoscale Characterization and Fabrication Laboratory of Virginia Tech is appreciated, especially to Stephen McCartney and John McIntosh.

Appreciations are also sent to other professors and my colleagues at Virginia Tech: Dr. William T. Reynolds, Jr., David Berry, Bo Chen, Dr. Tongan Jin, Mac McCord III, Dr. Scott Case, Dr. Richey Davis, Gregory James, Yuan Zhou, David Herman, Dr. Stephen Martin, Dr. Abby Whittington, Dr. Junbo Hou, Zhipeng Tian, Dr. Manoj Mahapatra, Yuchang Wu, Shunxi Ji, Heather Grandelli, Margaret Anderson, Dr. Guangyin Lei, Yongxuan Liang, Andrew Kulp, Dr. Carlos Suchicital, Dr. Niven Monsegue, Zhenbo Xia, Menghui Li, and Francisco Guzman.

Statement:

Most of the contents in this dissertation were published or will be published in scientific journals. In referencing this work, readers are asked to cite the journals.

TABLE OF CONTENTS

LIST OF FIGURES

LIST OF TABLES

CHAPTER 1. INTRODUCTION

1.1 Motivation and objectives

In the past decades, fabrication, characterization, and application of porous materials have drawn considerable attention. While traditional uses of such materials as membranes, catalyst supports and adsorbents remain common,[1-3] recent research has led to a much broader range of applications, such as in drug delivery, tissue engineering, energy storage, and microelectronics.[4-10]

Not surprisingly, a large number of novel synthesis procedures have been developed to meet this growing interest. Some examples include micro-emulsion methods, nanocasting, direct foaming, freeze casting and sacrificial templating.[11-14] While each of these methods is effective, many also suffer from one or more disadvantages, such as the requirement of expensive reagents, large amounts of organic solvents, or complicated fabrication procedures. In addition, as stated by Deville et al.,[15] one of the primary challenges in synthesizing porous materials is obtaining high porosity without compromising on strength.

The aim of this dissertation is to investigate the fabrication and properties of silica-nanoparticle-based porous composite, using the techniques of freeze casting and sintering. The system involves monodispersed silica nanospheres with an anisotropic particle additive (i.e. either kaolinite platelet or silica nanorod). This research was conducted because: first, porous silica-based materials are promising ceramics, as they exhibit high specific surface area, highly porous network, and a surface that can be easily functionalized; second, this binary system exhibits a synergistic bonding effect between the two species that could greatly improve the resulting strength for both the green and sintered samples without compromising the overall porosity; third, freeze casting is a versatile technique that is capable of fabricating a wide range of pore characteristics and applicable to most ceramics;[11] fourth, a much better understanding of both the fundamental principles guiding the freeze casting and subsequent sintering processes, and the composition-dependent properties for this silica-nanoparticle-based composite must be achieved before potential applications can be realized.

In this work, three main tasks were conducted. The first task was to build an understanding of the freeze casting and sintering behaviors for the silica-nanoparticle-based

composites. Specifically, the microstructure, porosity, specific surface area, and strength evolutions of the porous composites along with the freeze casting and sintering were investigated. The principle mechanisms governing these fabricating processes were proposed.

The second task was to evaluate and control the properties of the porous composites. The relationships between the relevant factors and the resulting properties were established by studying factors such as composition, solids loading, and sintering temperature. Afterwards, a new technique, suspension infiltration, was designed and carried out to better control the properties.

The third task was to examine the effects of anisotropic particle addition on the fabricating processes and the corresponding properties. In particular, kaolinite platelets and silica nanorods were exploited in the fabrication of the composites. These second phases were capable of adjusting the microstructure and improving the properties (e.g. strength) of the resulting composites.

The accomplishment of the above three tasks established a solid understanding of this novel system. Since specific methods are pointed out for the improvement of properties, the fabricated porous materials are promising in a number of applications. For example, with designed initial solids loading, sintering condition, and suspension infiltration, the major pore size can be controlled to provide a certain cutting off size and permeability, which are critical for separation membranes. The repeated suspension infiltration can improve the specific surface area to hundreds of square meters per gram, which is desirable for catalyst supports, adsorbents, and surface-functionalized membranes. Also, the well-defined porous microstructure and porosity can effectively modify the optical, electrical, and mechanical properties of these composites, and broaden the potential applications to fields as optical device, microelectronics, and biotechnology, respectively. Furthermore, one of the attractive features of this work is that the interaction during freeze casting is not believed to be material specific. The established understandings and the proposed mechanisms should also be applicable to many other materials/composites.

1.2 Overview

The dissertation is composed of 10 chapters, which can also be viewed as 5 parts based on the contents.

The first part includes Chapters 1 and 2. Following the Introduction (Chapter 1), Chapter 2 gives a literature review regarding the materials (i.e. silica and kaolinite) involved and the applied techniques (i.e. freeze casting and sintering). The potential applications of the porous materials are also pointed out.

The second part includes Chapters 3 and 4, focusing on the fabrication of the porous composite. In this part, the fundamentals for freeze casting (Chapter 3) and sintering (Chapter 4) of the kaolinite-silica system are discussed.

The third part includes Chapters 5 to 7. This part concentrates on analyzing the properties of the porous composite, as well as the corresponding influencing factors. Specifically, Chapter 5 elaborates the strength and porosity evolutions of the kaolinite-silica composite using the sintering temperature and composition; Chapter 6 discusses the solids loading effects on the properties of the same composite; and Chapter 7 introduces a suspension infiltration method for creating high surface area porous ceramic composites without loss of mechanical strength.

The fourth part is presented in Chapter 8. Unlike Chapters 3 to 7, this chapter focuses on a pure silica composite. With the addition of rod-like silica particles, the work describes in this chapter demonstrates a method of modifying the porous structure and improving the strength of a composite without compromising the porosity or altering the composition.

Part five includes Chapters 9 and 10. Chapter 9 provides a summary of the main points for this dissertation, and Chapter 10 indicates the directions for future work.

1.3 Contributions

This work makes contributions to both the understanding of fundamental principles and the control of the properties for the freeze casting and sintering of silica-nanoparticle-based binary porous composites.

1). Discovery of a novel porous nanocomposite.

The porous composites are made of silica nanospheres plus either kaolinite platelets or silica nanorods. All of the raw materials are common ceramic materials but the nanocomposite was previously not studied. In this novel composite, the characteristics of kaolinite are fully explored: the anisotropic shaped platelets are utilized to physically adjust the freeze casting behaviors and the corresponding properties; its thermal behaviors are exploited to modify the sintering of silica nanoparticles. On the

other hand, the recent achievements in synthesizing silica nanorods with fixed diameter and adjustable aspect ratio offer an opportunity to improve the strength of the porous silica without compromising the porosity and purity.

2). Understanding of the freeze casting behaviors for suspensions with gelled state and anisotropic particles.

Although the technique of freeze casting has been drawing increasing attention in the fabrication of porous ceramics, the study on freeze casting of a gelled suspension plus anisotropic particles is very limited.[11] In this work, the electrolyte-induced sol-to-gel transition offers an opportunity to improve the homogeneity of the 'suspension' along with the uniformity of the resulting porous microstructure without upgrading the freeze casting setup. The introduction of anisotropic particles (i.e. platelets and nanorods) to the suspension provides a first attempt to evaluate the effect of particle shape on the freeze casting behaviors.

3). Development of a novel method for creating porous ceramics with high specific surface area and high strength.

The approach involves infiltrating an aqueous suspension of silica nanoparticles into a scaffold that had been created by sintering a freeze-cast gel consisting of silica nanoparticles and kaolinite clay platelets. After infiltration, the liquid-filled samples are freeze-dried to remove the water while retaining a uniform distribution of nanoparticles, then subjected to a slight sintering to firmly bond the nanoparticles in place without altering their spherical shape. This method is simple and involves nothing more than water and nanoparticles. Altering the size and number of infiltrated nanoparticles allows precise control of the specific surface area of the resulting composite. In addition, it is shown that rather than weakening the composites, infiltrating the nanoparticles actually increases their mechanical strength.

CHAPTER 2. BACKGROUND

2.1 Experimental system

2.1.1 Silica nanoparticles

Silica has received considerable attention for decades in both academic studies and industrial applications. In general, any silicon-oxygen compounds with a central silicon atom surrounded by four oxygen atoms are recognized as "silica", including crystalline structures (e.g. quartz, tridymite, cristobalite, and etc.) and amorphous structures (e.g. short-, medium-, and long-range).[16]

The development of nanotechnology rejuvenated the investigation of silica and brought it to the frontier of the modern science.[17] Because of its tunable nano-size, larger surface area, well-defined surface properties, and chemical/thermal stabilities, silica nanoparticles are promising in many applications, including biocatalysis, bioseparation,[17] biosensor,[18] DNA/drug delivery,[19] and fluorescent materials for photonics and optoelectronics.[20] Synthetic methods, such as microemulsion,[21, 22] micelle,[22] flame spray pyrolysis,[23] and forced hydrolysis,[24] have been developed to prepare silica nanoparticles. In addition to nanospheres, silica nanoparticles with advanced features (e.g. mesoporous and core-shell silica nanoparticles[25-28]) have been created, which broadens the applications and improves the performances.

The recent achievement in synthesizing rod-like silica nanoparticles brought further opportunity in applications, such as separation membranes.[29-32] Kuijk *et al.* reported the fabrication of monodispersed silica nanorods with tunable aspect ratio.[31]

One characteristic of colloidal silica suspension is the salt-induced sol-to-gel transition. With proper concentrations of both silica nanoparticles and salt, the colloidal suspension gradually evolves to a solid-like material. Walz *et al.* reported that sufficient silica nanoparticles along with salt can be used to stabilize big particles (i.e. kaolinite platelets with micron size) with this unique gel formation.[33]

2.2.2 Kaolinite

2.2.2.1 Structure

Kaolinite is a naturally occurring clay with a chemical composition of $Al_2Si_2O_5(OH)_4$ and consists of hundreds of layers of covalently and hydrogen bonded alumina- and silica-like materials.[34] The crystal is comprised by alternative layers with one silicate tetrahedral sheet linked to one octahedral sheet of alumina octahedra through oxygen atoms (Fig. 2-1).[34,35] Generally, kaolinite exists in the form of disk-like hexagonally shaped particles,[35] and these platelets exist in "stacks" or as "books" with various degree of stacking regularity. These stacks are strongly bonded making them difficult to be delaminated. Natural synthesized kaolinite always has crystalline imperfections and is polydispersed. Kaolinite platelets are water dispersable and the surface charge of platelets depends on suspension pH when suspended in aqueous suspension. Experiments suggest that the platelet surfaces are negatively charged while the platelet edges are positively charged.[36] However, this conclusion is debatable as there were some uncertainties through these experiments.[37] The colloidal behaviors of kaolinite platelets depend on the suspension pH and second phase chemistry.

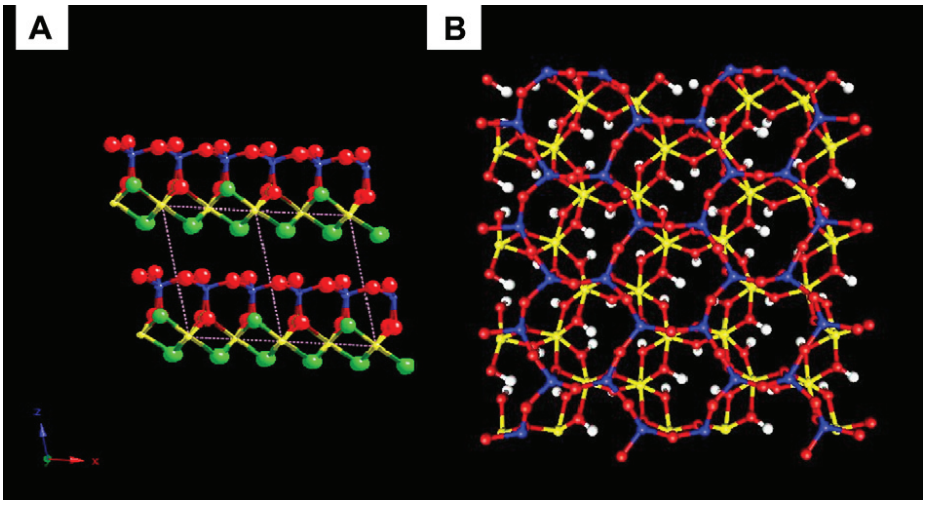

Fig. 2-1. Schematic illustration of kaolinite crystalline structure (A) side view, (B) top view of (001) surface. (Reprinted from *Journal of Colloid and Interface Science*, Vol 352/Issue 1 (2010), Gupta *et al*., Crystal lattice imaging of the silica and alumina faces of kaolinite using atomic force microscopy, Copyright (2012), with permission from Elsevier[35])

2.2.2.2 Thermal behavior

Upon sintering, kaolinite undergoes a series of phase transformations over a relatively broad temperature range and this thermal behavior has been extensively studied.[38, 39] Around 550°C, dehydroxylation or dehydration occurs with the formation of metakaolin (a complex amorphous structure with long range order) and continuous hydroxyl group (-OH) loss exists up to ~900°C.[40] Above 980°C, metakaolin transforms to a defective crystalline spinel phase ($Si_3Al_4O_{12}$), [35] which subsequently transforms into mullite at higher elevated temperatures.[41] Thanks to its crystal structure, disk-like shape, and thermal behaviors, kaolinite becomes a promising mineral clay. One of the emerging applications of kaolinite is modifying the sintering behavior and mechanical properties (e.g. hardness, strength, elastic properties) of ceramics. Along with other oxides (such as alumina,[42-45] nickel oxide[46]) and in novel sintering processes (microwave sintering,[47] tape-cast-sintering[48]), kaolinite is sintered to fabricate ceramics such as mullite and nickel aluminate spinel. Recently, the reinforcement effects of kaolinite in matrix materials, such as boron carbide,[49] have also been investigated.

2.2 Freeze casting of porous ceramics*

Porous ceramics exhibit a number of useful characteristics (e.g. low density, light weight, controllable porous microstructure, high specific surface area, thermal/chemical/mechanical stabilities) that are desirable in a wide range of applications, including separation filters, catalyst supports, drug carriers, gas distributors, insulators, and scaffolds for bio-applications.[10, 11, 51-55] Many fabrication techniques, such as sacrificial templating, direct foaming, extrusion, and freeze casting, have been developed to produce porous ceramics.[11, 12] Compared to other techniques, freeze casting is a promising method to fabricate porous ceramics with adjustable porous microstructures and component geometries as the resulting microstructures and properties can be effectively controlled by the dispersing medium, freezing conditions, suspension solids loading, and added additives. Freeze casting bases on physical fundamental principles that are shared by most ceramic systems, enabling a wide application of this technique.

* Section 2.2 was published in *International Materials Reviews 2012, **57**(1), 37-60*[50]

2.2.1 Processing principles

2.2.1.1 Experimental procedure

The tailorability of the freeze casting technique makes it capable of fabricating materials with dense, cellular, and lamellar microstructures. The original application of this technique was fabricating dense materials as a near-net-shape forming process.[56, 57] Later, scientists realized the strength of this technique in creating materials with adjustable porous microstructures. The typical freeze casting process for fabricating porous materials involves suspension preparation, molding, solidification, and sublimation of the dispersing medium. Figure 1 illustrates this fabricating process.

The first step (suspension preparation, Fig. 2-2(a)) is similar as that of the conventional routes. Ceramic powders are dispersed in the liquid media and a key requirement for the suspensions is being stable and well-dispersed.[58] Additives such as dispersant and plasticizer can be introduced to improve the suspension homogeneity and modify the subsequent solidification process. The studied dispersing media include water, camphene, naphthalene-camphor,[59] or tertiary butanol.[60] Among these, water and camphene are the most commonly used. Different dispersing media are capable of producing specific microstructures as they behavior differently upon freezing. The initial solids loading is determined according to the desired resulting porosity and strength. The typical solids loading ranges from 5 vol% to 60 vol%.

The followed molding process (Fig. 2-2(b)) governs the external shape of the ceramics. Desirable material of the mold should not be adhered by the sample after freeze casting. Specifically, any stress generated by de-molding may compromise the ceramics or destroy the external shape. The thermal conductivity of mold influences the temperature gradient throughout the sample during freezing and subsequently affects the resulting porous microstructure.

The solidification of suspension is the critical process in determining the resulting porous microstructure. Upon temperature below the freezing point of the dispersing medium, the liquid solidified and the crystals grow to form a network. The resulting porous microstructure replicates the network of the solidified dispersing medium and the continuous crystal network leads to interconnected porous microstructure. The dispersing medium behaviors differently upon different solidification conditions, allowing freeze casting technique be able to fabricate both homogeneous and directional porous microstructures (Fig. 2-2(c)). Specifically, when the freezing conditions are controlled to achieve uniform temperature and freezing rate throughout

the sample, and the particle size is properly chosen to offset particle expulsion from the freezing front, directional growth of the solidified dispersing medium is inhibited and homogeneous (cellular) microstructures with interconnected pores can be fabricated after sublimation. When the anisotropic growth of the solidifying dispersing medium is favored by the temperature gradient or the particles expelled are arranged in a specific way, freeze casting is also able to fabricate well-defined directional (lamellar) microstructures.[61, 62] In both cases, freeze-cast microstructures can possess tailorable open pores. One issue associate with the solidification process is the volume change of the dispersing medium during freezing. For instance, water experiences 9% volume expansion while camphene displays 3% volume shrinkage after solidification.[11] The tolerance of the mold should be able to accommodate this volume change.

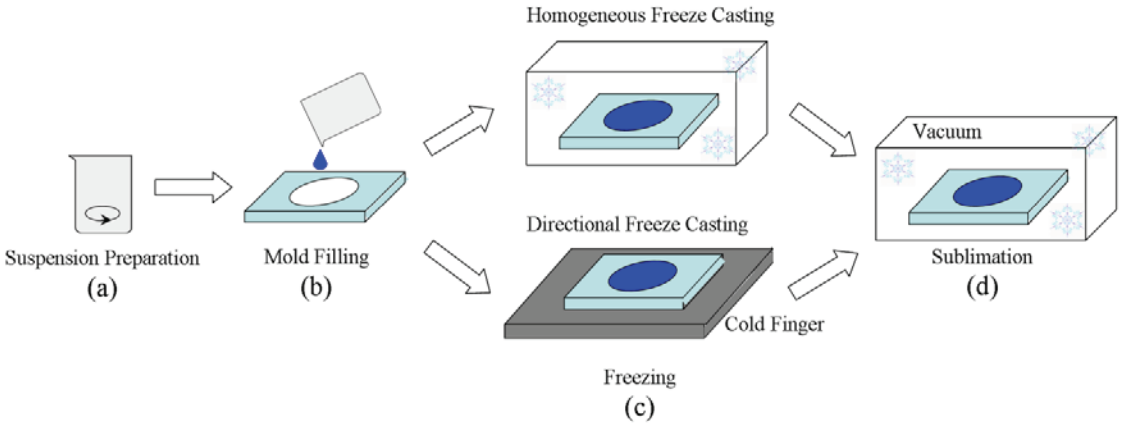

Fig. 2-2. Illustration of freeze casting process.

Once the solidification of the dispersing medium is completed, the environmental pressure is reduced while maintaining the low temperature to accomplish the sublimation. During this process, the solidified dispersing medium converts directly into gas state and the porous microstructure is obtained, replicating the former crystal structures. The applied temperature and pressure for this process vary according to the particular system, especially the dispersing medium.

Freeze cast green samples are fabricated when the dispersing medium is completely removed. The green samples are always fragile and can hardly been used in any real applications. As a result, a sintering process always follows the freeze casting route to strengthen

the freeze cast green samples. The sintering temperature is carefully controlled to reinforce the porous framework while maintaining the porosity.

Although these experimental procedures are shared by various systems, the exact parameters for each process should be separately determined for particular dispersing medium. The relationship between the aqueous suspension states and the processing steps is shown by Deville *et al.* (Fig. 2-3).[11]

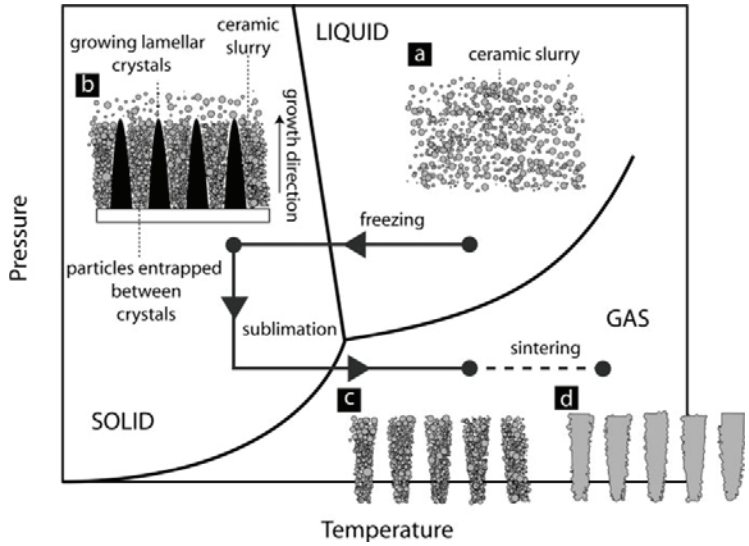

Fig. 2-3. The relationship between aqueous suspension states and the freeze casting procedures. (Reprinted from *Advanced Engineering Materials*, Vol 10/Issue 3 (2008), Deville, Freeze-Casting of Porous Ceramics: A Review of Current Achievements and Issues, Copyright (2012), with permission from John Wiley and Sons[11])

2.2.1.2 Solidification principles

Solidification of a prepared suspension is the most critical stage during freeze casting, since the crystal morphology determines the resulting porous microstructure and the volume change associated with the phase transformation greatly influences the integrity. Crystal nucleation and growth, interaction between the moving solidification front and particles, as well as the freezing modes (homogeneous or directional) are key issues that control the solidification behavior of the dispersing medium. Extensive work has been carried out to investigate ice

formation and suspension solidification and will not be discussed. However, the fundamental principles will be used to analyze the freezing process and predict the resulting microstructures.

In general, the formation of porous microstructures using freeze casting relies on the rejection of the particles by the advancing solidification front, the breakdown of the solidification front to a non-planar morphology, and the concentration and entrapment of the particles in-between the solidified crystals, all of which are determined by the interaction between the solidification front and the particles. Thermodynamically, the interfacial free energy between particles and solidification front (σ_{sp}) should be larger than the sum of interfacial free energies of solid-liquid (σ_{sl}) and particle-liquid (σ_{pl}) in order to effectively reject the particles and fabricate porous structures: [63]

$$\Delta\sigma_0 = \sigma_{sp} - (\sigma_{sl} + \sigma_{pl}) > 0 \tag{2-1}$$

In addition to the thermodynamic criterion, the rejection behavior of the particles depends on the forces they experience. For the particles close to the solidification front, the most important forces are repulsive force (F_σ) and attractive drag force (F_D), which are expressed as:[63]

$$F_\sigma = 2\pi R\Delta\sigma_o(\frac{a_o}{d})^n \tag{2-2}$$

$$F_D = \frac{6\pi\cdot\eta\cdot v\cdot R^2}{d} \tag{2-3}$$

where R refers to the particle radius, a_o refers to the average intermolecular distance, d is the particle and ice front distance, n is a constant from 1 to 4, v is the ice growth velocity, η is the suspension viscosity. With these equations, the engulfment or repulsion of the particles can be predicted. Specifically, the thermodynamic criterion (eq. (2-1)) should be satisfied to allow possible particle repulsion, where a liquid film exists between the solidification front and the rejected particles to ensure the transfer of liquid molecules for the continuously growing crystals. In addition, the repulsion of particles occurs only if the net force on the particles at the crystal-particle interface is repulsive. The balance between repulsive force (eq. (2-2)) and attractive drag force (eq. (2-3)) provides out the other critical criterion.

The break-down of the solidification front is necessary for the formation of porous structures and often happens because of the instability and supercooling at the interface of the advancing solidification front, the possibility of secondary nucleation, and the inhomogeneity of the freezing zone.[64-66] The curvature at the interface is dependent on the relative thermal

conductivities: if the particles possess a higher thermal conductivity, the interface is concave; conversely the interface is convex.[67] These interface deviations from a planar surface can further affect the freezing point of the local suspension and alter the supercooling and solidification behavior.[68] Based on the dispersing media used (e.g. water, camphene) and the typical freezing conditions, the freezing process is similar to unidirectional solidification, which has been extensively studied by Trivedi, Peppin, Worster, and their co-workers.[64, 65, 69-75]

A different aspect of freeze casting is particle velocities, which are affected by the forces exerting on particles. Several models have been established to describe particle velocity, which is mostly affected by the particle radius and relative density between the particles and the dispersing medium, but less sensitive to the temperature gradient[61, 68, 76] The critical solidification front velocity for particle trapping can be estimated by the following equation:[61, 67]

$$v_c = \frac{\rho_1}{9\eta\rho_s}\left[-\frac{A}{2\pi D d_0} - gDd_0\left(\rho_p - \rho_1\right)\right] \tag{2-4}$$

where D is the particle diameter, A is the Hamaker constant of the aqueous system, η is the viscosity of the liquid phase, d_0 is the minimal distance between the particle and the freezing front, ρ_p is the particle density, ρ_s and ρ_l are the densities of the solid and liquid phases, and g is the gravitational constant. The particle entrapment occurs when the solidification velocity is higher than this critical value. It should be mentioned that scientists have developed different equations that describe the critical solidification front velocity which are obtained by setting the sum of the forces (i.e. repulsive force and attractive drag force) to be zero. The main difference between these equations is the choice of the forces, and eq. (2-4) is derived considering gravity, viscous drag forces, buoyancy forces, and molecular van der Waals forces.

It also needs to be noticed that most of the above studies on suspension solidification are carried out for aqueous systems. However, the fundamental principles are applicable to all the systems and the porous morphology of the freeze cast materials can be qualitatively predicted.

2.2.2 Porous structure development

2.2.2.1 Solidification of dispersing medium

The behavior of dispersing medium during solidification process is the most significant factor that determines the resulting porous structure, which is a replication of the crystal network.

Water and camphene are two most popular dispersing media used for freeze casting. Since this proposed work bases on aqueous systems, this section mainly focuses on the solidification behavior of water, while basic properties of camphene are briefly mentioned.

The solidification behavior of water can be understood from the ice nucleation and crystal growth in aqueous systems.[77-83] Ice has 15 known crystalline phases, among which hexagonal ice is the most common structure (Fig. 2-4(b)). According to the crystal structure (Fig. 2-4(a)) and crystal growth kinetics of ice,[11] the ice growth rate along the *a* axis is 10^2 to 10^3 times faster than that along the *c* axis (Fig. 2-4(b)). Thus, the growth of ice crystals with the temperature gradient perpendicular to the *c* axis is kinetically favorable. This ice crystal morphology results in spontaneously preferred lamellar structure for the freeze-cast or sintered samples (Fig. 2-4(c)).

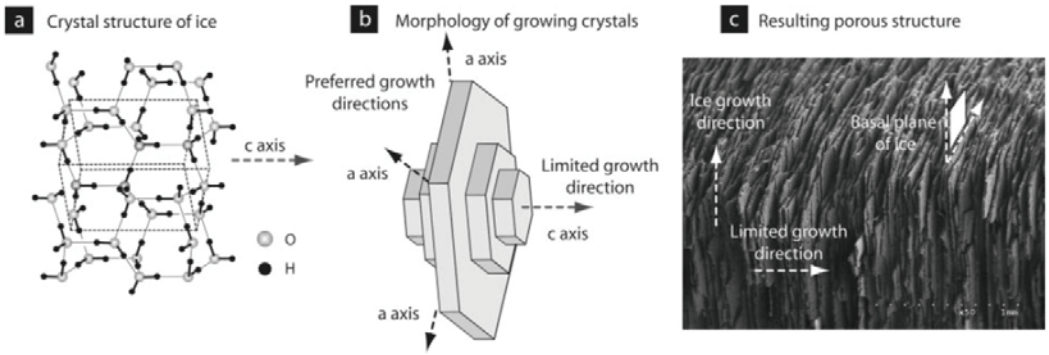

Fig. 2-4. Directional microstructure formation mechanism for aqueous suspensions: (a) crystal structure of ice, (b) anisotropy of ice crystal growth, (c) lamellar structure of resulting materials. (Reprinted from *Advanced Engineering Materials*, Vol 10/Issue 3 (2008), Deville, Freeze-Casting of Porous Ceramics: A Review of Current Achievements and Issues, Copyright (2012), with permission from John Wiley and Sons[11])

To form porous structures, particles must be rejected from the solidification front and trapped in-between the crystal arms. The break-down of the solidification front can be generated by different mechanisms. One mechanism known as Mullins-Sekerka instability indicates the solidification interface evolves from flat to cellular, and then to lamellar caused by the inherent thermodynamic instability of the interface.[66] Another mechanism reported by Deville *et al.* believes both lamellar crystals oriented along the freezing direction (Fig. 2-5(a)) and pseudo-

lamellar ones along the radial direction (Fig. 2-5(b)) form at the initial stage.[83-85] The interface instability is due to the presence of the particles. Under the freeze casting triggered by the cold finger (Fig. 2-2(c)), the initial ice crystals are randomly oriented and the growth velocity (the distance that solidification front travels per unit time in the vertical direction) is high enough to engulf all the particles for a dense microstructure to form. Then, ice crystals both along the freezing direction and randomly oriented ones grow with the diminishing ice front velocity. With the ice crystals grow, an obvious crystal morphology transition occurs because of the significant temperature gradient caused by increased thermal conductivity and enhanced residual stress. Ice crystals keep growing along the freezing direction.[84] Passing the initial instant of rapid ice crystal growth, the solidification transitions into a steady state. The advancing solidification front repels particles and dendritic growth of ice crystals occurs. The morphologies of the growing ice crystals and the resulting pores are determined by the thermal gradient and particle redistribution, instead of particle diffusion.[85] Solidification front velocity, particle size, ice crystal morphology, and the angle between crystal growth direction and temperature gradient are key factors that determine the particle redistribution.[85]

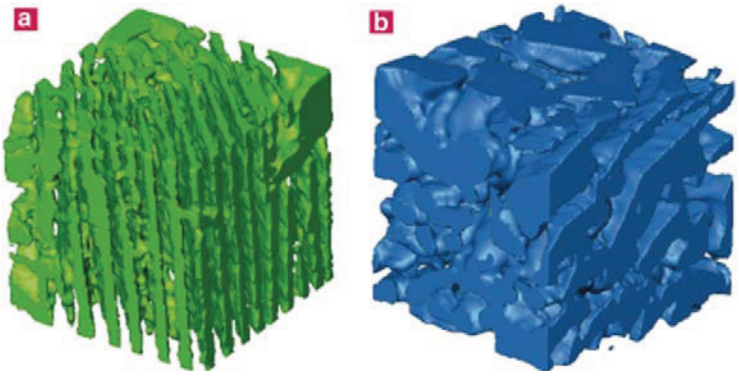

Fig. 2-5. Three-dimensional ice crystal structure at the initial solidification stage reconstructed from tomography data: (a) the lamellar crystals oriented along the freezing direction, (b) pseudo-lamellar ones along the radial direction. (Reprinted from *Journal of the American Ceramic Society*, Vol 92/Issue 11 (2009), Deville *et al.*, In Situ X-Ray Radiography and Tomography Observations of the Solidification of Aqueous Alumina Particle Suspensions—Part I: Initial Instants, Copyright (2012), with permission from John Wiley and Sons[84])

As for camphene-based systems, the typical morphology of the solidified phase is dendrites. An approximation of camphene dendrite growth velocity is reported as:[86]

$$\upsilon = 0.018 \frac{\kappa \Delta S \Delta H}{\Omega \gamma C_p} \Delta \theta^{2.5} \quad (2\text{-}5)$$

where κ is the thermal diffusivity, ΔS is the molar entropy of fusion, ΔH is the molar enthalpy of fusion, Ω is the molar volume, γ is the solid-liquid interfacial energy, C_p is the molar heat capacity of the liquid, $\Delta\theta$ is the dimensionless undercooling ($=\Delta T/(\Delta H/C_p)$).[86] Camphene also kinetically favors the formation of directional microstructures.

2.2.2.2 Homogeneous and directional freeze casting

Although the dispersing media (water and camphene) favor directional growth of the crystals, the resulting porous microstructure can be effectively controlled by the manners of freeze casting. Freeze casting techniques can be generally categorized into homogeneous and directional freeze casting. When the freezing condition is carefully controlled that the temperature gradient is minimized, the nucleation occurs at any locations without any preference and the directional crystal growth is inhibited. In this case, homogeneous microstructures can be fabricated. In addition, high particle expulsion hindrance is also able to hinder the oriented growth of solidified crystals and promotes the structural homogeneity. In contrast, the formation of lamellar pores possessing larger dimensions along the preferred growth directions of crystals can be prepared by increasing the temperature gradient while lowering the particle hindrance, namely directional freeze casting. The lamellar wavelength can be empirically estimated based on the temperature grident (υ), $\lambda \sim \upsilon^{-n}$, where n is a constant depends on specific system.[87] Temperature gradient is dependent on sample volume, shape, thermal conductivity, and freezing rate. Particle expulsion hindrance is influenced by particle size, particle shape, and the viscosity of the suspension.

For directional freeze casting, bridge formation between lamellar pores is another interesting phenomenon. These bridges are caused by overgrown dendrites or densely packed particles in local regions, due to particle repulsion from the solidification front, dendritic tip splitting or healing, and particle agglomeration.[11] The bridge structure can be modified by additives that affect interfacial tension and interparticle forces.[88]

2.2.3 Critical factors

The interaction between the solidification front and the particles determines the solidification behavior of the dispersing media and subsequently determines the porous microstructure. This section focuses on the key factors for both homogeneous and directional freezing processes. Freezing conditions (e.g. freezing temperature, freezing time, freezing rate) suspension solids loading, and particle size are discussed. Additives and their effects on the microstructure evolution are evaluated. The fundamental mechanisms of these factors in influencing the resulting microstructures are also analyzed. Again, aqueous systems are mainly discussed here as the proposed project involves a water-based suspension. Fundamental principles are shared by various systems (ceramics, metals, polymers, and composites) and can be applied to other dispersing media.

2.2.3.1 Freezing condition

Freezing temperature, freezing rate, freezing time, temperature gradient, and solidification front velocity are significant factors affecting ice nucleation and crystal growth and subsequently the morphology of porous microstructures. Although different systems are affected differently by these factors, the overall trend in the microstructure evolution is shared by most materials.

Freezing temperature affects the relative dominance of ice nucleation and crystal growth. For ice nucleation to occur, suspension supercooling is needed. Under high supercooling, namely low temperature, nucleation rate is higher than crystal growth rate, so ice nucleation is more favorable than ice crystal growth. At such freezing temperatures, a large number of small ice crystals form and the porous microstructure consists of uniform small pores. In contrast, if the supercooling is low, ice growth is favorable. A small number of large ice crystals result during freeze casting, and larger pores form after the ice sublimation. On the other hand, a higher freezing temperature induces lower ice crystal growth rate and expulsion efficiency, which means smaller pore sizes. During freeze casting, these two factors compete with each other to determine the final pore sizes.

In addition, the shape of the ice crystals formed during freeze casting also depends on the freezing temperature, which influences the supercooling behaviors. The interface curvature and supercooling are correlated with each other and the morphology of the solidification front varies

with the freezing temperature. This effect in combination with secondary nucleation influences the final shape of the ice crystals and porous microstructures. Overall, different freezing temperatures lead to different ice solidification behaviors, and ultimately different pore sizes and morphologies. Since the particles cannot rearrange sufficiently under high supercooling conditions, lower freezing temperature produces higher porosity in materials.[89] At relatively high freezing temperatures, the degree of supercooling is low and it always takes a longer time for the entire sample to be solidified. As time goes, the growth of ice crystals in one specific direction may be disturbed as a result of the changing supercooling condition at the interface and the possible growth of secondary dendrites. Thus, lamellar pores evolve into dendritic pores. When the freezing temperature further increases to around the freezing point, directional freezing effect is even less important and tortuous ice growth may appear.[90] The decreases in ice crystal growth rate and solid particle rejection also influence the resulting pore sizes. The typical freezing temperature range for aqueous systems is from -18ºC to -196ºC.

Freezing rate is another factor that influences the morphology of porous microstructures.[91, 92] The typical freezing rate for aqueous systems is from 0.05ºC/min up to cooling by immersing a sample in liquid propane (sudden change from room temperature to -196ºC). At a high freezing rate, ice nucleation is kinetically more favorable than crystal growth, small pore formation is more likely. Moreover, the dispersing state of the suspension is more likely to be maintained at a high freezing rate since there is less time for particles to rearrange. Similarly, a higher freezing rate for directional freeze casting have finer lamellar structures and pores, while those obtained at a lower freezing rate have larger lamellar structures and pore sizes.[93] Fig. 2-6 is an example of freezing rate effect on the microstructure. Both samples are made by freeze casting of a kaolinite-silica suspension. Compared with the sample frozen at a low rate (< 2^{o}C/min) (Fig. 2-6(a)), the sample produced by direct immersion into liquid propane (-196ºC) possesses smaller pores with a narrow pore size distribution (Fig. 2-6(b)).[91] Lower freezing rate provides nanoparticles with more time to rearrange, and thus the particle packing is denser.[57, 92] As for alumina nanoparticle suspensions frozen at 1ºC/min and 0.05ºC /min freezing rates have visibly different microstructures on the as-cast surfaces. Lower freezing rate offers more densely packed nanoparticles and lower porosity. In addition, freezing rate has strong dependence on the heat transfer within the sample.[94, 95] When the temperature gradient is large, heat transfer efficiency is high and ice crystals can continuously grow and lead to interconnected

or dendritic porous structures. When heat transfer efficiency is low, the diffusion of water molecules and the growth of ice crystals are hindered, thus oval pore structure is more likely.

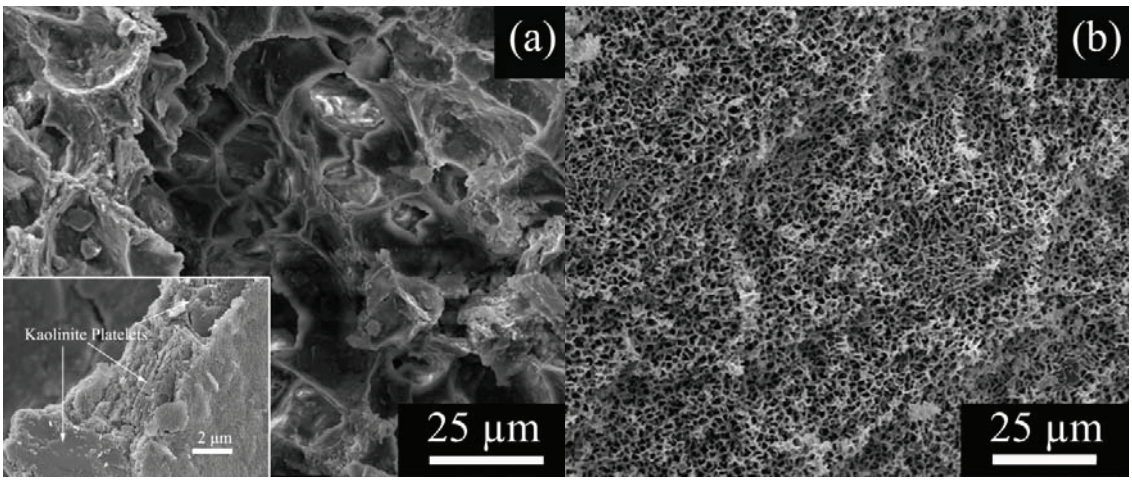

Fig. 2-6. Freezing rate effect on microstructures of a kaolinite-silica system: (a) freezing rate < 2 ºC /min, (b) directly immersed into liquid propane (-196 ºC). The insert in (a) is a high magnification images showing the pore wall structure. (Reprinted from *Journal of the American Ceramic Society*, Vol 92/Issue 4 (2009), McKee *et al.*, Effects of Added Clay on the Properties of Freeze-Casted Composites of Silica Nanoparticles, Copyright (2012), with permission from John Wiley and Sons[91])

Freezing time also affects ice crystal growth. When a sample is maintained at a certain freezing temperature, ice crystals keep growing and small crystals can link to each other and form large crystals. As mentioned above, anisotropic growth of ice crystals is favored based on the chemical potentials of different ice crystal facets. Elongated ice crystals form if the freezing process is uninterrupted. In addition, the rejected particles form the walls and the growing ice crystals result in dendritic structures due to the hindrance effect from the solid particles. Therefore, long freezing time favors columnar and lamellar microstructures. Based on this understanding, it is possible to control the porous structure by adjusting the freezing time.

Temperature gradient influences the solidification direction and subsequently the lamellar structure direction.[87] If we define the crystal growth rate along the temperature gradient direction as r, and the rate along the preferred crystal growth direction (determined by the interfacial energy) as r_p, the ratio of r_p/r strongly relies on the temperature gradient $(T_1\text{-}T_2)/L$, where $T_1(t)$

and $T_2(t)$ are time-dependent mold top and bottom temperatures and L is the length of the mold. When the temperature gradient changes, the ice crystal growth direction tilts with the variation of r_p/r.

Solidification velocity is another factor (in addition to particle size, pH value, and viscosity) that affects resulting porous structure, especially for the lamellar spacing during directional freeze casting.[96] When the solidification velocity is extremely low, lamellar structures may disappear. This is because the ice front velocity is much lower than the critical particle entrapment velocity and the low solidification velocity makes the ice front more stable. Thus, the solidification front does not break down and a planar morphology remains, in which case all the particles are rejected together and directional microstructure cannot be generated. As shown in Fig. 2-7, a switch-over occurs at 0.4 μm/s velocity for a 22 vol% alumina aqueous suspension, below which a planar ice front appears instead of a lamellar structure. When the velocity is higher than 2 $\mu m \cdot s^{-1}$, a lamellar ice front forms and the space between lamellae decreases with the velocity increase. On the other hand, the ice front velocity should be lower than the so-called critical velocity in order to produce porous microstructures. If the velocity is higher than this value, particles cannot be transported along the growing ice front and the engulfment of particles occurs.[11]

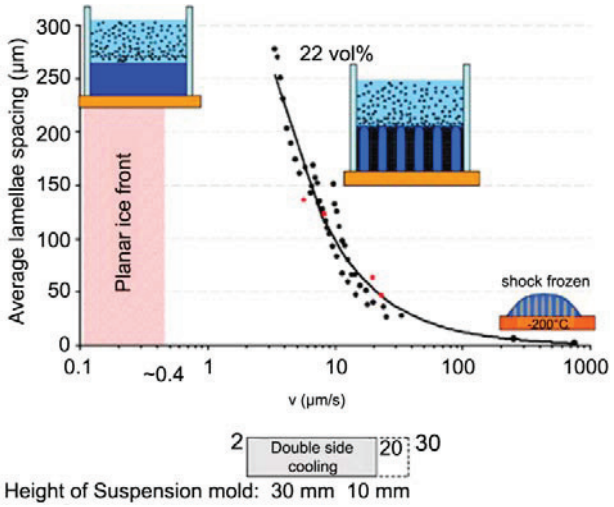

Fig. 2-7. Overview of the lamellar spacing development over a wide range of solidification velocities. (Reprinted from *Journal of the American Ceramic Society*, Vol 92/Issue Supplement s1 (2008), Waschkies *et al.*, Control of Lamellae Spacing During Freeze Casting of Ceramics

Using Double-Side Cooling as a Novel Processing Route, Copyright (2012), with permission from John Wiley and Sons[96])

In combination, numerous small pores can be obtained by low freezing temperature and high freezing rate. The homogeneity of the microstructure is promoted with short freezing time and low heat transfer efficiency. These factors have more influence on porous morphology than on pore dimensions for directional freeze casting. Although only a few specific systems are presented here to analyze these freezing condition effects on microstructures, the fundamental physical principles are applicable to most materials. Since the effects of freezing conditions are relatively independent of the specific freeze casting systems, it is possible to predict porous microstructure evolution when other factors are properly controlled.

2.2.3.2 Suspension solids loading

Suspension solids loading directly influences the microstructure and properties of freeze-cast samples and ranges widely from 5 to 60 vol%. Higher solids loading suspensions possess lower water content and thus produce lower porosity and higher density freeze-cast samples. In addition, less expansion of ice due to the lower water content further enhances the density of the resulting samples. Porosity decrease caused by increased suspension solids loading leads to stronger solid samples. The finer microstructure from the high suspension solids loading further enhances the sample strength. A review of the relationship between porosity and solids loading of sintered freeze cast samples is provided by Deville *et al.*[11] Furthermore, the suspension solids loading can also influence the homogeneity of the resulting microstructure. In addition, suspension solids loading also influences pore morphology.[97, 98] For gradient titanium dioxide porous sheets (Fig. 2-8),[99] the pores evolve from dendritic into three-dimensional reticular shapes with an increase in the suspension solids loading. When the solids loading is low, such as 2.6 vol% (Fig. 2-8(a)), the particles are effectively repelled by the ice solidification front, the ice crystals are elongated along the thermal gradient direction and grow into large sizes with highly interconnected microstructures. At a higher solids loading, such as 13.6 vol% (Fig. 2-8(b)), particles are ejected less effectively, the solidification front movement is not powerful enough compared to the growth of the pore walls, the accumulated particles form the pore walls and hinder the growth of ice crystals. As a result, the ice crystal size decreases and the pore shape

evolves from dendritic into interconnected reticular. For different systems, the solids loading effects on the microstructure homogeneity need to be evaluated individually. However, the fundamental mechanisms of the microstructure evolution are still based on particle expulsion and hindrance effect.

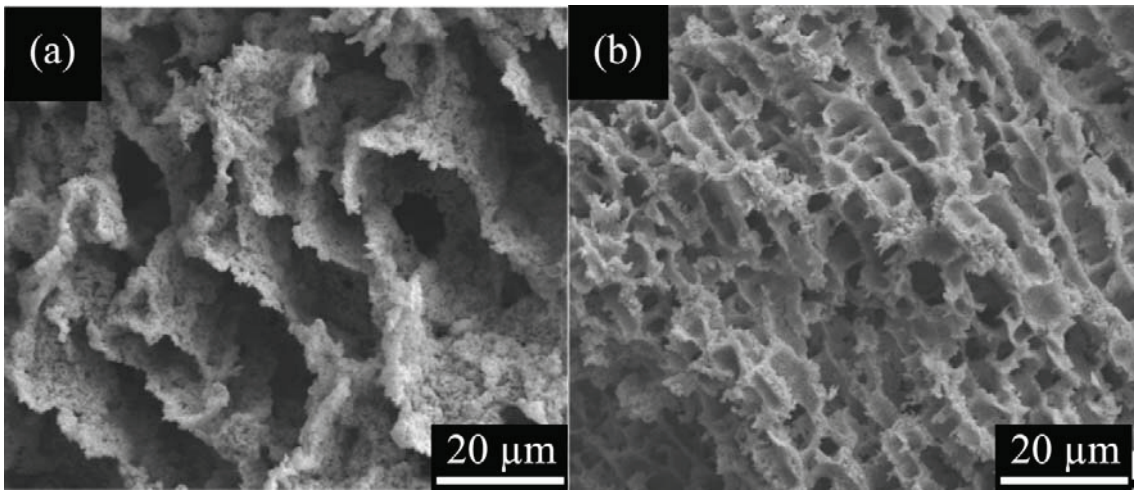

Fig. 2-8. Effects of suspension solids loading on the morphology of porous titanium dioxide microstructures. Solids loading: (a) 2.6 vol%, (b) 13.6 vol%. (Reprinted from *Journal of the American Ceramic Society*, Vol 90/Issue 9 (2007), Ren *et al.*, Fabrication of Gradient Pore TiO_2 Sheets by a Novel Freeze–Tape-Casting Process, Copyright (2012), with permission from John Wiley and Sons[99])

2.2.3.3 Particle size

Particle size influences the freeze-cast microstructure. Since ice nucleation mostly experiences a heterogeneous process, smaller particle size provides more nucleation sites (i.e. liquid-solid interface, specifically the particle surfaces) and results in the formation of numerous small pores. When the particle size is comparable to that of the crystals from the frozen liquid, the mobility of the particles is reduced and the engulfment of the particles is more likely. As a result, the structural homogeneity is compromised. Large particle systems are unlikely to replicate the fine structure of small ice crystals and the detailed features in microstructure are lost. However, for systems containing different kinds of particles, large ones may obstruct the propagation of growing ice and limit pore sizes.[91] Large particles also provide higher

supercooling compared to small particles since fewer nucleation sites allow the suspension to reach a lower nucleation temperature. Thus, larger structural gradient occurs in a system with larger particles as a result of the corresponding faster moving solidification front.[100] When the large particles are big enough and their content is high, pore sizes and porosity increase. For the kaolinite-silica system discussed previously, the micron-sized kaolinite particles disturb the original silica network and build a new framework for the composite, leading to an increase in pore sizes. On the other hand, there exists an upper limit in particle size for the formation of homogeneous microstructures, above which particle sedimentation and suspension instability need to be addressed. This critical particle size differs for each specific suspension system and is influenced by electric double layer, van der Waals force, and Brownian motion, which depend on particle/liquid densities, suspension viscosity, temperature, particle shape, and surface charges. Small particles are always beneficial for improving the homogeneity, integrity, and fine structures of the resulting materials.

Particle size also affects pore morphology. Large particles will be trapped within the solidification front instead of being rejected. A plot of equation (2-4) is shown in Fig. 2-8 for a titanium suspension. Since the titanium particles can be oxidized by air or water during freeze casting, the aqueous system is deaerated, 0.2 wt% agar and a very small amount of neutral detergent are added in the study.[61] As shown in Fig. 2-9, the critical ice front velocity decreases with titanium particle size. Since the critical ice front velocity describes the condition when the ice front and particles share the same velocity, the region above the curve gives the conditions when the particles are engulfed during the freeze casting. The region below the curve indicates the conditions when the particles are repelled by the ice front. Specifically, small particles will be rejected by the solidification front and elongated ice crystals will form during directional freeze casting; large particles will be engulfed by the ice solidification front and lead to oval pore shapes at a certain ice front velocity. For example, for 2~12 $\mu m \cdot s^{-1}$ ice front velocity v, particles < 45 μm will be rejected. When the particle size is 125 μm, it is on the boundary of being engulfed/ejected. Any particles > 125 μm will be engulfed.

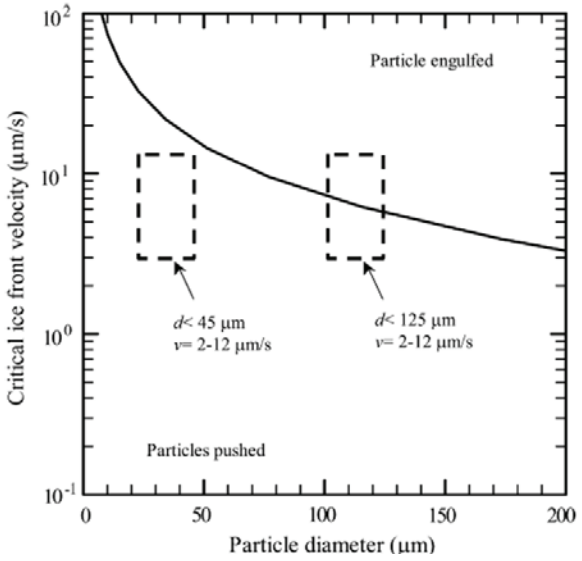

Fig. 2-9. Titanium particle size effects on critical ice front velocity. (Reprinted from *Acta Materialia*, Vol 56/Issue 1 (2008), Chino *et al.*, Directionally freeze-cast titanium foam with aligned, elongated Pores, Copyright (2012), with permission from Elsevier[61])

2.2.3.4 Additives

Additives are used to modify the freeze casting parameters since they are able to change the solvent phase diagram, the anisotropy of the solid/liquid interfacial energy, the interparticle forces, the degree of undercooling, the solvent viscosity, the suspension freezing point, and the volume expansion of the system. Furthermore, some additives are able to induce a gelation or bond to solvent molecules.[88] Some of these effects are interrelated and work synergistically to modify the microstructures. For aqueous systems, commonly used additives include glycerol, poly(acrylic acid) (PAA), gelatin, dioxane, polyvinyl alcohol (PVA), and polyethylene glycol (PEG).

Glycerol is one of the most commonly used additives. It is non-toxic, highly soluble in water, inexpensive, and has low freezing point and vapor pressure.[57, 101-105] When added to a suspension, glycerol binds to water molecules and blocks the growth of ice crystals, resulting in the formation of a localized amorphous ice structure and a reduction in ice crystal size. Glycerol is also effective in reducing the volumetric expansion of water, inhibiting particle rejection, and modifying the suspension viscosity. In general, the high viscosity of glycerol (934 mPa·s) always inhibits the fluidity of the suspension, which limits water molecule diffusion and leads to

formation of small ice crystals. However, the effect of glycerol on suspension viscosity greatly depends on additives in suspension and solids loading. For an alumina suspension with ammonium polymethacrylate additive at a high solids loading (such as 60 vol%), the viscosity decreases from 2613 mPa·s to 1599 mPa·s at a shear rate of 12 s^{-1} with 20 wt% glycerol addition.[57] This is because the glycerol addition enhances the steric hindrance among the dispersant and acts as a lubricant between particles. Thus, a better dispersed and more flowable suspension is obtained, ice crystal uniformity can be improved, and homogeneous microstructures can be obtained.[101] At low solids loading where the particle separation exceeds the steric barrier distance, this enhance effect in steric hindrance becomes invisible and the high glycerol viscosity and its interaction with water molecules play a dominant role. In addition, glycerol is widely used to lower the freezing point of particle suspensions and adjust the corresponding microstructures.[106, 107] For an alumina particle system, the density of green samples increases slightly since the glycerol molecules decrease the growth of ice crystals and subsequently reduce the expansion of ice. These characteristics in combination make glycerol effective in modifying porous microstructures and reducing defects and large cleavage fracture. The effect of glycerol on the integrity of alumina nanoparticle samples is reported by Lu *et al*.[106] Cracks and defects are apparent in the sample without glycerol because of the formation and expansion of ice crystals. In contrast, the sample with 10 wt% glycerol possesses a smooth fracture surface and uniform microstructures.

Compared to the freeze casting of homogeneous microstructures, glycerol has more effect on microstructures for directional freeze casting since it affects both the size and shape of pores. In a suspension, water molecules concentrate around the polar groups of glycerol. The viscosity of the liquid increases with glycerol concentration, which limits water molecule diffusion during ice crystallization. The disturbed ice lattice and the reduced diffusion length result in smaller ice crystals and less repulsion of solid particles, which leads to refined porous microstructures and small pore sizes. As shown in Fig. 2-10, HA lamellas are fabricated with larger pore channels and fewer bridges without glycerol (Fig. 2-10(a)). With glycerol, lamellar structures evolve into small dendritic pores and the number of dendritic bridges between pores increases dramatically (Fig. 2-10(b)).[101, 104, 105] With the increase of glycerol concentration in the suspension, the porosity also decreases due to the reduced ice expansion during the freeze casting process.

Accompanying the finer porous microstructure, the strength of the sample is improved with the addition of glycerol.[102]

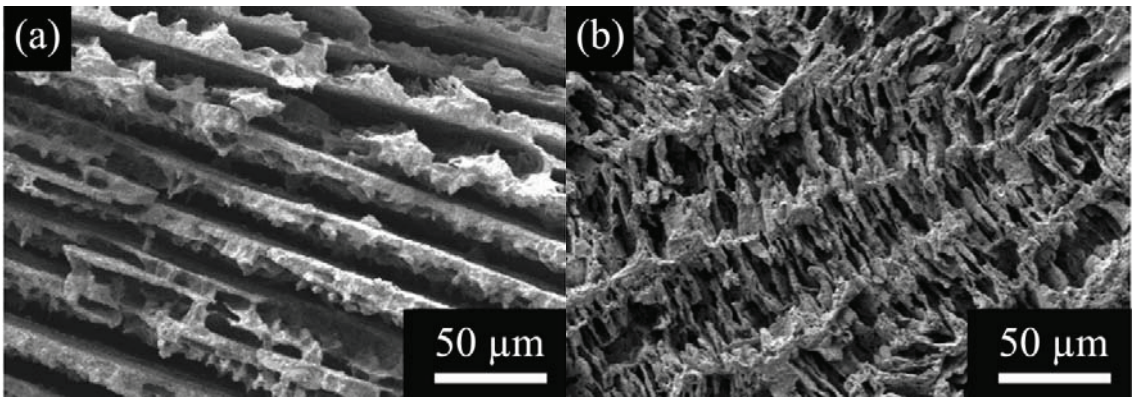

Fig. 2-10. Glycerol effect on pore morphology of HA system from 10 vol% suspension: (a) water, (b) water + 20 wt% glycerol. (Reprinted from *Biomedical Materials*, Vol 3/Issue 2 (2008), Fu *et al.*, Freeze-cast hydroxyapatite scaffolds for bone tissue engineering applications, Copyright (2012), with permission from IOP Publishing Ltd.[105])

In addition, glycerol can work with other additives to adjust the microstructures. Examples are alumina nanoparticle suspensions with glycerol and PAA, or with glycerol and ammonium polymethacrylate.[57, 106, 108] The polymers act as anionic dispersants. The negatively charged dispersant chains adsorbed to the positively charged alumina nanoparticles screen the nanoparticles from being directly exposed to glycerol, and interact with glycerol through hydrogen bonds to prevent the chains from entangling with each other. Micelle structures may also form. Subsequently, the electrostatic repulsion and steric stabilization result in the increase of particle dispersion. The homogeneity of the suspension is improved even though the sample density decreases slightly.[57, 106] With added glycerol and dispersant, the microstructure is more mesh-like (Fig. 2-11).[57]

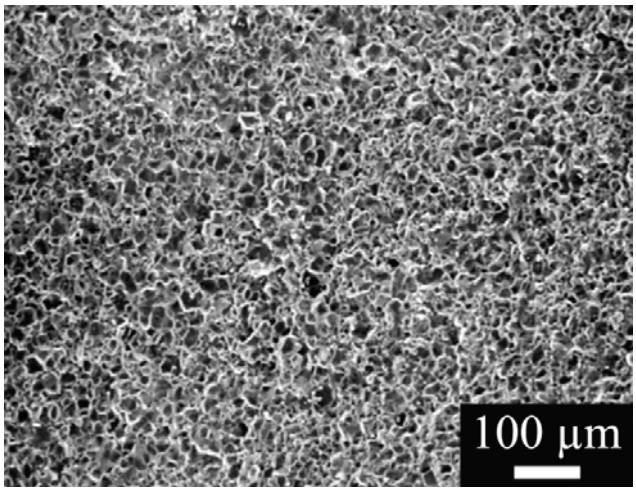

Fig. 2-11. Effect of glycerol in building a mesh-like microstructure in an alumina system. (Reprinted from *Journal of the American Ceramic Society*, Vol 84/Issue 7 (2004), Sofie *et al.*, Freeze Casting of Aqueous Alumina Slurries with Glycerol, Copyright (2012), with permission from John Wiley and Sons[57])

Although glycerol improves microstructure homogeneity, its amount needs to be properly chosen. This is because glycerol has a low vapor pressure. After freeze casting, glycerol stays throughout the sample and often needs to be removed. In addition, excessive glycerol increases suspension viscosity or prevents a sample from drying even after ice is sublimated. A wet sample, because of the excessive presence of glycerol, can lead to shape deformation.[57]

Gelatin is another additive used in freeze casting. It is a hydrolyzed form of collagen, which comes from animal's skin and bones. Gelatin addition to a freeze casting system of hydroxyapatite (HA, $(Ca_{10}(PO_4)_6(OH)_2)$ is effective in adjusting the solid state microstructure and porosity. During freeze casting, gelatin slowly gelatinizes and gelatin-containing HA particles hinder the anisotropic growth of ice crystals. Fig. 2-9 shows such a system as an example. Without gelatin addition, the ice crystal growth fronts reject HA particles to form walls and lamellar porous microstructures (Figs. 2-12(a)). With the addition of gelatin, the pores evolve into spherical and reticulated shapes (Figs. 2-12(b)). The HA particles in combination with gelatin form a network, effectively hinder the growth of ice crystals, and result in the pore evolution from lamellar structures to three dimensional reticulated shapes. [109]

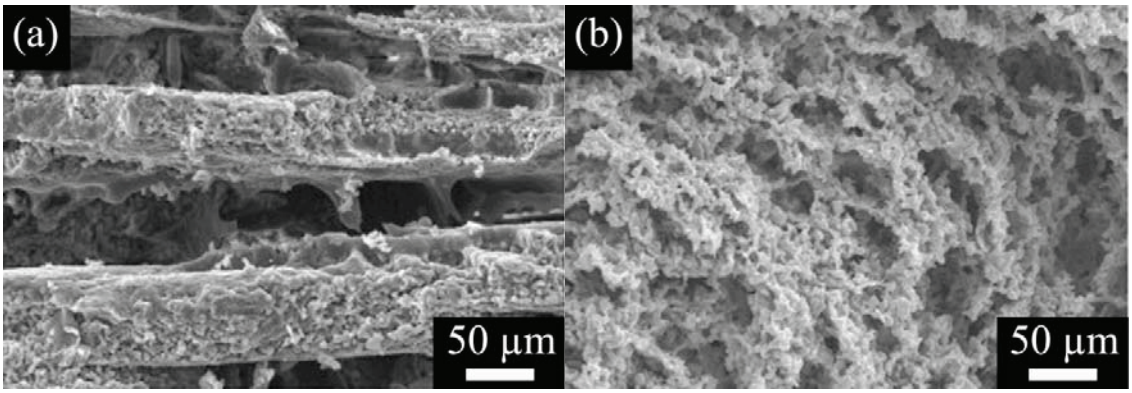

Fig. 2-12. Effects of gelatin on microstructures of a HA system: (a) no gelatin, (b) 6 wt% gelatin. (Reprinted from *Ceramics International*, Vol 35/Issue 6 (2009), Zhang *et al.*, Effects of gelatin addition on the microstructure of freeze-cast porous hydroxyapatite ceramics, Copyright (2012), with permission from Elsevier[109])

Dioxane is a common additive for water-based directional freeze casting systems.[101, 104, 105] Dioxane can induce remarkable microstructure evolution from lamellar to cellular pores. The fundamental process can be understood as follows. When dispersed in water, dioxane breaks the hydrogen bonds of water and forms stable dioxane-water complexes $(dioxane)_m$-$(H_2O)_n$, which favors a columnar structure when solidified. When the dioxane concentration is below ~13 mol%, water molecules connected by hydrogen bonds are dominant in the liquid, therefore the pore shape remains lamellar, similar to the morphology of pure aqueous systems. The added dioxane only affects the pore sizes. However, as the concentration of dioxane increases to above ~23 mol%, the suspension is dominated by $(dioxane)_m$-$(H_2O)_n$ complexes instead of hydrogen bonds, which reduces solid particle expulsion and blocks directional ice crystal growth, and the microstructure evolves into a cellular type.[104, 105] The dioxane effect on pore morphology evolution of a HA system is as follows. When the suspension is made without dioxane, a lamellar pore structure is obtained as HA particles are effectively expelled from the ice front. With 23 mol% dioxane addition, a hypereutectic suspension mixture is made, the freezing point increases from -10°C to -5°C, and cellular dioxane crystals form. Therefore, the microstructure evolves from lamellar to cellular. If the dioxane concentration increases further, the suspension will have a large amount of dioxane crystals and the solid sample will have a large amount of fine pores.[104]

PVA is another additive that is used to adjust the pore morphology in directional freeze casting.[52, 105, 109] Without PVA, solid particles are more likely to be repelled from the ice crystal fronts and the accumulated particles are more likely to block the growth of ice crystals. This leads to the formation of lamellar porous microstructures. With the addition of PVA, the solution can experience a gelation process at a relatively high temperature and the viscosity of the suspension increases accordingly. During freezing, the gelled PVA combines with solid particles and inhibits the growth of ice crystals, resulting in a decrease of ice crystal sizes and providing refined pore sizes and morphology.[52, 110] Large and isolated lamellar pores transform into small and interconnected lamellar or columnar pores; porosity increases.[52, 111] An example of PVA effects on the freeze cast microstructures is displayed in an yttria-stabilized-zirconia (YSZ) system.[52] The samples are frozen at -18°C. For the samples without PVA, lamellar ice crystals form as the particles are repelled from the ice front, and porous lamellar microstructure is fabricated. With the addition of PVA, ice crystal growth is hindered by the gelled PVA and the pore morphology evolves into interconnected small pores.[52] The microstructures of titanium dioxide can also be adjusted by controlling the concentration of PVA.[111] Without PVA, a dendritic porous structure forms from the sample top to the bottom due to a temperature gradient. With increased PVA concentration, the porous morphology evolves from dendritic to columnar. Because of the polymeric long chain configuration, PVA cannot move freely in the suspension and the suspension loses fluidity as the temperature decreases. The suspension gels with temperature decrease and evolves into two phases: ice crystals and PVA-wrapped titanium dioxide particles. The gelation and phase separation limit the diffusion of water molecules and lead to small ice crystals and eventually small pores.

Polyethylene glycol (PEG) acts as a binder and affects the microstructure of freeze cast alumina.[112] In the alumina suspension, concentrated PEG in the solidification front decreases the local equilibrium solidification temperature. As a result, the supercooling of the suspension at the ice front decreases, allowing the solidified tips to melt back into the suspension. This process further breaks down the solidification front and leads to a finer microstructure. In addition, lower supercooling allows ripening of secondary dendrites, where thin secondary tips melt back while thicker dendrites grow even larger; the spaces between secondary dendrites increase. PEG addition also influences the lamellar size of the freeze cast alumina, either by poisoning the preferred growth direction or affecting the diffusivity of water molecules.[112]

Overall, additives introduced into the homogeneous freeze casting systems affect the pore morphology by adjusting the ice solidification behavior. Most additives are used with the purpose of improving the homogeneity and integrity of the resulting porous materials. Although limited additives are discussed, their functions represent the main mechanisms of modifying the freeze casting microstructures. Other additives that are capable of adjusting suspension viscosity, freezing point, particle dispersion, or particle hindrance on the ice crystal growth can be introduced to control the homogeneity and integrity of the porous microstructures. For directional freeze casting, additives affect the pore morphology of aqueous systems by either limiting the diffusion of water molecules or producing fine crystals. Glycerol and dioxane combine with water molecules and modify the freezing point of the suspension and ice expansion. PVA can experience a gelation process during freeze casting and influence the particle hindrance and water molecule diffusion. PEG affects the suspension supercooling and ice solidification behaviors. Most additives refine the microstructures and other chemicals with similar behaviors can also be considered for directional freeze casting.

The critical issues and their effects on porous structure evolution for aqueous systems are presented in Table 2-1.

2.2.3.5 External conditions

Besides the inherent conditions discussed above, the external conditions are equally effective in modifying the solidification behavior of the dispersing media and controlling the resulting porous microstructures. This section reviews three techniques: double-sided freeze casting, freeze tape casting, and field-directed freeze casting. These novel techniques evolve from traditional freeze casting with modified external conditions. Most of these modifications are designed for directional freeze casting and the temperature gradient and solidification behaviors are carefully controlled.

Double-sided freezing is a freeze casting technique that freezes the suspension from both sides of the sample in order to keep the solidification velocity constant during the entire freezing process with the aim of obtaining constant-spaced lamellae.[96, 98] For one-sided freezing, the

Table 2-1. Summary of critical factors affecting porous microstructure evolution during freeze casting.

	Additive	Freezing Conditions				Suspension Solids Loading	Particle Size
		Temperature	Rate	Time	Heat Transfer		
Homogeneous Microstructure	Glycerol: improves microstructure homogeneity, integrity; Gelatin: improves microstructure homogeneity; Clay: improves microstructure homogeneity, increase pore size.	Numerous small pores evolve into fewer larger pores with increase in temperature; Study range: -196ºC to -18ºC.	High rate leads to small pore size and liquid like microstructure. Study range: 0.05ºC/min to cooling from room temperature into liquid propane (-196ºC).	Longer time leads to dendritic microstructure and larger pores.	High heat transfer efficiency leads to interconnected and dendritic microstructure.	High solids loading leads to porosity decrease and pore morphology evolution; Study range: 5 to 60 vol%.	Small particle size (submicron) is desirable for homogeneous microstructure and fine features.

Table 2-1. Summary of critical factors affecting porous microstructure evolution during freeze casting (continues).

Directional Microstructure	Glycerol: refines microstructure and decrease pore size; Dioxane: lamellar microstructure evolves to cellular pores, refined microstructure; Polyvinyl alcohol: refines microstructure, dendrites evolve to columns; Polyethylene glycol: increases local supercooling and refined microstructure, promotes ripening of secondary tips and increase pore size.	Temperature increase results in pore evolution from lamellar to dendritic to tortuous, affects pore size by decreasing particle rejection efficiency while promoting crystal growth. Study range: -196ºC to -18ºC.	High rate leads to finer microstructure. Study range: 2ºC/min to cooling from room temperature into liquid propane (-196ºC).	Longer time promotes directional microstructure.	High efficiency promotes directional microstructure.	High solids loading leads to porosity decrease; fine structure; particle hindrance increase; Study range: 5 to 60 vol%.	Small particle: easily repelled; promote directional structure; refine microstructure.

chilled plate is under a constant temperature, but the upper side is exposed to ambient conditions, where the temperature decreases with time in an uncontrolled manner. The ice solidification velocity decreases with time and the pore size varies with holding time. For double-sided freezing, the upper and lower plates are set at specific temperatures; the solidification velocity can be controlled. Accordingly, homogeneous lamellar structures are obtained. By this approach, unique lamellar structures with varying spaces can also be created by modifying the upper and lower plate temperatures.

Freeze tape casting is a technique to obtain vertically graded porous structures for large area tape samples. Similar to traditional tape casting, the suspension is first cast onto a casting bed through a doctor blade assembly. Then, the casting bed is moved into a freezing zone to realize directional freeze casting (Fig. 2-13).[90] This technique is effective in fabricating graded and aligned porous microstructures and the pore morphology can be adjusted by controlling the freezing conditions and the bed temperature.

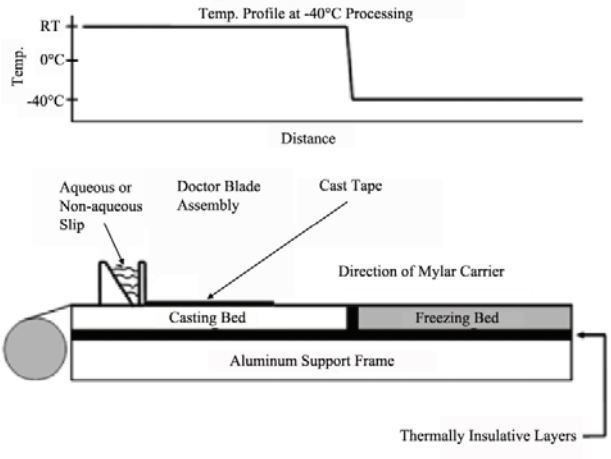

Fig. 2-13. Schematic of freeze tape casting. (Reprinted from *Journal of the American Ceramic Society*, Vol 90/Issue 7 (2007), Sofie, Fabrication of Functionally Graded and Aligned Porosity in Thin Ceramic Substrates With the Novel Freeze–Tape-Casting Process, Copyright (2012), with permission from John Wiley and Sons[90])

Field-directed freeze casting uses a specific external field to modify the ice solidification and particle ejection directions. This technique has been used to fabricate dense/porous bilayered composites and the thickness of the dense layer can be efficiently controlled by the applied field.

The most common field-directed freeze casting is through an electric field. One example suspension contains 20 vol% alumina particles in a water-glycerol mixture.[113] The measured zeta potential of the alumina suspension is -49 mV, indicating that the alumina particles are negatively charged. Under an electric field (15 to 90 V), the negatively charged alumina particles move toward the anode and cause a stratification of solid concentration. At the beginning of the electric field-directed freeze casting, the ice front velocity is higher than the critical value and most alumina particles are engulfed by the ice front. Those particles that are repelled by the solidification front accumulate at the interface. When the alumina particle concentration at the interface increases to a certain value, the ice front velocity is lower than the critical value, the solidification front breaks down and ice dendrites form. The high suspension solids loading near the anode leads to a dense layer while the low solids loading away from the anode results in a dentritic porous microstructure with growing ice crystals rejecting the solid particles more effectively. Therefore, a gradient dense/porous structure is fabricated.[111] Fig. 2-14 shows the microstructure evolution when the voltage increases from 15 V to 90 V. The thickness of the dense layer continuously increases from 51 to 155 μm with the voltage and can be effectively controlled.

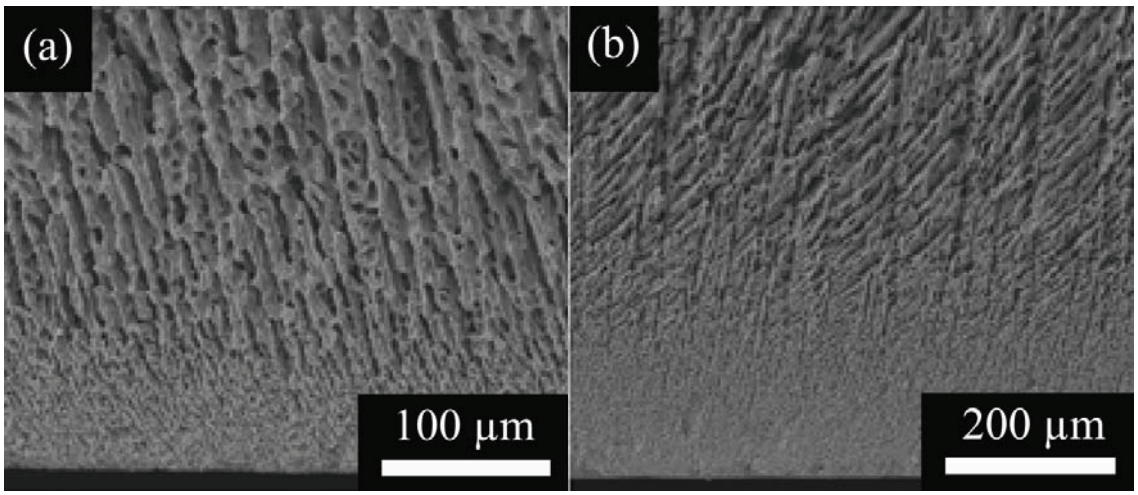

Fig. 2-14. SEM images for the cross-sections of the alumina samples prepared with different electric field strength: (a) 15 V, (b) 90 V. (Reprinted from *Journal of the American Ceramic Society*, Vol 92/Issue 8 (2009), Zhang *et al.*, Preparation of a Dense/Porous BiLayered Ceramic by Applying an Electric Field During Freeze Casting, Copyright (2012), with permission from John Wiley and Sons[113])

The above discussed novel freeze casting techniques are mostly based upon aqueous systems. However, they can be applied to non-aqueous systems since the fundamental principles are the same. The key factors that influence the aqueous systems can be similarly discussed for non-aqueous systems. On the other hand, although these techniques are mostly designed for directional freeze casting, homogeneous freeze casting can also be improved by inversely considering the mentioned conditions and designs.

2.2.4 Issues and perspective

Thanks to its versatility and flexibility in the fabrication of porous materials with controllable porous structures, freeze casting technique has a promising perspective in both scientific study and industrial applications. Based on the current research activities and understanding, the future development in this area will likely advance along the following aspects.

First, although many efforts have been devoted to the freeze casting technique in recent years, a general model for predicting porous microstructure and morphology for different systems is not presently available. To my best knowledge, very limited simulation study has been reported on freeze casting. As a result, a proper and effective way of controlling the microstructure needs to be separately evaluated for a given system. For multi-component systems, the freeze casting process is further complicated because different particles will hinder the ice growth and particle arrangement differently. In order to establish general models which can quantitatively describe the relationship between critical factors and porous structures, more theoretical and simulation studies are needed.

Second, post-processing techniques are requested to improve the overall properties of the freeze cast porous materials. Due to the intrinsic solidification behaviors of the dispersing media, the typical pore size of freeze cast porous materials is limited to a narrow range from 1 μm to 100 μm. This limitation not only frames the restraint of the pore structure, but also indicates the specific surface area of the freeze cast materials cannot be desirable. In addition, sintering is always requested to reinforce the scaffold of the freeze cast porous materials. This application of heat would inevitably further decrease the active surface area. Since these issues are associated

with the intrinsic properties of the freeze casting technique, proper post-processing techniques may be introduced to further improve the overall properties of the freeze cast porous materials.

Third, the fundamental principles of freeze casting are closely related to heterogeneous nucleation and growth and can be applied to any species that are stable in the specific dispersing medium. Because of the widespread use of water as the dispersing medium, the main activities in this area are in ceramics. With proper care, it should be possible to freeze cast metals and even polymers or their composites. For instance, oxidation of metal particles should be avoided; polymer should not be soluble but should be dispersible. Several studies have been carried out on the freeze casting of metals and polymers.[114] Modeling indicates that the pore size is dependent on the freezing front velocity and the temperature gradient.[114] The interaction between chains should be considered for polymer freeze casting. For multi-composition suspensions, a proper co-dispersion system and a good understanding of different particle-solidification front interactions are necessary. Chitosan gelatin-graphene oxide is an example of freeze cast composites.[115] Key factors such as pH values, additives, suspension compositions, and solids loading are investigated. However, the interactions between species, freezing conditions, and the above key factors need to be established. The extension of freeze casting to these kinds of materials will open up new opportunities in fundamental science as well as applications.

2.3 Sintering of nanoparticle-based porous materials

As discussed above in the experimental procedure of the freeze casting technique (section 2.2.1.1), sintering is always applied to the freeze-cast green samples to remove the micropores in the pore walls while keep the macropores that fabricated by sublimating of the dispersing media. Sintering is a necessary process for most porous materials as their green state is always too fragile for actual applications. Compared to larger grain powders, sintering of the nanoparticle-based porous materials should be carefully controlled to achieve maximum reinforcement of the solid framework while maintaining the macroporosity.

2.3.1 Thermodynamic driving force and grain growth

Sintering of nanoparticle-based porous materials can be defined as the bonding of the particles along the solid framework by atomic diffusion with the application of heat to build a

solid-pore bi-continuous structure with a coherent solid network. The driving force of sintering is the reduction of the particle surface energy by decreasing the particle-pore interface. According to the conventional sintering theories, the thermodynamic driving force for particle with the principle radii R_1 and R_2 can be expressed by[116, 117]

$$\sigma = \gamma\kappa = \gamma\left(\frac{1}{R_1} + \frac{1}{R_2}\right) \tag{2-6}$$

where γ refers the surface energy, κ refers to the curvature of the surface. On this basis, the driving force for sintering of nanoparticles is much higher than particles with size larger than one micrometer. In addition, the specific surface energy (γ) also depends on particle size.[117] Scientists reported that the specific surface area of the nanoparticles is significantly higher than that of the bulk material, especially when particle size lower than 3 nm.[117-119] As a result, the driving force for sintering of the nanoparticles is extremely high. The sintering temperature and grain growth for nanoparticles are therefore different from the larger particle powders.

Shown in Fig. 2-15 is the schematic diagram illustrating the onset sintering temperatures for particles with nano- and micron size. Although the starting sintering temperature is not a single point, the onset sintering temperature is hereby defined as the temperature at which the rapid densification occurs.[115] It is obvious that the densification versus temperature plot shifts left when particle size decreases, and the onset sintering temperature for nanoparticles is much lower than that of micron sized particles.

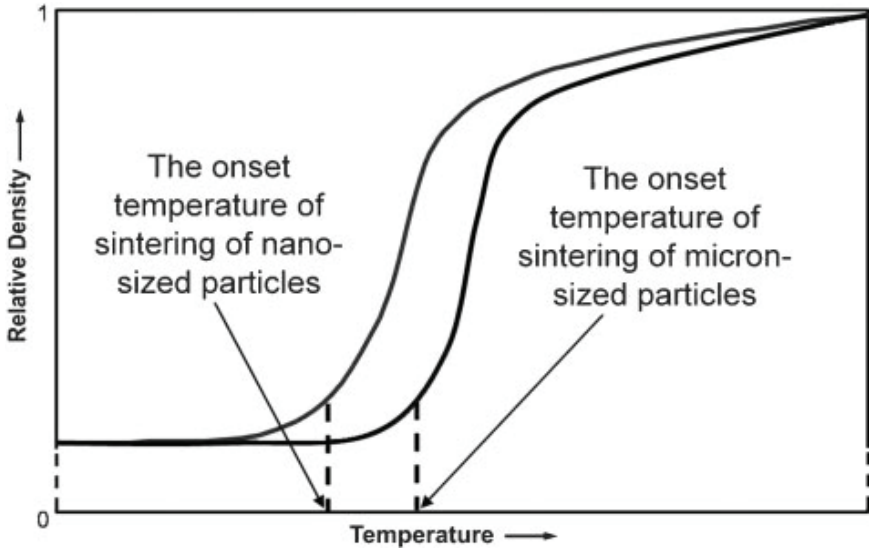

Fig. 2-15. Schematic diagram illustrating different onset sintering temperatures of nano- and micron sized particles. (Reprinted from *International Materials Reviews*, Vol 53/Issue 6 (2008), Fang *et al.*, Densification and grain growth during sintering of nanosized particles, Copyright (2012), with permission from Maney Publishing, www.ingentaconnect.com/content/maney/imr, www.maney.co.uk/journals/imr[117])

Another important principle related to sintering of nanoparticles associates with the grain growth, which strongly depends on the temperature. With the increase of temperature, the initially slow grain growth speeds up dramatically when the temperature passes a critical value.[117] Although this critical temperature can hardly be defined as a switch-on temperature, the grain growth before this temperature is very slow.[120, 121] According to the discussion above concerning the sintering driving force, this critical temperature is lower for nanoparticles. Rapid grain growth always occurs for sintering of nanoparticles even before reaching the isothermal holding temperature. From another point of view, the extensive grain growth during sintering mainly occurs in the final stage where the porosity is lower than 10%. Since the sintering of nanoparticle-based porous materials always falls in the initial and intermediate stages to maintain the major porosity, this final stage is the least factor that should be considered for sintering of porous materials.

2.3.2 Characteristics and challenges

Although the sintering of nanoparticle-based porous materials shares many basic principles with the conventional sintering (e.g. diffusion mechanism, grain growth rules), unique characteristics and potential issues appear as a result of the small size effects. The sintering conditions should be even more carefully designed as to reinforce the porous framework while maintaining the major porosity.

The sintering temperature for nanoparticle-based porous material should be carefully controlled. Again, the small particle size and high specific surface area greatly enhance the thermodynamic driving force while lowering the sintering temperature. The onset sintering temperature for nanoparticles ranges from $0.2T_m$ to $0.3T_m$, compared to that of the micro-sized particles from $0.5T_m$ to $0.8T_m$ (T_m is the melting point of the sintering species in Kelvin).[122-125] For the sintering of porous materials, the isothermal holding temperature may be even lower to

prevent the formation of any liquid phase. Since the liquid phase would result in rapid densification and destroy porous structures without any preference, sintering of porous materials can only involve solid state sintering.

The introduction of extremely high specific surface area due to the reduction of particle size may bring in potential issues. The high surface energy promotes the spontaneous agglomeration. On the one hand, agglomeration consumes the driving force and inhibits the grain growth. On the other hand, agglomeration produces inter-agglomerate pores that could be hardly to remove throughout the sintering process.[123] The formation of agglomeration could especially damaging for producing porous materials, as either the hindrance of the grain growth or the minor pores within the solid framework could significantly damage the reinforcement effect of sintering.

When the particle size decreases to nanometer, the particle size tends to be polydispersed as there are challenges for both synthesis and separation. The wide size distribution brings in problems for particle packing and subsequent grain growth. The homogeneity of the densification could be damaged.

2.3.3 Typical sintering methods

Traditionally, sintering is aimed to form a coherent, predominantly solid structure and achieve full density by the application of heat. To accelerate the densification, external conditions have been applied and therefore a variety of sintering methods have been developed besides the conventional pressureless sintering, such as pressure sintering (e.g. hot pressing, hot isostatic pressing, and sinter forging), electrically assisted sintering (e.g. spark plasma sintering and microwave sintering), plasma spray forming, and dynamic compaction. [123] The inter-particle bonding is improved by the applied pressure, current, or electromagnetic radiation, and fast and full densification can be easily achieved.[126] However, these novel sintering methods are always a disaster for producing porous materials. The designed porous structure can be damaged or completely eliminated by the enhanced densification and the green porous samples may be too fragile to afford any external pressure. According to the conventional theories, sintering process can be divided into three stages, the initial stage, the intermediate stage, and the final stage, with relative density of ~65%, ~90%, and ~100%, respectively.[122, 127] On this basis, the sintering of porous materials can be viewed as a shortened process of the traditional sintering, only involving

the initial and/or the intermediate stage. Typically, the sintering of nanoparticle-based porous materials can be categorized into partial sintering and sacrificial templating sintering.

The so-call partial sintering is a shortened version of pressureless sintering, including the early sintering stages. This technique is advantageous for its simple equipment, cost-efficiency, and capability in forming samples with complex shapes.[123] The schedule of the pressureless sintering should be carefully controlled as the reduction of the surface energy is the only driving force. The heating rate, isothermal holding temperature, holding time, and second phase governs the sintering stages and determines the dominance between densification and grain growth. Various sintering approaches have been developed to control the relative contribution of densification and grain growth, such as two-step sintering where a high temperature sintering step followed by a prolonged isothermal holding at low temperature.[128] Theoretically, the sintering mechanisms without densification are desirable for the fabrication of porous materials. Mechanisms (i.e. surface diffusion and evaporation-condensation) result in neck growth without densification are ideal.[122, 129] In contrast, the grain growth should be suppressed by densification with respect to manufacturing bulk nanocrystalline materials.[117] With this purpose, volume diffusion and grain boundary diffusion are preferred. In combination, the sintering schedules have to be particularly designed to fabricate materials with specific structures. For porous nanocrystalline materials, the partial sintering should remove the minor pores throughout the solid framework while conserving the macropores.

Sintering of nanoparticle-based porous materials can also experience a sacrificial templating process.[130-132] A typical fabrication procedure is shown in Fig. 2-16. Well-dispersed suspension containing raw nanoparticles and sacrificial template (e.g. polymer) is first obtained. The nanoparticles and the sacrificial template possess opposite charges and a core-shell polymer/nanoparticle structure can be fabricated. Through vacuum filtration and followed drying processes, the green sample forms. Afterward, heat is applied to the green sample and the sacrificial template is burn-out followed by a higher temperature sintering step. The mechanisms and criteria are the same as those of the partial sintering discussed above.

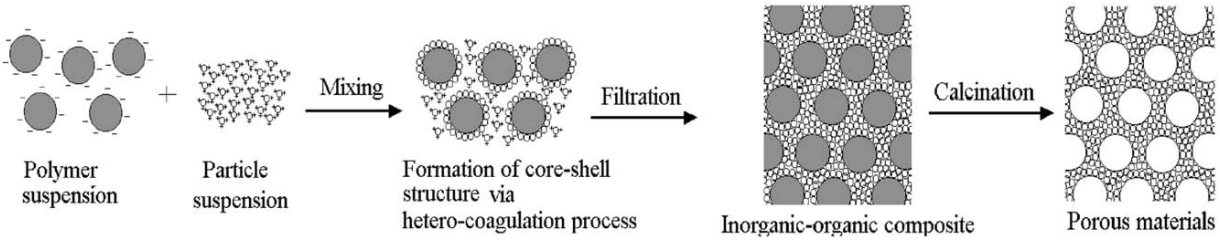

Fig. 2-16. Schematic illustration for fabrication of porous materials via sacrificial (polymer) templating sintering. (Reprinted from *Journal of the European Ceramic Society*, Vol 24/Issue 2 (2004), Tang *et al.*, Preparation of porous materials with controlled pore size and porosity, Copyright (2012), with permission from Elsevier[130])

The sintering technique that applied to the freeze-cast green samples is generally partial pressureless sintering. The freeze-cast green samples are not strong enough to afford external pressures and accelerated densification is not desirable as the major porosity should be conserved. The freeze casting and followed sintering in combination can be viewed as a type of sacrificial templating approach that fabricates porous materials with adjustable microstructure. It should be mentioned that electrically assisted sintering can also been used to produce porous materials. For instance, porous alumina was reported to be fabricated by spark plasma sintering.[133] However, the porosity created through this approach dues to the shrinkage associated with reactions during sintering. Specifically, it is the decomposition of the raw material ($Al(OH)_3$) and the phase transformation (from θ-alumina to α-alumina) that result in volume change and subsequently lead to formation of pores. Since the sintering work of this proposed project is applied to freeze-cast materials, this unique technique is not elaborated.

2.4 Applications of porous materials

In the past decades, fabrication, characterization, and application of porous materials have drawn considerable attention. In general, the porous materials can be classified into two groups according to the characteristics being utilized.[5] The first category refers to those applications exploiting the porosity itself. The porous spaces can either be used as a host scaffold to confine certain environments or applied to modify the macro-properties, such as dielectric constant.[6, 7] The second group relies on the properties associated with the porosity. For example, the high specific surface area allows enhanced interactions with foreign species,[8, 9] while

designed pore size and morphology provide selective passing for particles.[2-4, 32] The recent achievements in the study of porous materials have broadened their applications in separation, adsorption, catalyst support, sensing,[1-3] and extended to new fields such as biotechnology, medical diagnosis, and microelectronics. [4-10]

Ceramic membranes, typical porous materials, are widely used in many fields, such as ion-exchange electrodes,[134] electromechanical actuators,[135] insulating layers,[136, 137] oil spill cleanup,[138] chemical sensors,[139-141] light harvesting devices,[142] and gas/liquid separation.[1] These applications capitalize on their controllable porous microstructure, chemical/thermal stabilities, long operation live, well-defined surface properties, and high cleanability.[1] Nowadays, with the development of the nanotechnology and better understanding of surface chemistry for ceramics (e.g. silica, alumina, and titania), the porous structure can be precisely controlled and inorganic membranes can be functionalized by a variety of molecules. As a result, their applications, such as in wastewater treatment, filtration, and bioengineering, are greatly promoted.

CHAPTER 3. FREEZE CASTING OF THE KAOLINITE-SILICA NANOCOMPOSITES*

Abstract

This chapter is focused on understanding the effects of kaolinite content and freezing rate on the microstructure, surface area, and flexural strength of freeze-cast kaolinite-silica nanoparticle composites. Scanning electron microscopy reveals that the bulk of the composites contain interconnected pores and that the size of the pores increases with kaolinite concentration. Lowering the freezing rate from 2.0°C/min to 0.05°C/min produces much larger pores on the outer surface of the sample and only minor effects on the bulk morphology. BET measurements indicate that the specific surface area (area/mass) of the composites is controlled primarily by the relative amounts of kaolinite and silica in the sample and not by the freezing rate. Equibiaxial flexural strength tests show that the strength of the composites is substantially higher than freeze-cast samples produced using either kaolinite only or silica only, indicating that the two components work cooperatively. The strength is slightly higher for composites produced at the lower freezing rate. Adsorption tests indicate that during gel formation, the silica nanoparticles strongly adsorb to the much larger kaolinite platelets, which could be the primary cause for the increased strength of the composites.

3.1 Experimental procedures

3.1.1 Raw materials and sample preparation

In this study, 34 wt% silica nanoparticle suspension (Ludox TMA, Sigma Aldrich, St. Louis, MI), sodium chloride (AR grade, Mallinckrodt, Paris, KY), kaolinite (Hydrite Flat-D, Imerys Performance Materials, Dry Branch, GA), and de-ionized water were used to prepare kaolinite-silica gels. The silica nanoparticles had a nominal diameter of 22 nm and a density of 2.37 g/cm^3.[144, 145] The specific surface area of the silica was reported by the manufacturer as ~140 m^2/g, however calculating this property using the size and density (i.e., $A_{sp} = 3/\rho R$, where ρ is the particle density, R is particle radius, and A_{sp} is the specific surface area) yielded a value of

* Chapter 3 was published in *Journal of the American Ceramic Society 2011, **94**(4), 1256-1264*[143]

approximately 115 m^2/g, which agreed well with BET measurements reported below. The particles were well dispersed in de-ionized water. The kaolinite particles were composed of thin platelets and quite polydisperse, with observed diameters ranging between 200 nm and 6 μm and a thickness at 50-200 nm. The density of the kaolinite, obtained by measuring the volume of water displaced by a known mass of added clay, was 2.56 g/cm^3, and the manufacturer reported specific surface area was 7 m^2/g.

Desired amounts of silica nanoparticle suspension and de-ionized water were mixed in a vial using a vortexer (Fisher Scientific Inc, Bohemia, NY). The kaolinite particles were added into the suspension, followed by 1 min mixing. Finally, a specific amount of NaCl solution of 5 M concentration was introduced and the mixture was homogenized for another 1 min. A series of samples with kaolinite concentrations of 0 vol%, 6 vol%, 10 vol%, and 14 vol% were prepared. The total solids concentration (kaolinite plus silica) was kept at 18% vol., meaning that as the kaolinite concentration increased, the silica concentration decreased. The NaCl concentration in all samples was 0.5 M. The specific compositions of each of the samples used in this study are given in Table 3-1.

Table 3-1. Compositions of samples used in this study.

Kaolinite (vol%)	Silica (vol%)	NaCl (M)
0	18	0.5
6	12	0.5
10	8	0.5
14	4	0.5

After mixing, the suspension was poured into small aluminum foil containers (8 mm diameter, 3 mm deep, sample volume of approximately 0.15 cm^3) and large silicone rubber containers (31 mm diameter, 2 mm deep, sample volume of approximately 1.5 cm^3) and held there for 4 hrs to allow gelation. The small samples were used for microstructure observations and surface area measurements, while the large ones were designed for flexural strength tests. The gelation times of solutions with 0, 6, 10 and 14 vol% kaolinite were 30 min, 10 min, 5 min, and > 8 hrs, respectively. (The gelation time is defined here as the time at which the sample would no longer flow upon inverting the sample holder.) The holding time was chosen to be 4

hrs to allow sufficient time for the silica nanoparticles and kaolinite platelets to interact while also minimizing sedimentation. Note that the samples containing 14 vol% kaolinite would typically not gel within the 4-hour holding time, however the sample was sufficiently viscous that little sedimentation of the kaolinte was observed.

After 4 hours, the gels (and containers) were placed into an Advantage Freeze Dryer (SP Industries VirTis, Gardiner, NY) to execute freezing and sublimation. The samples were first cooled to -35°C with freezing rates of 2.0°C/min, 1.0°C/min, and 0.05°C/min respectively and then held at -35°C and ~1.34 Pa for 400 min to sublimate the ice. (For purposes of brevity, only the results obtained at 2.0°C/min and 0.05°C/min are presented here for microstructure and flexural strength analyses.)

3.1.2 Characterization

The microstructures of the freeze-cast composites were observed using a field emission scanning electron microscope (SEM, LEO1550, Carl Zeiss MicroImaging Inc., Thornwood, NY). The freeze-cast samples were coated with 15-20 nm Au-Pt layer before examination. Images of both the top and interior (cross-section) surfaces of the composite samples were obtained (the cross-sections were obtained by breaking the samples by hand and imaging one of the exposed surfaces). Specific surface area and pore volume/size analyses were carried out by nitrogen adsorption (Autosorb-1 C, Quantachrome Instruments, Boynton Beach, FL). The equibiaxial flexural strength of the freeze-cast composites was measured by a strength test apparatus with a 1 kN load cell (Instron 4204, Instron, Norwood, MA). The schematic diagram of the strength test setup is shown in Fig. 3-1. The test was a two-dimension bending compressive strength measurement with 360° rotation about the load axis, which followed ASTM C 1499.[146] The crosshead was lowered at a speed of 0.1 mm/min until the sample was broken. The equibiaxial flexural strength was calculated as

$$\sigma_f = \frac{3F}{2\pi h^2}\left[(1-\nu)\frac{D_S^2 - D_L^2}{2D^2} + (1+\nu)\ln\frac{D_S}{D_L}\right] \tag{3-1}$$

where σ_f is the equibiaxial flexural strength, F is breaking load, h is specimen thickness, ν is Poisson's ratio, D is sample diameter, D_S is support ring diameter, and D_L is load ring diameter.

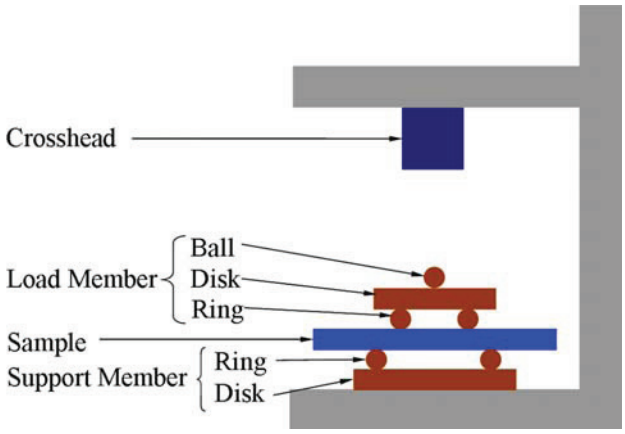

Fig. 3-1. Schematic diagram of equibiaxial flexural strength test apparatus.

3.2 Results and discussions

3.2.1 Microstructure Evolution

The top surface microstrucutres of the freeze-cast composites with 2.0°C/min freezing rate are shown in Fig. 3-2. Since all the samples have the same total solid concentration, differences in the microstructure should result only from the relative amount of kaolinite and silica comprising the sample. With no added kaolinite (Fig. 3-2a), very distinct and connected pores are observed, with visible pores as large as 50 μm. As the kaolinite concentration increases, fewer and fewer pores are observed on the surface. It can also be seen that the pores take on a longer and narrower shape, with the pore width decreasing from tens of microns with no added kaolinite to 1 - 2 μm with 14 vol% kaolinite (Fig. 3-2d).

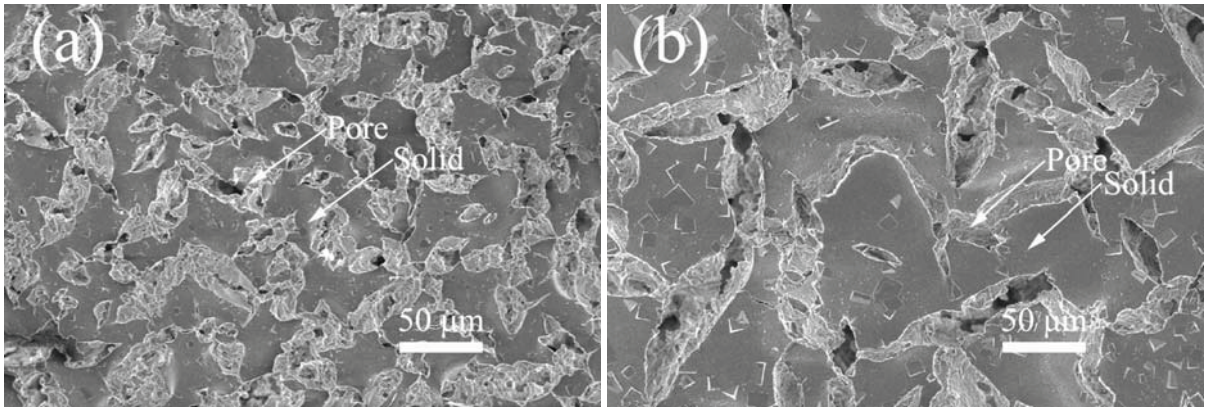

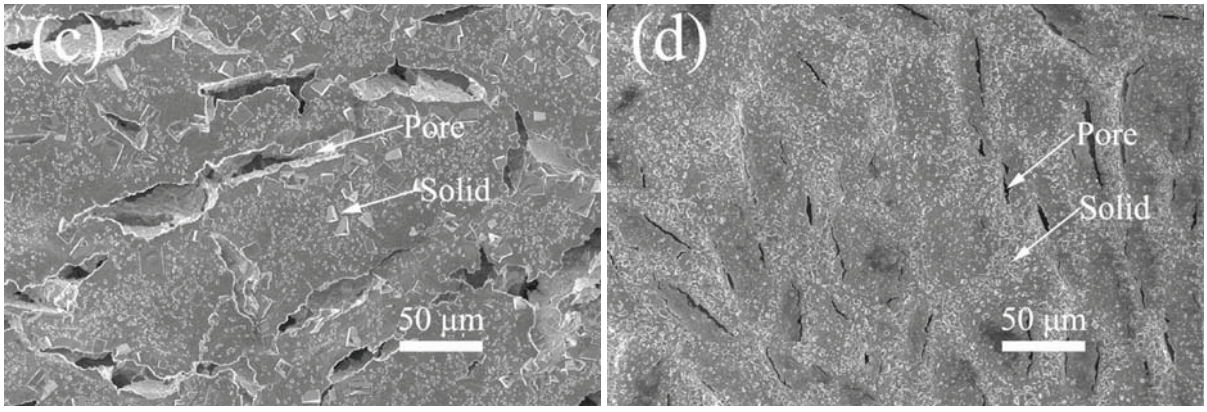

Fig.3-2. Top surface SEM images of 2°C/min freeze-cast composites with different kaolinite concentrations: (a) 0 vol% kaolinite, (b) 6 vol% kaolinite, (c) 10 vol% kaolinite, (d) 14 vol% kaolinite. The scale bar is the same in all figures to facilitate comparisons.

Fig. 3-3 shows the cross-section microstructures of the 2.0°C/min freeze-cast samples. Again, these images were obtained by manually breaking samples of the freeze-cast composites and then imaging one of the exposed surfaces. For the sample with no kaolinite (Fig. 3-3a), pores with an average diameter of 5 μm, are prevalent. With kaolinite addition (6 vol%), pores grow larger (> 10 μm), with the large kaolinite particles forming the pore walls. This can be seen more clearly in the high magnification image for one of the pore walls shown in Figure 3-3e. Further increases in pore size are observed with the 10 vol% kaolinite sample (Fig. 3-3c). With 14 vol% kaolinite, the pore size has increased to 25 μm, and the connectivity between the pores appears to be improved.

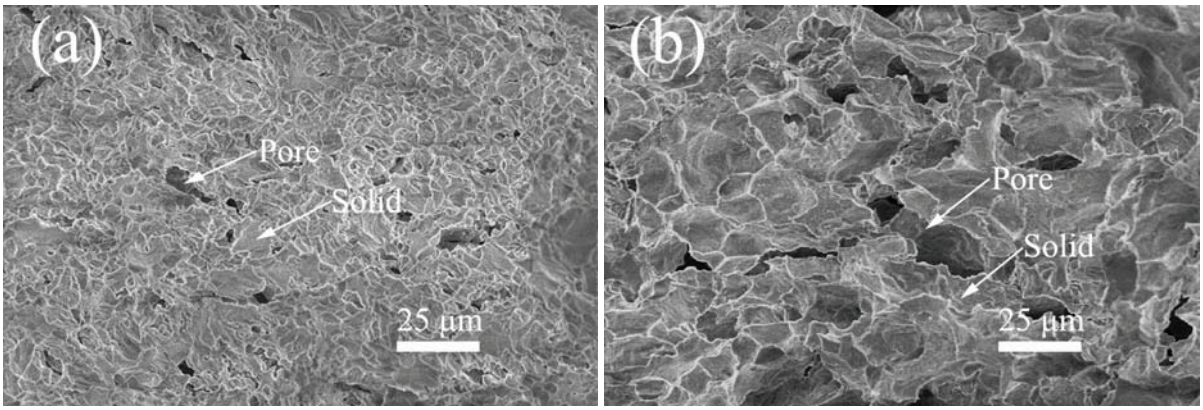

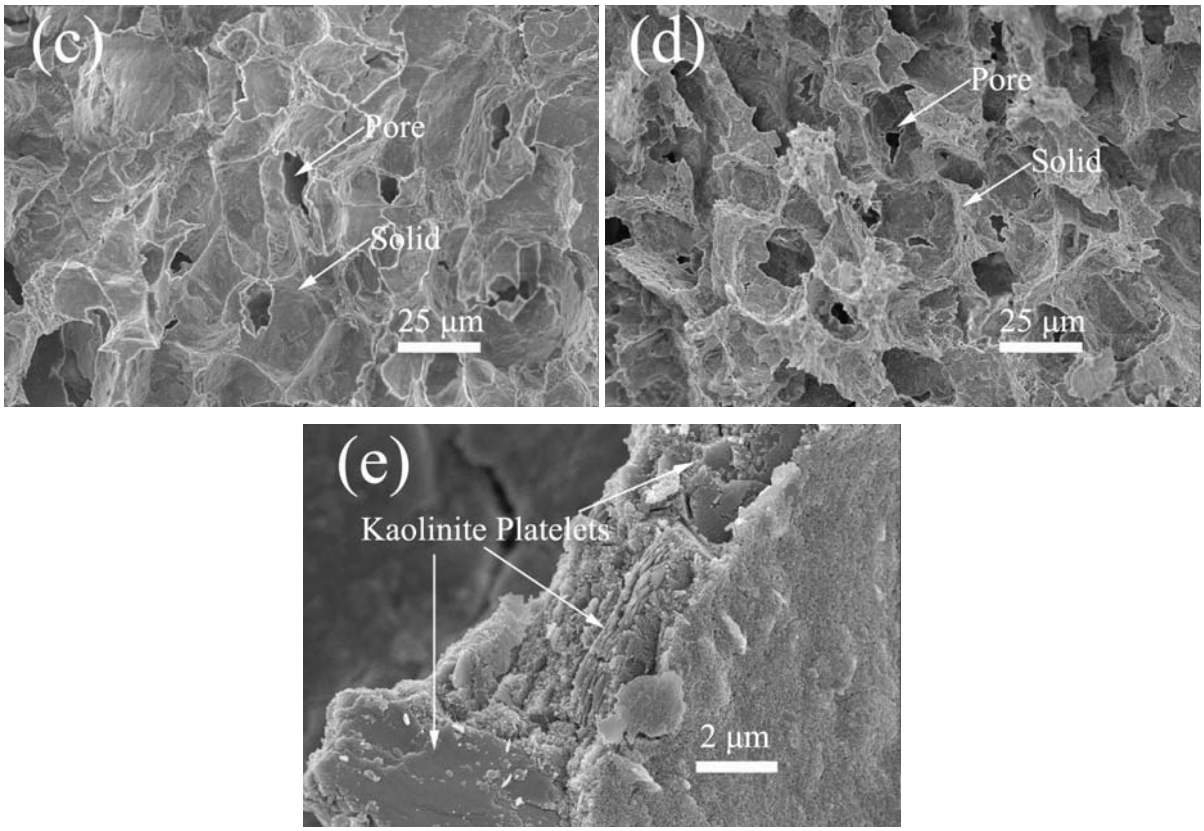

Fig. 3-3. Cross-section SEM images of 2.0°C/min freeze-cast composites with different kaolinite concentrations: (a) 0 vol% kaolinite, (b) 6 vol% kaolinite, (c) 10 vol% kaolinite, (d) 14 vol% kaolinite; (e) 10 vol% kaolinite under high magnification showing the wall of one of the pores.

Fig. 3-4 shows the top surface images of 0.05°C/min freezing rate samples. The overall trends are the same as those observed with the 2.0°C/min freeze-cast composites (Fig. 3-2), namely that the pores become more isolated and less numerous as the kaolinite concentration increases, however the changes are not so pronounced. Unlike the surface of the 2.0°C/min samples shown above, increasing the kaolinite concentration here does not have a substantial impact on the dimensions of the pore. The main tendency seen is the decreased connectivity of the surface pores as the kaolinite concentration increases, with the highly connected pores in Fig. 3-4a evolving into more isolated pores in Fig. 3-4d.

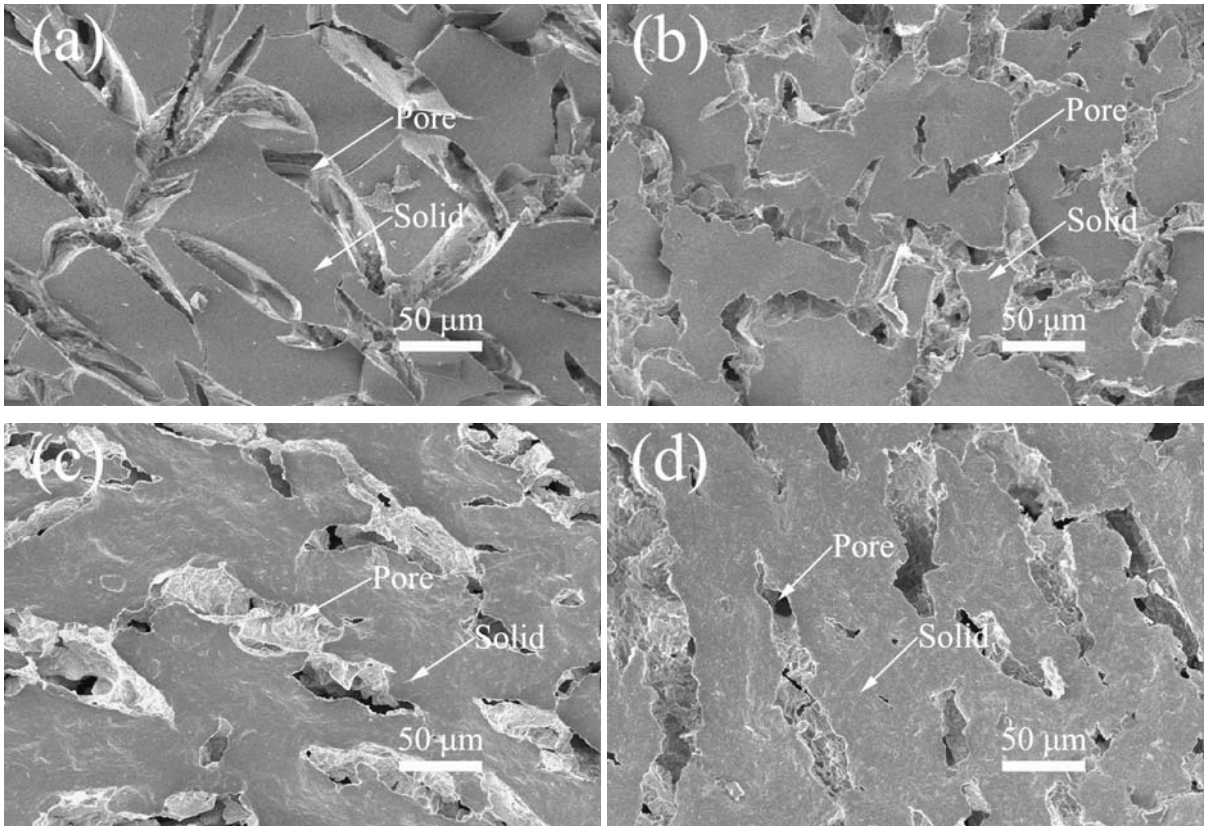

Fig. 3-4. Top surface SEM images of 0.05°C/min freeze-cast composites with different kaolinite concentrations: (a) 0 vol% kaolinite, (b) 6 vol% kaolinite, (c) 10 vol% kaolinite, (d) 14 vol% kaolinite.

Comparing Figs. 3-2 and 3-4 also shows that in samples containing only silica nanoparticles (0 vol% kaolinite), lowering the freezing rate creates larger isolated pores. Although pores evolve from interconnected shape into isolated narrow ones for both freezing rates, the samples frozen at 2.0°C/min have significantly smaller pore widths. A more open porous structure forms on the top surface of the samples frozen at 0.05°C/min.

For the samples freeze-cast at 0.05°C/min freezing rate, the cross-section microstructures (Fig. 3-5) show that the pore size increases with the kaolinite concentration, similar to what was observed for the 2.0°C/min samples. For the pure silica sample (Fig. 3-5a), only a few thin pores are visible, while much larger pores (10 – 20 μm) become apparent as the kaolinite concentration increases from 6 vol% to 14 vol% (Figs. 3-5b-d). It should be emphasized that because all of the samples contained roughly the same volume fraction of solids, and since no significant

expansion of the samples was observed to occur during freeze-casting, the actual bulk porosity in all samples was approximately the same (around 82% volume). Thus in Fig. 3-5a, the void space consists primarily of very tiny pores that cannot be visualized at this magnification. A much higher magnification image of this sample is provided below in Fig. 3-5e. The very small pores are now clearly evident.

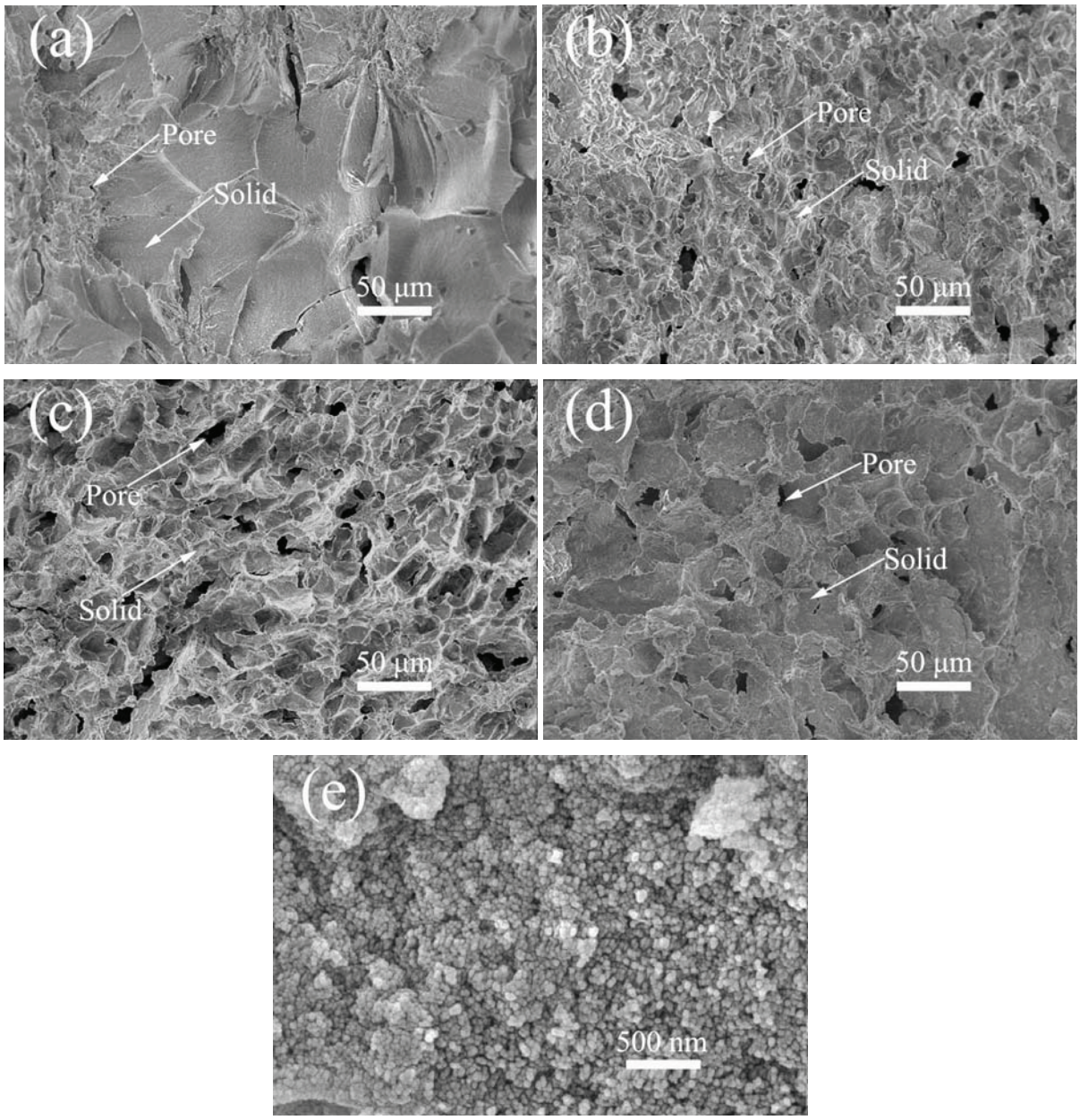

Fig. 3-5. Cross-section SEM images of the 0.05°C /min freeze-cast composites with different kaolinite concentrations: (a) 0 vol% kaolinite, (b) 6 vol% kaolinite, (c) 10 vol% kaolinite, (d) 14

vol% kaolinite; (e) 0 vol% kaolinite at high magnification. The majority of the pore volume in Fig. 3-5e appears to consist of very small pores between the silica nanoparticles.

A summary of the observations obtained from the SEM images is provided below in Table 3-2. It is clear that in the cross-sections, the size of the pores increases substantially with added kaolinite. Little difference between the pore size and pore morphology are observed at the two different freezing rates.

Table 3-2. Trends observed in SEM images of freeze-cast composites.

Freeze-rate	Top Surface	Cross-section
2.0°C/min	As kaolinite concentration increases, pores become very thin, more isolated, and much fewer in number.	As kaolinite concentration increases from 0 vol% to 14 vol%, pore size increases from ~5 μm to ~ 25 μm. Pores also become more interconnected, and kaolinite particles form the walls of the pores.
0.05°C/min	As kaolinite concentration increases, pores become more isolated, however pore size and shape do not significantly change.	With no kaolinite, pores are extremely small, existing mainly between the nanoparticles. As kaolinite concentration increases, pore size increases significantly.

Freezing-rate appears to have a much larger impact on the morphology of the surface of the samples. Specifically, with no added kaolinite, the surface of the samples frozen at 2.0°C/min shows highly connected pores with a variety of sizes and shapes, while the surface of samples frozen at 0.05°C/min displays much larger pores with highly elongated shapes. At 14 vol% clay, samples frozen at 2.0°C/min have extremely thin, almost 'thread-like' pores on the surface, while much larger pores are clearly visible on the sample frozen at 0.05°C/min.

The exact causes for these trends can only be hypothesized. Since the applied freezing rates were relatively low and the thicknesses of the samples were very small, the temperature gradient throughout the samples was not significant and the anisotropic growth of ice crystals was not favored. In addition, samples were frozen under their gelled states (viscosity of 14 vol%

kaolinite sample is sufficiently high) where the particle hindrance effectively offsets the ice front expulsion. Therefore, homogeneous microstructures were fabricated. The microstructure was composition dependent since the ice nucleation and growth were affected by the particles. Specifically, the nanoparticles possess much larger specific surface area and provide more liquid-solid interfaces, which is able to reduce the nucleation barrier. Since the total solid concentration for all the samples were kept the same, the number of nucleation sites decreases dramatically with kaolinite content increase. Thus, numerous small pores appeared in pure silica samples as the nucleation was more likely to occur. At lower freezing rate, the ice nucleation and growth processes were given more time to occur; however, because of their large size and planar shape combined with gelled state, the kaolinite platelets were much more difficult to expel, causing the growing ice-front to become broken and distorted. As a result, little microstructure difference was observed on the cross-sections for various freezing rates. Macropores were more likely to be found on the top surface of lower freezing rate samples because the mobility of particles on the free surface is much higher and allows particles to rearrange.

3.2.2 Nitrogen Adsorption Measurement

The specific surface area vs. kaolinite concentration of the resulting composites is given in Fig. 3-6. The hysteresis of the adsorption and desorption isotherm curves for the sample with 10 vol% kaolinite (as a representative) as a function of relative pressure is shown in the insert. The samples show the classical type II isotherm. The dashed line in Fig. 3-6 shows the specific surface area calculated by assuming the surface area is conserved from the kaolinite and silica particles upon freeze casting. Specifically, the surface area for the composite sample can be calculated using

$$S = \frac{S_{kaolinite}\rho_{kaolinite}\psi_{kaolinite} + S_{silica}\rho_{silica}\psi_{silica}}{\rho_{kaolinite}\psi_{kaolinite} + \rho_{silica}\psi_{silica}} \quad (3\text{-}2)$$

where S is the calculated specific surface area, $S_{kaolinite}$ and S_{silica} refer to specific surface area of kaolinite and silica nanoparticles, $\psi_{kaolinite}$ and ψ_{silica} refer to kaolinite volume fraction and silica volume fraction, $\rho_{kaolinite}$ and ρ_{silica} are density of kaolinite and silica, respectively. For the specific surface area of the kaolinite, I used the manufacturer-reported value of 7 m^2/g, while for the silica I used the value of 115 m^2/g calculated from the known density and particle size. The calculated curve is very consistent with the measured values for the freeze-cast samples,

indicating that no significant loss of area occurs during gelation and freeze-casting. For the samples produced at the three different freezing rates, the specific surface area decreases almost linearly from 115 m^2/g to 35 m^2/g with the increase of kaolinite concentration from 0 vol% to 14 vol% Since the total solid concentration is kept at 18 vol%, the decrease of the specific surface area is a direct result of the silica concentration decrease.

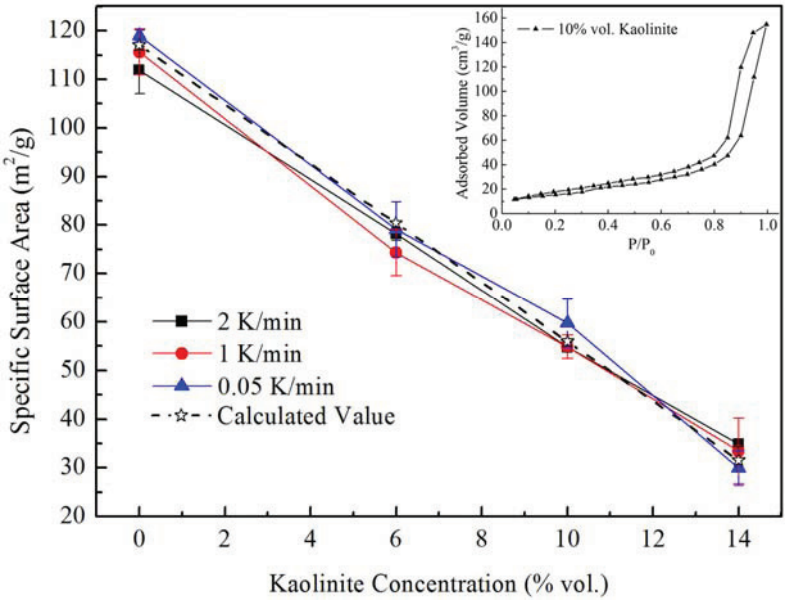

Fig. 3-6. BET specific surface area results for different freezing rates and kaolinite concentrations. The insert shows the adsorption and desorption curves for a 10 vol% kaolinite sample frozen at 2.0°C/min. The error bars indicate the range of the measured values.

Compared to the kaolinite concentration, the freezing rate has little effect on the specific surface area. This again indicates that the specific surface area of the composite is determined by the specific surface areas of the silica nanoparticles and kaolinite platelets and their relative concentration in the composite.

Fig. 3-7 shows the cumulative pore volume vs. pore radius plots for the different samples. Since the nitrogen adsorption measurement primarily detects nano-sized pores, Fig. 3-7 only shows the pores in the 3 nm to 600 nm range, most of which cannot be seen in the SEM images. All curves show a sharp increase in pore volume between roughly 30 and 100 nm, followed by a much more gradual increase above 100 nm. Pores in the 30 nm to 100 nm size result from the

aggregated silica nanoparticles. As a result, the volume of small pores decreases as the silica nanoparticles concentration decreases (increasing kaolinite concentration).

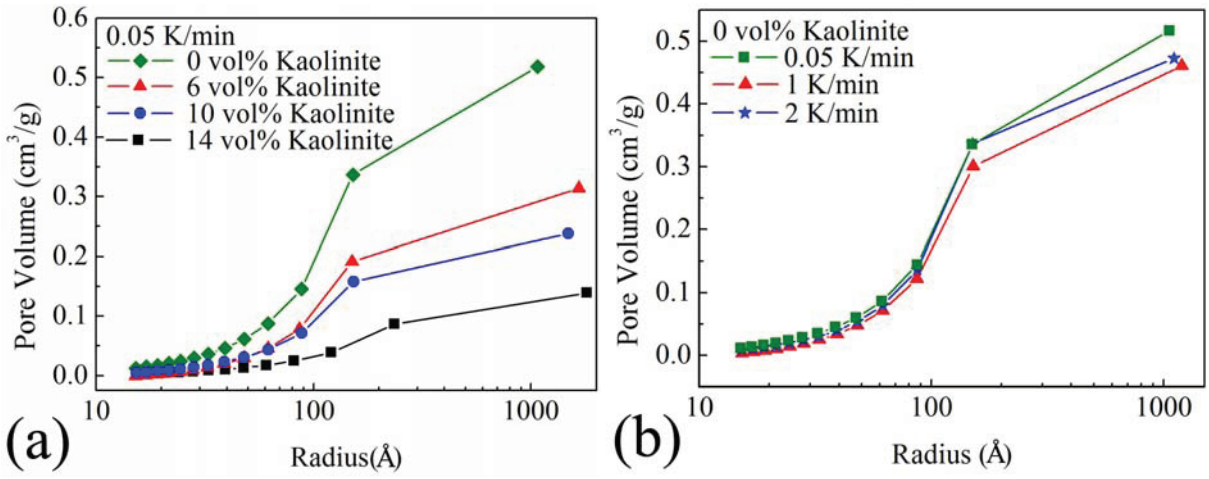

Fig. 3-7. Cumulative pore volume vs. pore radius plots for different (a) kaolinite concentrations frozen at 0.05°C/min, (b) freezing rates.

3.2.3 Equibiaxial Flexural Strength

The results of the equibiaxial flexural strength test are shown in Fig. 8. Poisson's ratios for the silica and kaolinite were assumed to be 0.17 and 0.45 (taken from Lobo-Guerreo[147]), respectively. Poisson's ratios for kaolinite-silica porous composites, ν_p, were obtained using the following equation of Arnold *et al.*[148]

$$\nu_p = 0.5 - \left(1 - P^{2/3}\right)^{1.21} \Big/ 4\left[(1-s)\frac{(3-5P)(1-P)}{2(3-5P)(1-2\nu_0)+3P(1+\nu_0)} + s\frac{(1-P)}{3(1-\nu_0)}\right] \quad (3\text{-}3)$$

where $s = \frac{1}{1+e^{-100(P-0.4)}}$, P is the porosity, υ_0 is Poisson's ratio for porous-free composite, which was obtained by linear interpolation based upon composition. The calculated Poisson's ratio for each porous composite is shown in Table 3-3.

Table 3-3. Calculated Poisson's ratios for the various porous composites.

Kaolinite Concentration	0 vol%	6 vol%	10 vol%	14 vol%	16 vol%	18 vol%
Poisson's Ratio	0.22	0.25	0.28	0.30	0.31	0.32

At 2.0°C/min freezing rate, as the kaolinite concentration increased from 0 vol% to 14 vol%, the flexural strength increased from ~0.05 MPa to 0.35 MPa. Decreasing the freezing rate to 0.05°C/min slightly increases the flexural strength, however the impact is not significant. Since the total solid concentration is kept at 18 vol% for all the samples, the strength increase is attributed to the kaolinite concentration increase. As discussed above, the kaolinite particles form the framework of the porous composites and apparently are capable of withstanding more load than the aggregated silica nanoparticles.

As a simple comparison, a strength test was also performed on composites made with very low nanoparticle concentrations (16 vol% kaolinite plus 2 vol% silica and 18 vol% kaolinite plus 0 vol% silica). Because these samples did not gel, the samples were obtained by freeze-casting immediately after mixing. As seen in Fig. 3-8, the flexural strength of the pure kaolinite sample was found to be approximately the same as that of the pure silica (roughly 0.04 MPa), while the strength of the 16 vol% kaolinite sample was intermediate between the strength of the 14 vol% and 18 vol% kaolinite samples.

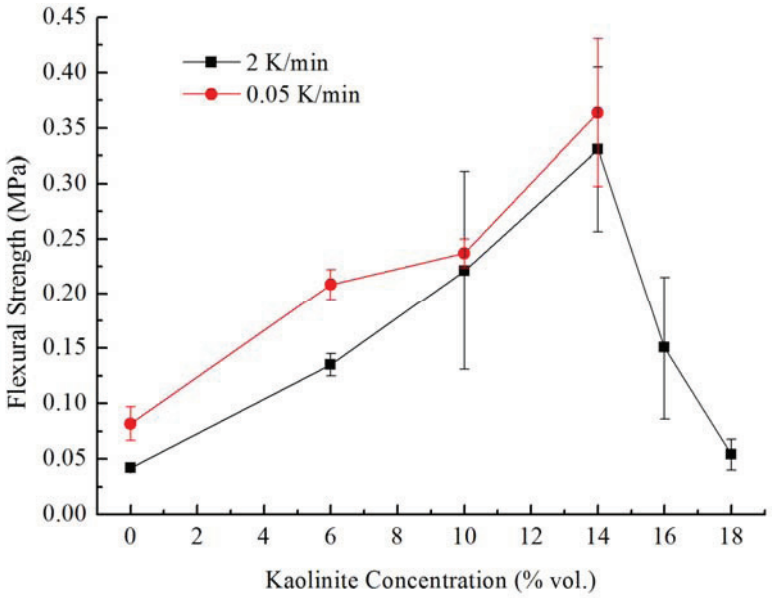

Fig. 3-8. Equibiaxial flexural strength of freeze-cast composites measured at 2.0°C/min and 0.05°C/min freezing rates. The error bars indicate the standard deviation of the measured values.

The results in Fig. 3-8 suggest that the maximum strength is obtained with a kaolinite concentration of approximately 14 vol% (4 vol% silica) and the strength at this concentration is six to seven times greater than that of either pure silica or pure kaolinite. It is thus clear that the two materials interact cooperatively in providing strength to the composite. The explanation to the strength improvement is elaborated in the mechanism section.

3.2.4 Proposed Mechanism

Electrophoresis measurements, performed with a Zetasizer Nano ZS, indicate that the silica nanoparticles are negatively charged with a zeta potential of -43 mV in a solution at pH 7. Thus without added electrolyte, the nanoparticles remain dispersed in solution by the mutual electrostatic repulsive forces. Upon additional of sufficient electrolyte, the Debye length characterizing the range of this repulsion is lowered enough that short-range van der Waals attractive forces becomes significant between the nanoparticles, causing them to aggregate into a space-filling network comprising the gel.

Although the chemistry at the faces of the kaolinite platelets is expected to be different from that of the edges, electrophoresis measurements yield a zeta potential of -25.2 mV in a solution at pH 4, meaning that the average charge on the platelets is negative. SEM images of the dry clay indicate that while individual platelets can be found, stacks consisting of as many as 50 platelets bound together are prevalent (see Fig. 3-9). Attempts to break these stacks using a high-shear mixer, as well as exposure to supercritical CO_2 followed by rapid depressurization, were unsuccessful, meaning that the stacks are held together strongly.

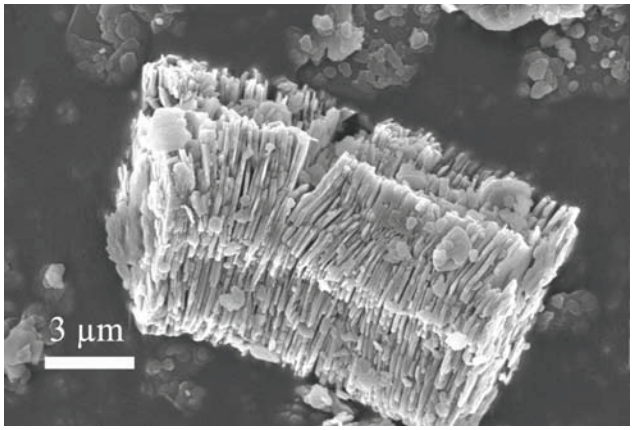

Fig. 3-9. SEM image showing a stack of kaolinite platelets. The material here had been washed with pure water but had no added salt or silica.

In order to better understand the nature of the silica/kaolinite interactions in these systems, a series of simple adsorption experiments were conducted. Silica suspensions were first mixed with distilled water, followed by addition of kaolinite and NaCl solution (if needed). The amounts of all additives were controlled to obtain suspensions with 1 wt% kaolinite and 1 wt% silica. Suspensions with and without NaCl were made for comparison. The suspensions were stirred for 1 hr to allow the nanoparticles and platelets to interact sufficiently. Next, the suspensions were allowed to rest for 30 min, during which a significant fraction of the platelets settled. After sedimentation, the supernatant was removed and the sedimented particles were gently washed three times to eliminate any nonadsorbed nanoparticles while not disturbing any that had adsorbed. The samples with no added salt were washed with pure water, while samples obtained with added NaCl were washed with water at the same NaCl concentration (0.5 M). The sediments were collected to exam the microstructure under SEM.

SEM images of the recovered platelets are shown in Fig. 3-10. As seen in Fig. 3-10a, significant adsorption occurs in suspension containing 0.5 M NaCl, indicating that NaCl screens the repulsion between the nanoparticles and platelets, allowing the nanoparticles to adsorb to the kaolinite surface. In contrast, in samples prepared with solutions containing no added NaCl (Fig. 3-10b), very few adsorbed nanoparticles were observed.

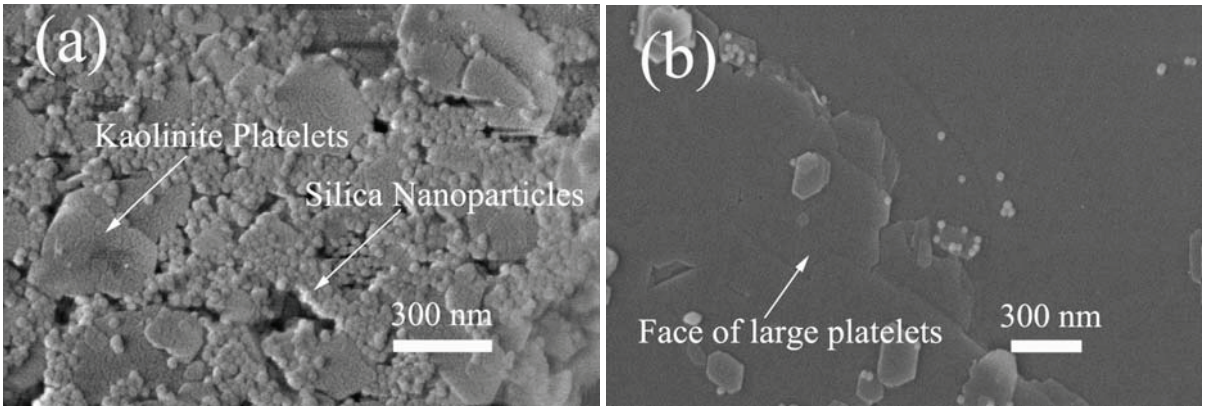

Fig. 3-10. SEM images of sedimented kaolinite plates after adsorption tests. The solution used in (a) contained 0.5 M NaCl, while the solution used in (b) contained no added salt. (The whole background of Fig. 10b is part of a large kaolinite platelet face.)

These results indicate clearly that the significant increases in strength of the freeze-cast composites produced by the addition of kaolinite arises from the ability of the kaolinite plates to bond together relatively large portions of the nanoparticles network and increase the strength of the network structure (see Fig. 3-11 below). Support for this hypothesis was provided by shear rheology measurements made by Baird and Walz,[149] who found that the strength of the gel, as characterized by the elastic modulus, was increased substantially by the addition of kaolinite.

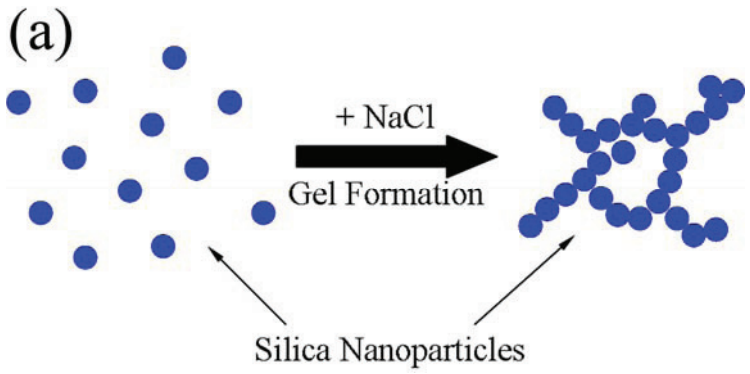

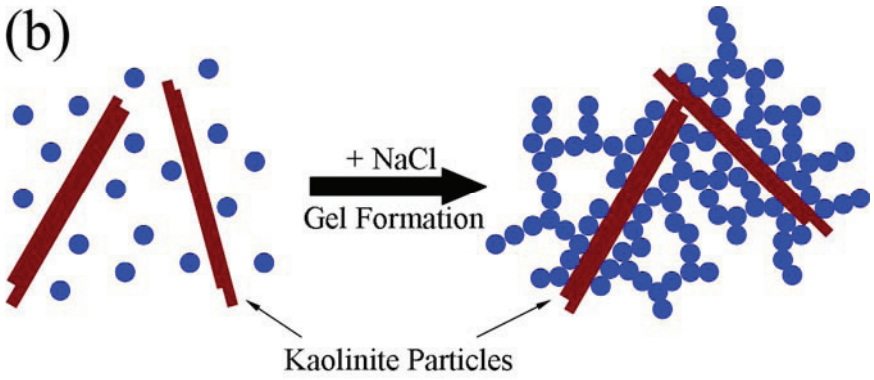

Fig. 3-11. Proposed gelation mechanism. (a) without kaolinite, the nanoparticles aggregate into a porous network upon the addition of salt, (b) when kaolinite plates are added, the platelets are bound together by nanoparticles to form network, adding strength to the structure.

Upon freeze-casting the gels, the growing ice-crystals will obviously disrupt this network, and a porous structure is formed. Nonetheless, the increased strength of the composite produced by the kaolinite-silica particle interaction clearly still persists. Based upon the nitrogen adsorption measurement, the specific surface area of particles is conserved during freeze casting, indicating that the sphere-like nanoparticles interact with each other by point contact. When load is applied to the sample, the point-to-point contacts from the nanoparticles are not able to transfer the load effectively, thus the strength of pure silica sample is low. When kaolinite particles are introduced to the system, the platelets are bonded together by nanoparticles throughout the network. Apparently, the stiffness of kaolinite stacks is higher than that of silica nanoparticle packing. In addition, as numerous nanoparticles attach to the stacks, the contacts between particles are largely improved and the load can be transferred much more efficiently. Therefore, strength reinforcement occurs with the addition of kaolinite. At around 14 vol% kaolinite content, the amount of silica nanoparticles reaches its critical value at which the network can be fabricated and kaolinite platelets can be effectively bonded (for gel formation, it is also around the critical value at which gel transition occurs), the maximum strength is obtained at this point. If the kaolinite concentration is further increased, the amount of silica nanoparticles is not high enough to form the bonded network. The shear strength of the platelets decreases rapidly and the transfer of load is less effective between stacks. As a result, the strength of the entire sample decreases.

3.3 Conclusions

The effect of kaolinite concentration and freezing rate on the structure, strength and surface area of freeze-cast composites of kaolinite and silica nanoparticles were investigated. The primary findings were:

1. Increasing the kaolinite concentration creates large and more interconnected pores in the interior (cross-section) of the samples. Changing the freezing rate from 2.0°C/min to 0.05°C/min does not have a significant impact on pore shape or structure.
2. On the outer surface of the composite samples, adding kaolinite creates much smaller and less numerous pores. In addition, the pores become thinner and more elongated. This trend appears significantly more pronounced in samples frozen at the higher freezing rate (2.0°C/min).
3. The specific surface area (area/mass) of the samples can be accurately predicted using the area and mass of the silica nanoparticles and kaolinite platelets assuming conversation of area (i.e., there is no significant area loss during freeze-casting). Freezing rate does not alter this property.
4. Adding kaolinite increases substantially the equibiaxial flexural strength of the composites. This occurs even when the total solids content (kaolinite plus silica volume concentration) is held fixed. The maximum strength in these studies occurred with a sample containing 14 vol% kaolinite and 4 vol% silica. The strength of this composite was six to seven times greater than that of a freeze-cast sample made with either silica only or kaolinite only. Samples frozen at 0.05°C/min had a slightly higher strength than those frozen at 2.0°C/min.
5. Adsorption tests show that significant adsorption of the nanoparticles to the kaolinite occurs during the formation of these materials. This adhesion is the likely cause of the increased strength, as the regions of the nanoparticle network are able to bind together kaolinite platelets.

CHAPTER 4. SINTERING BEHAVIOR OF THE KAOLINITE-SILICA NANOCOMPOSITES*

Abstract

In Chapter 3, the effects of added kaolinite on the microstructure and strength of freeze-cast composites of kaolinite platelets and silica nanoparticles were reported. This current chapter details the results of an investigation into the effects of the kaolinite on the microstructure and phase transformation of these materials during sintering. It is found that upon sintering at 1000°C, grain growth and phase transformation of the silica nanoparticles in the silica/kaolinite composites are hindered, and even completely inhibited, at sufficient concentrations of added kaolinite. Nonetheless, reduction in the size of the nanoparticles suggests that diffusion from silica nanoparticles to kaolinite platelets is occurring. Upon increasing the sintering temperature to 1250°C, boundaries between the two species completely disappear and new peaks are observed in the X-ray diffraction pattern of the composite that are not present in the patterns of either silica-only or kaolinite-only samples. These findings indicate that a transitioning interfacial phase forms at higher temperatures.

4.1 Experimental procedure

4.1.1 Materials and sample preparation

Details of the materials used and the sample preparation procedure were described in Chapter 3. In this chapter, aqueous samples containing kaolinite concentrations of 0, 1, 3, 4, 6, 10 or 18 vol% were prepared. 34 wt% silica nanoparticle suspension (Ludox TMA, Sigma Aldrich, St. Louis, MI) and kaolinite (Hydrite Flat-D, Imerys Performance Materials, Dry Branch, GA) powder serve as silica and kaolinite sources. As before, the total solids concentration (silica nanoparticles plus kaolinite) was fixed at 18 vol% in each sample, meaning that as the kaolinite content increased, the silica content decreased by an equal amount. All samples also contained 0.5 M NaCl to induce gelation in the aqueous dispersion.

* Chapter 4 was published in *Journal of the American Ceramic Society 2012, **95**(3), 883-891*[150]

All the samples, except for the 18 vol% kaolinite, were held for 4 h after being poured into silicone rubber molds (31 mm diameter, 2 mm deep, sample volume of approximately 1.5 cm^3) to allow gelation. Freeze-casting was then performed by an Advantage Freeze Dryer (SP Industries VirTis, Gardiner, NY). The samples were first cooled to -35°C with a freezing rate of 2.0°C/min, and then held at a temperature of -35°C and pressure of ~1.34 Pa for 400 min to sublimate the ice. Because the sample containing 18 vol% kaolinite (0 vol% silica) would not gel during the 4 h waiting period, freeze-casting was performed immediately after the sample was poured into the silicone mold to minimize sedimentation of the kaolinite platelets.

After freeze-casting, the samples were sintered at 1000°C, 1200°C, or 1250°C for 1 h with fixed heating and cooling rates of 5°C/min.

4.1.2 Characterization

The microstructures of the freeze-cast samples were observed using a field emission scanning electron microscope (SEM, LEO1550, Carl Zeiss MicroImaging Inc., Thornwood, NY). The sintered samples were coated with a 3-5 nm Au-Pt layer before examination (the coating thickness varies according to different composition; the thickness is kept at 5 nm for the silica nanoparticle size measurement.) Images of the cross-sections of the composite samples were obtained (the cross-sections were obtained by breaking the samples by hand and imaging one of the exposed surfaces). The phase analysis was carried out by X'Pert PRO diffractometer (PANalytical B.V., EA Almelo, The Netherlands). Thermogravimetric analysis (TGA) and differential scanning calorimetry (DSC) were carried out to understand weight loss and phase transformation during sintering by a simultaneous thermal analyzer (STA, 449 C Jupiter, Netzsch Instruments N.A. LLC., Burlington, MA). Infrared spectra were obtained to identify surface functional groups at different stages of sintering by analyzing chemical bond vibrations (IR, Excalibur HE Series FTS 3100, Agilent Technologies, Santa Clara, CA).

4.2 Results and discussion

4.2.1 Effects of kaolinite on microstructure of sintered composite

Shown in Fig. 4-1 are SEM micrographs displaying how the silica nanoparticles and kaolinite platelets transform upon sintering at 1000ºC for 1 h. Micrographs of samples containing

0 vol% kaolinite (silica only), 18 vol% kaolinite (kaolinite only), and 10 vol% kaolinite (8 vol% silica) are shown and labeled as a, b, and c, respectively. For each sample, micrographs taken before and after sintering are presented. A low magnification micrograph that shows the porous microstructure of the 10 vol% green kaolinite composite is given in the insert image of Fig. 4-1c. The fabricated green samples possess porosities around 82% with pore size ranging from ~30 μm to ~100 μm. The pores uniformly distribute throughout the sample with pore walls comprised of homogeneously packed silica and kaolinite particles. The rest of the micrographs in Fig. 4-1 were taken from the cross-section of pore walls. Microstructure observation has been carried out throughout the samples, and the given micrographs are representative of the entire samples. Upon sintering, the samples maintain higher than ~60% porosities with elongated pores.

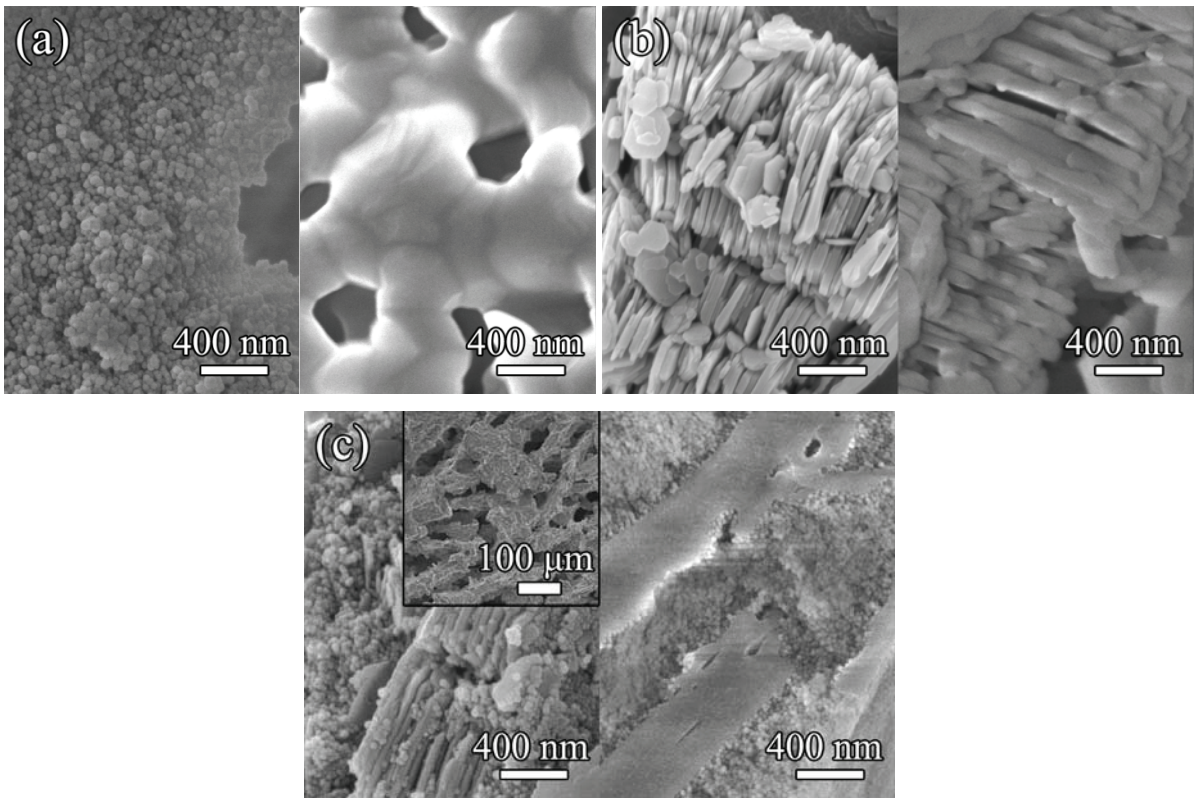

Fig. 4-1. Microstructures of: (a) pure silica sample, (b) pure kaolinite sample, and (c) 10 vol% kaolinite-silica nanocomposite. In all cases, the left side image shows the microstructure before sintering and the right side shows the microstructure after sintering at 1000°C. The insert in (c) is a low magnification micrograph shows the porous microstructure of the 10 vol% kaolinite-silica nanocomposite before sintering.

For the silica-only sample (Fig. 4-1a), the 22 nm nanoparticles grow into ~400 nm size grains upon sintering. The nano-sized pores found prior to sintering, which are formed by simple packing of the nanoparticles, evolve into much larger ones with sizes ranging from hundreds of nanometers to micrometers, with a significant loss of surface area and neck formation between grains. Individual silica nanoparticles can no longer be identified after sintering. Diffusion of the silica is primarily from the particle/grain surfaces to the necks, and leads to grain growth instead of densification.[125]

For the pure kaolinite sample (Fig. 4-1b), the boundaries between kaolinite platelets become less distinct after sintering and the sharp edges and corners become rounded. Based on the boundary and morphology differences between the platelets before and after sintering, it is speculated that some sintering diffusion and inter-platelet bonding occur.

For the 10 vol% kaolinite sample, the grain growth of the silica nanoparticles does *not* occur and the nano-sized silica particles are conserved. In fact, the size of the silica actually decreases as determined from the SEM images (discussed in greater detail in section 4.2.3 below). For the kaolinite platelets, however, sintering proceeds as with the kaolinite-only sample, with the platelets again becoming rounded and the platelet boundaries less distinct. Compared to the green composite, the interfaces of silica nanoparticles and kaolinite platelets in the sintered sample are not as distinct. The sintered morphology suggests that diffusion occurs between kaolinite particles and silica nanoparticles.

To further explore this hindering effect of the kaolinite, a composite was made containing only 1 vol% kaolinite (17 vol% silica). As shown in Fig. 4-2a, silica nanoparticles located relatively far from kaolinite platelets were observed to grow into larger size grains during the sintering process (1000°C), similar to that seen in the silica-only samples. By comparison, silica nanoparticles located in close proximity to the kaolinite platelets preserve their size (or even show a decrease in size) and shape upon sintering (Fig. 2b). (It should be noticed that excessive silica contents have been removed in order to observe the nanoparticles attached to the kaolinite platelets.) This observation suggests that the hindrance effect of the silica is of finite range. While determination of the specific value of this range requires further investigation, it is interesting to first look in more detail at the variation in sintering behavior with kaolinite concentration.

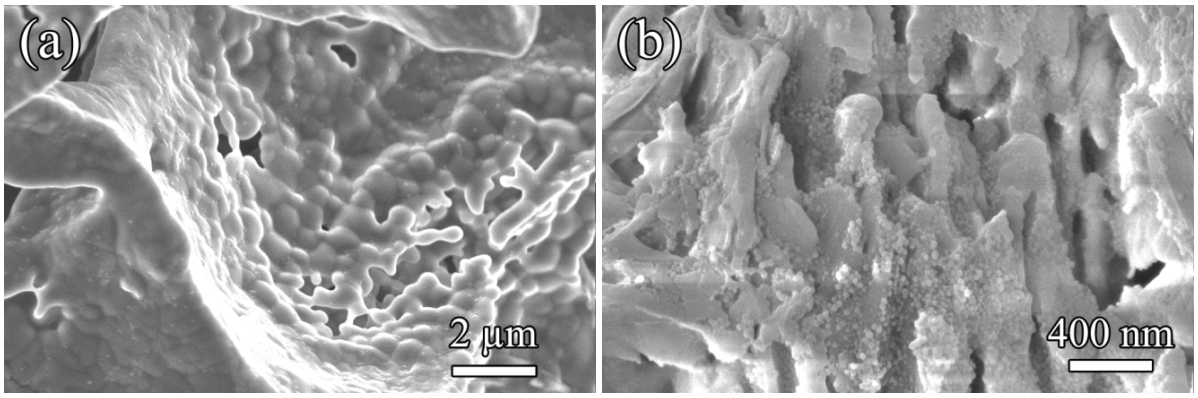

Fig. 4-2. Microstructure of 1 vol% kaolinite-silica nanocomposite after sintering at 1000°C: (a) silica grains far from kaolinite particles, (b) silica nanoparticles attached to kaolinite particles.

Shown in Fig. 4-3 are SEM micrographs obtained on sintered samples containing 3, 4, and 6 vol% kaolinite (again, the total concentration of kaolinite and silica was fixed at 18 vol%). As discussed above, sintering of the silica nanoparticles is observed to occur throughout the entire sample (except for the regions very close to kaolinite platelets) in the 1 vol% kaolinite sample (Fig. 4-2(a)). For the 3 vol% kaolinite sample (Fig. 4-3(a)), necks between silica nanoparticles form and silica grain size increases from ~22 nm to ~50 nm, even though the grain size is much smaller than that of the 1 vol% kaolinite sample. Thus while the majority of the silica nanoparticles experience sintering-related diffusion and grain growth, the hindrance effect from the kaolinite platelets is obvious. Upon increasing the kaolinite content to 4 vol% (Fig. 3(b)), sintering is observed to occur in only a small portion of the sample. The grains remain around the initial size (~22 nm). Finally, in the 6 vol% kaolinite sample (Fig. 4-3(c)), silica nanoparticles are almost fully conserved after sintering throughout the sample and very little grain growth is observed. The nanoparticle size actually decreases during sintering which is discussed in section 4.2.3. This would suggest that at the sintering conditions used here (1000°C for 1 h), the sintering of the silica nanoparticles is almost totally inhibited at kaolinite concentrations of roughly 4 vol% and above.

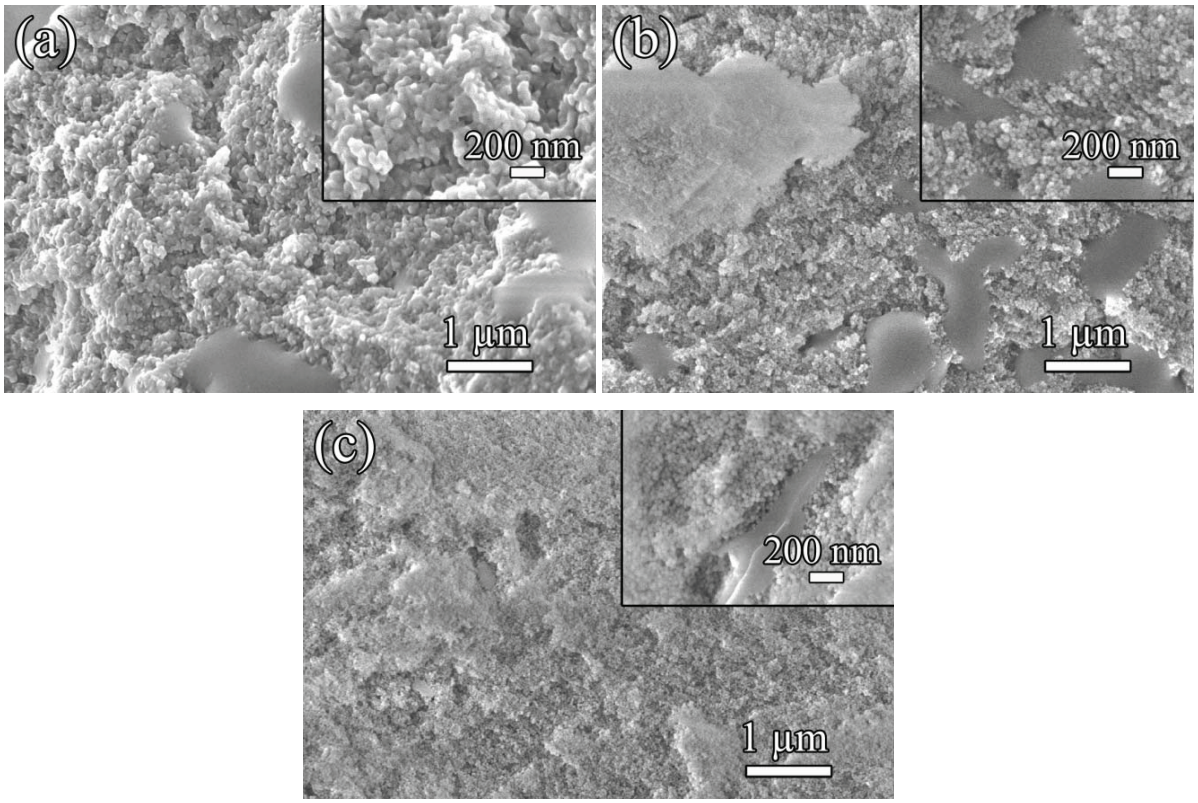

Fig. 4-3. Microstructures of 1000°C sintered kaolinite-silica nanocomposites: (a) 3 vol% kaolinite, (b) 4 vol% kaolinite, and (c) 6 vol% kaolinite. The total solids concentration (silica nanoparticles plus kaolinite) is 18 vol% in each sample.

This hindrance effect of kaolinite on the sintering behavior of silica nanoparticles was found to be temperature limited and disappeared upon increasing the temperature further. Fig. 4-4 displays the microstructure of the samples sintered at 1250°C. Compared to the samples sintered at 1000°C, both the grains and pores of pure silica sample grow even larger (Fig. 4-4(a)). The pores evolve to irregular and elongated shapes. In both the pure kaolinite sample (Fig. 4-4(b)) and the 10 vol% kaolinite sample (Fig. 4-4(c)), individual kaolinite platelets can no longer be observed, indicating that kaolinite-kaolinite and/or kaolinite-silica diffusion is promoted at elevated temperatures. The lack of discernible boundaries between the silica and kaolinite components suggests that the two species interact at the interface.

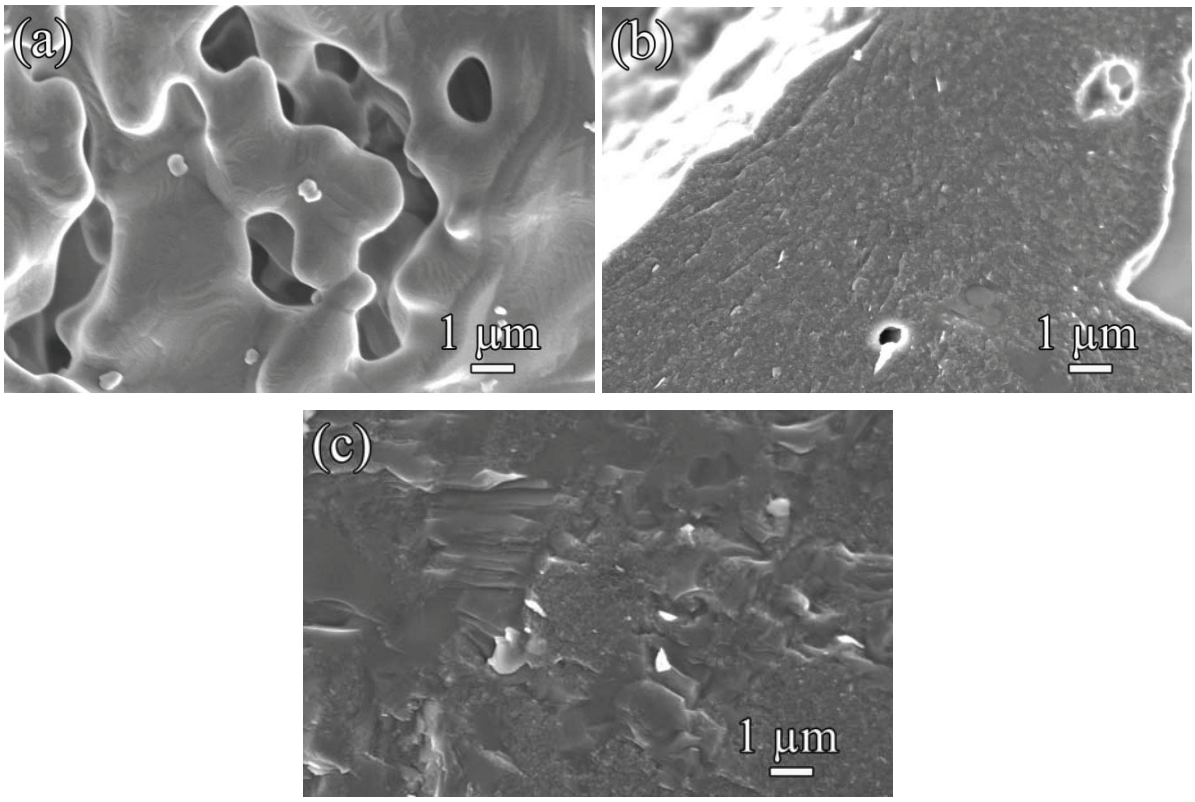

Fig. 4-4. Microstructures of: (a) pure silica sample, (b) pure kaolinite sample, and (c) 10 vol% kaolinite-silica nanocomposite sintered at 1250°C for 1 h.

4.2.2 Analysis of sintering process

4.2.2.1 X-ray diffraction

Fig. 4-5 shows the X-ray diffraction patterns for silica-only, silica-kaolinite composites, and kaolinite-only samples before and after sintering at 1000°C for 1 h. Different from the equilibrium phase transition sequence for pure silica (α-quartz to β-quartz at 574.3°C, then to tridymite at 867°C, and finally to β-cristobalite at 1470°C), only one phase transformation is identified within the studied range for this silica nanoparticle system. Before sintering, the silica in the nanoparticles is amorphous (Fig. 4-5(a)). The sharp peaks in the XRD pattern correspond to those of NaCl crystals, which was introduced to the suspension to induce gel formation before freeze casting. After sintering, the silica transforms to α-cristobalite phase (tetragonal structure) (Fig. 4-5b). NaCl is removed from the system and the corresponding peaks disappear.

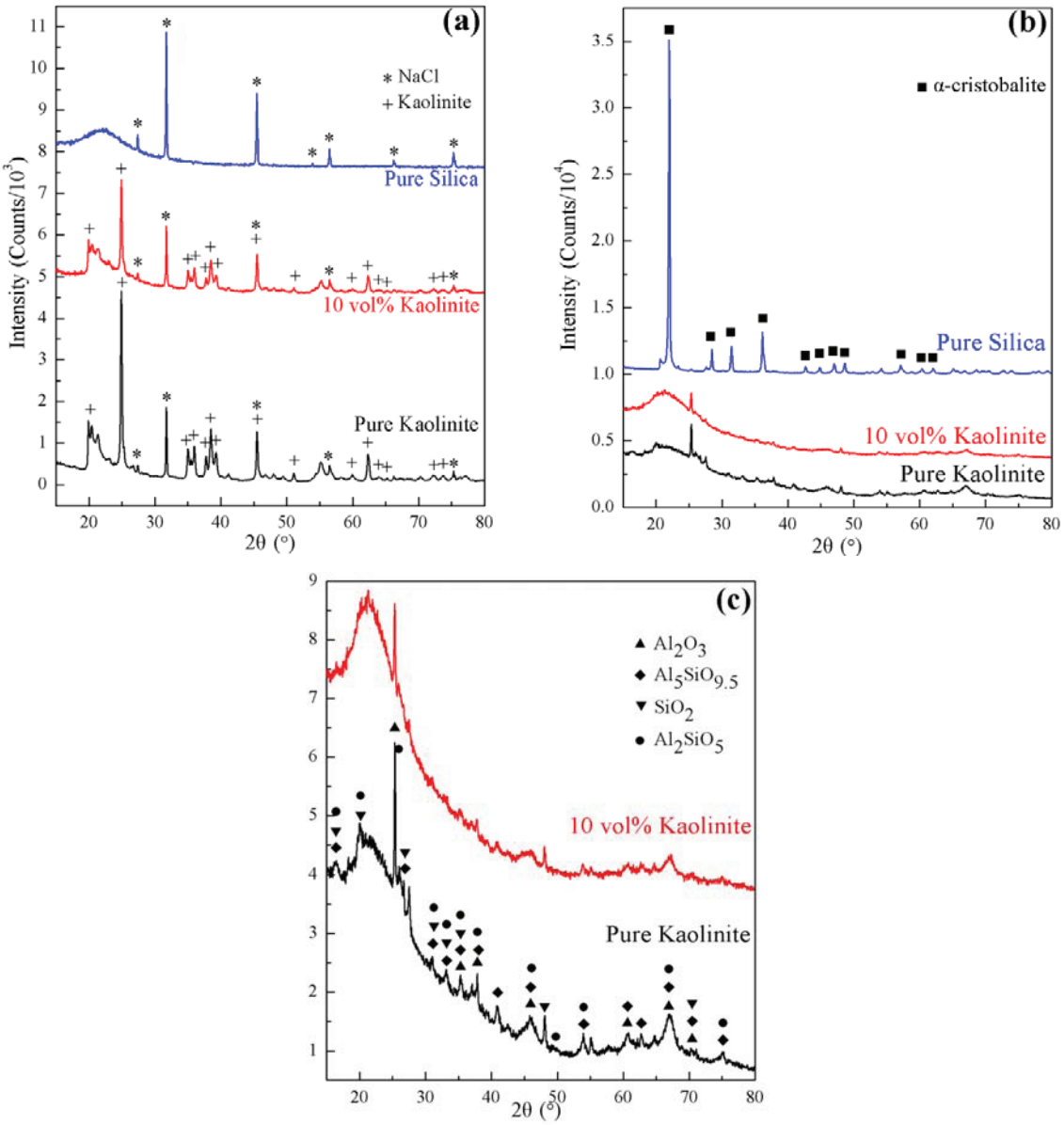

Fig. 4-5. XRD patterns for pure silica, kaolinite-silica composite, and pure kaolinite samples: (a) green state, (b) sintered state (1000°C for 1 h), (c) a closer view of kaolinite-silica composite and pure kaolinite patterns sintered at 1000°C for 1 h. The curves have been offset vertically for ease of viewing.

In contrast, the kaolinite sample before sintering shows a monoclinic phase with a chemical formula of $Al_2Si_2O_5(OH)_4$ (Fig. 4-5a). After sintering, phase transformation occurs and the aluminum silicate hydroxide transforms to a mixture of different phases: pseudo-mullite ($Al_5SiO_{9.5}$), sillimanite (Al_2SiO_5), aluminum oxide (Al_2O_3), and silicon dioxide (SiO_2) (Fig. 4-

5(b)). Since the patterns for the sintered kaolinite and composite samples are complicated and consist of several different phases, a revised analysis method was used here to determine the phases. The three strongest peaks of the possible phases suggested by the software (X'Pert HighScore Plus) are compared to those of the sample patterns. Phases are accepted if the variation of d-spacing is less than 0.005 nm. Then the possible phases are ranked according to the variation of d-spacing. There are only a few weak peaks for the sintered kaolinite sample, suggesting that the system is still in the process of phase transformation and the crystalline phases are not fully developed yet.

The XRD patterns for the kaolinite-silica composite before and after sintering agree with those of pure kaolinite samples, indicating that silica nanoparticles in both cases remain amorphous. In the green samples, the peak intensities from the sample containing 10 vol% kaolinite are lower than those in the pure kaolinite material. This suggests that the presence of the amorphous silica is lowering the peak intensities. This same trend is also observed upon comparing the patterns of the pure kaolinite and 10 vol% kaolinite samples after sintering, further indicating that the silica remains amorphous after sintering. It is also possible that a new amorphous phase is formed during this sintering, however I currently have no direct evidence of this.

4.2.2.2 Thermal analysis

To fully understand the phase transformation involved in each sample during sintering, the weight loss and thermal change are examined. The weight loss of the pure silica sample occurs in three temperature ranges (Fig. 4-6(a)). The first one is a sharp loss that occurs below 100°C, which is caused by the sublimation of adsorbed water. The second one happens gradually from 100°C to 850°C, the reason of which is elaborated in the IR analysis. The third one is again a drastic loss from 850ºC to 1000ºC. This only occurs during/after the silica phase transformation (amorphous to α-cristobalite) from 800°C to 850°C, where an exothermic peak is observed on the DSC curve (Fig. 4-6(b)). This third weight loss does not occur in the composite where the silica phase transformation around 800°C is inhibited.

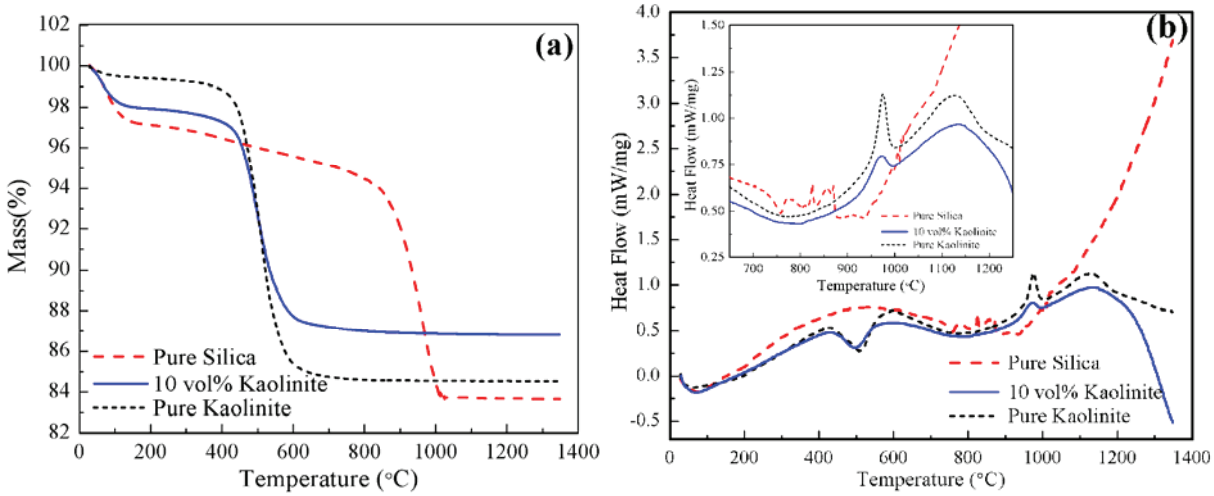

Fig. 4-6. (a) TGA curves and (b) DSC curves for pure silica, 10 vol% kaolinite composite, and pure kaolinite samples. The inset graph provides the details of the plots from 650°C to 1250°C.

For the kaolinite sample, a significant weight loss occurs from 450°C to 550°C (Fig. 4-6(a)), which corresponds to an endothermic dehydroxylation/dehydration process on the DSC curve.[17] The phase transformation for the kaolinite sample happens around 980°C (Fig. 4-6(b)), shown as an exothermic peak on the DSC curve. The DSC curve of the composite shows the hindrance effect of kaolinite platelets on silica crystallization. The exothermic peaks at 800-850°C on the DSC curve and the third weight loss on the TGA curve seen in the silica sample are not observed on the curves for the composite. More precisely, the TGA and DSC for the composite are qualitatively similar to those of the pure kaolinite sample.

Based on the measured TGA curves for the pure silica and pure kaolinite samples, the theoretical weight loss for the 10 vol% kaolinite composite should be 15.9% by linear interpolation. The difference between the measured (13.2%) and the calculated values is attributed to the disappearance of the third weight loss process of the 8 vol% silica content. This suggests that the third weight loss on the TGA curve for the pure silica sample is associated with the amorphous to α-cristobalite phase transformation. Kaolinite prevents this phase transformation and consequently eliminates this weight loss for the kaolinite-silica composite. Above 1000°C, the weights of all the three samples remain almost constant.

Overall, for the pure silica sample, 2.5% weight loss is attributed to *adsorbed* water, 4% to the *absorbed* water (to be discussed next), and 9.9% to phase transformation (discussed in greater detail below). For the kaolinite sample, 1% weight loss is attributed to adsorbed water

and 14.5% to the dehydroxylation/dehydration process. For the 10 vol% kaolinite composite, 2.5% weight loss is attributed to adsorbed and absorbed water and 10.7% to the dehydroxylation/dehydration process.

With a further increase in temperature, a broad exothermic peak appears on the DSC curve of the pure kaolinite sample (peak at approximately 1100°C) and the composite sample. This peak suggests that the kaolinite undergoes an additional transformation at a temperature above 1000°C and that a similar transformation also occurs in the composite material. In this range, there is no peak on the silica DSC curve, which indicates that the tetragonal crystalline silica phase remains up to 1300°C.

4.2.2.3 Infrared spectroscopy

In order to understand the weight loss during the sintering process, infrared spectra for the samples thermally treated at 150°C, 400°C, 700°C, and 1000°C are shown in Fig. 4-7. The holding time at these temperatures is 1 h. After treatment at 150°C and 400°C, broad absorption bands appear at 3468 cm^{-1} and 1638 cm^{-1} wavenumbers for the pure silica sample, while intense absorption bands appear from 3700 cm^{-1} to 3620 cm^{-1} for the pure kaolinite sample. As an example, the specific wavenumbers for the 400°C treated sample are: 3698 cm^{-1}, 3671 cm^{-1}, 3651 cm^{-1}, and 3620 cm^{-1}. These wavenumbers correspond to the O-H stretching and bending vibrations. The O-H vibrations in water are distinguishable from those in free hydroxyl groups as hydrogen bonding in water reduces the vibration frequency and broadens the absorption bands. Therefore, the high intensity absorptions between 3700 cm^{-1} and 3600 cm^{-1} correspond to the O-H stretching vibration in hydroxyl groups, while the broad absorption bands from 3500 cm^{-1} to 3200 cm^{-1} correspond to the O-H stretching vibration in water. Similarly, the absorption peaks around 1200-600 cm^{-1} and at 1638 cm^{-1} are related to the O-H bending vibrations in hydroxyl groups and in water, respectively. This means adsorbed water stays in the pure silica samples up to 400°C, while the pure kaolinite sample only involves hydroxyl groups (lattice water), which are not removed until 400°C.

The tiny peaks at 3450 cm^{-1} and 1650 cm^{-1} wavenumbers for the kaolinite sample indicate that the O-H content as adsorbed water is very low. The O-H vibrations for the 10 vol% kaolinite-silica composite are the combination of those of the pure silica and kaolinite samples (Fig. 4-7(c)). Both intense peaks and broadened absorptions appear in the 150°C and 400°C

samples, indicating that the composite sample contains both adsorbed water and lattice O-H groups.

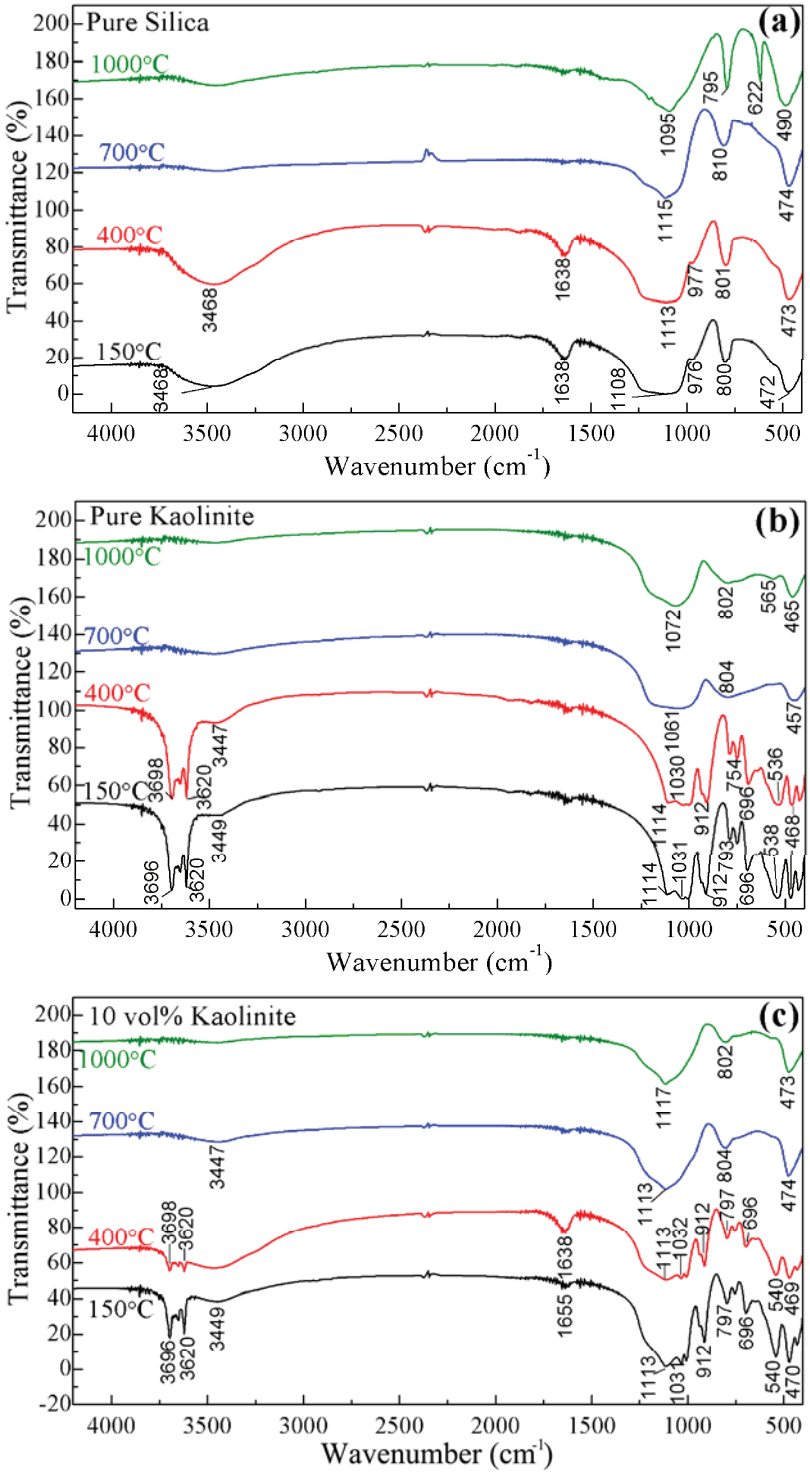

Fig. 4-7. IR spectra for samples treated at 150°C, 400°C, 700°C, and 1000°C: (a) pure silica, (b) pure kaolinite, (c) 10 vol% kaolinite composite.

The weight loss observed in Fig. 4-6(a) can be explained by the IR results. For the pure silica sample, the first weight loss is caused by the loss of free water. The second one is mainly the loss of adsorbed and lattice water molecules as O-H vibrations are not identified in the high temperature samples (700°C and 1000°C) (Fig. 4-7(a)). The third weight loss can only be hypothesized and may be related to the loss of oxygen during silica crystallization. As discussed above, the weight loss of kaolinite is a dehydroxylation/ dehydration process, which occurs from 450°C to 550°C.

The phase transformation of the pure silica sample around 850°C is further confirmed by the IR spectra. The absorption bands at 1108 cm^{-1}, 976 cm^{-1}, 800 cm^{-1}, and 472 cm^{-1} for the 150°C thermally treated sample indicate amorphous silica.[151] The appearance of a sharp absorption band after 1000°C sintering at 622 cm^{-1} wavenumber is attributed to the formation of tetragonal silica crystals (Fig. 4-7(a)).[152] Sintering of silica nanoparticles in the composites is inhibited as the 622 cm^{-1} sharp absorption band is absent (Fig. 4-7(c)).

The complex absorption bands for the pure kaolinite sample after 150ºC thermal treatment (1114 cm^{-1}, 1031 cm^{-1}, 912 cm^{-1}, 793 cm^{-1}, 696 cm^{-1}, 538 cm^{-1}, and 468 cm^{-1}) correspond to kaolinite.[151] The evolution in the fingerprint region (1450 to 600 cm^{-1}) for the kaolinite sample proves the continuous phase transition during sintering (from 150°C to 1000°C). The change between the 400°C and 700°C thermally treated kaolinite samples is a result of kaolinite dehydroxylation/dehydration from 450°C to 550°C. The fingerprint region bands (1450 to 600 cm^{-1}) of the 10 vol% kaolinite-silica composite at 150°C and 400°C are consistent with those of the pure kaolinite sample. This means that the kaolinite behavior is dominant in the system. At 700°C, the composite peaks become broad and similar to those of both the pure silica sample and the pure kaolinite sample, meaning that the phase transformation is a continuous process. At 1000°C, the composite shows the same peaks as at 700°C, while the peaks for the pure silica sample have changed to the tetragonal phase. This again indicates the hindrance effect of kaolinite on the sintering of pure silica nanoparticles in the composite.

4.2.3 Proposed mechanism

The results presented above demonstrate consistently the ability of the kaolinite to alter the sintering of the silica. After sintering at 1000°C, the kaolinite platelets in the samples containing either kaolinite-only or 10 vol% kaolinite are in the middle of phase transformation from amorphous silica plus monoclinic kaolinite to mullite ($3Al_2O_3 \cdot 2SiO_2$) plus crystalline silica. The XRD patterns of both samples after sintering appear identical, suggesting that the kaolinite phase transformation is not altered by the presence of the silica. By comparison, whereas sintering pure silica nanoparticles at 1000°C results in substantial changes in morphology and the transformation from an amorphous phase to crystalline α-cristobalite phase, no such changes in the silica are observed when sufficient amounts of kaolinite are added to the sample.

Nonetheless, as mentioned above, some changes in the silica nanoparticles are still observed, specifically in the nanoparticle size. This is illustrated more clearly in Fig. 4-8(a), which plots the measured nanoparticle diameter (obtained via SEM) versus kaolinite concentration upon sintering at 1000°C for 1 h. The nanoparticle diameters are measured from the SEM images, and the error bars in Fig. 8 are the standard deviation of 50 measurements. As can be clearly seen, increasing the kaolinite concentration from 6 to 14 vol% results in a steady decrease in the nanoparticle diameter. This would tend to suggest that even though no new additional phases are seen in the XRD pattern of composite samples sintered at 1000°C, diffusion from the silica nanoparticles to the kaolinite platelets is still occurring.

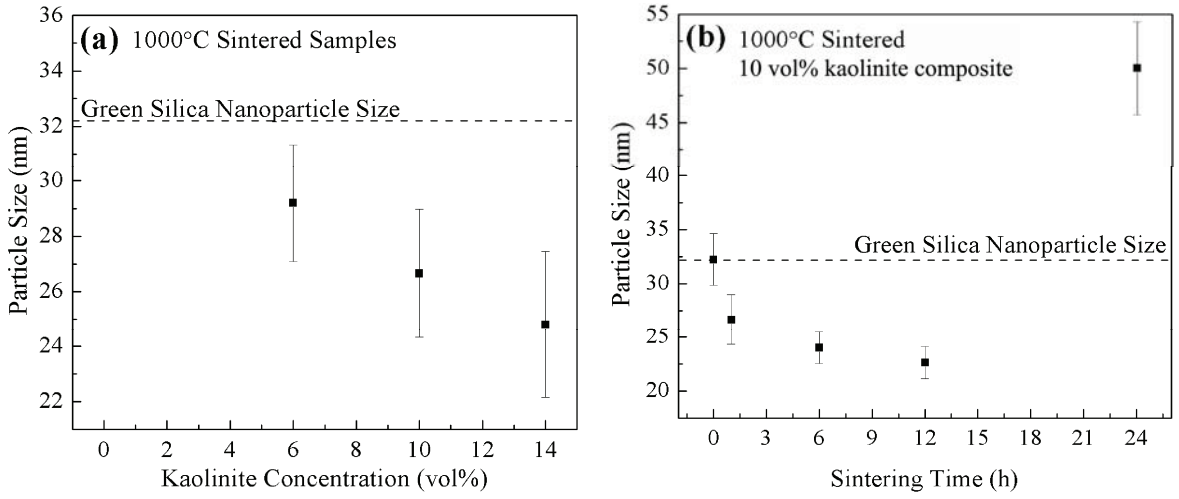

Fig. 4-8. Silica nanoparticle size evolution in the composite during sintering process as a function of: (a) kaolinite concentration, (b) sintering time. (Note that below approximately 4

vol% kaolinite, the silica particles sinter and individual nanoparticles cannot be discerned.) The error bars indicate the standard deviation of the measured values.

This diffusion from silica nanoparticles to kaolinite platelets can be seen further upon investigating the effect of sintering time on the silica nanoparticle size (Fig. 4-8(b)). When the sintering holding time increases up to 12 h, the silica nanoparticle size decreases correspondingly, from 32 nm to 22.6 nm. This finding suggests that the silica species diffuses to kaolinite particles throughout the sintering.

However, the diffusion between silica nanoparticles continues to occur and the results of this process can be observed if the holding time is long enough. As shown in Fig. 4-9(b), silica nanoparticles grow into much larger grains (50 nm) with a 24 h sintering time at 1000°C (shown in Fig. 4-8(b)). Although not tested, it is likely that additional growth in grain size would occur upon additional increases in sintering holding time.

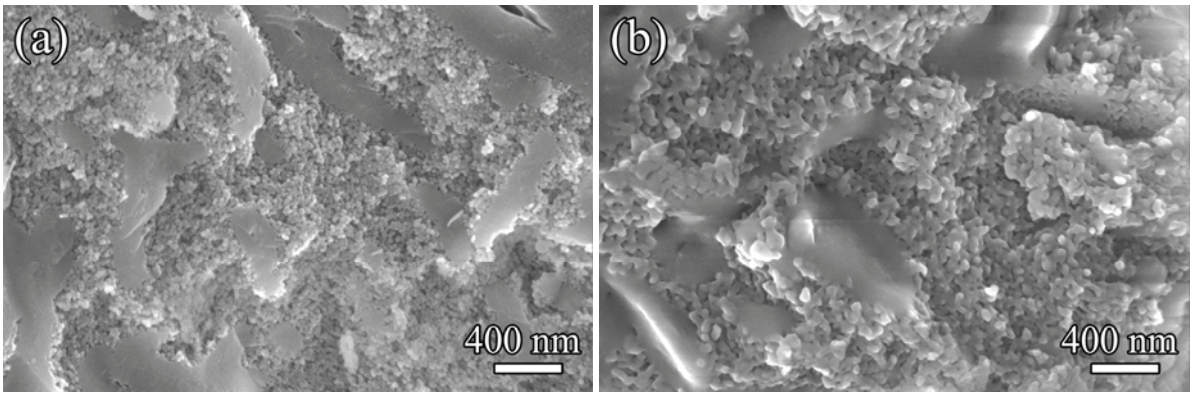

Fig. 4-9. Microstructures of 10 vol% composite sintered at 1000°C with holding time of: (a) 6 h, (b) 24 h

It should be explained that the dashed line in Fig. 4-8 is the average diameter of unsintered nanoparticles measured by SEM – approximately 32 nm. This is significantly larger than the manufacturer-reported diameter of 22 nm, and this difference is thought to be due to the 5 nm Au-Pt coating used to prepare the samples for SEM analysis. To confirm that this was the case, TEM images were obtained on silica nanoparticles both before and after applying the Au-Pt coating, and the observed difference in diameter was consistent with the 10 nm difference (5 nm

coating results in 10 nm increase in diameter) between the SEM and manufacturer-reported results.

The finding that the silica and kaolinite particles are interacting at 1000°C suggests that sintering at higher temperatures could possibly lead to interesting phase behavior. Thus XRD measurements were made on 10 vol% kaolinite samples that had been sintered at 1200°C and 1250°C for 1 h. The results are shown in Fig. 4-10. As can be seen, significant new structure (e.g. peak at 21.69°) develops with temperature increase, especially after sintering at 1250°C. The sharp peak around 21.99° is a signature peak for α-cristobalite. However, the XRD pattern of 1250°C sintered 10 vol% kaolinite composite cannot be formed by simply adding those of silica-only and kaolinite-only samples, indicating that new phases have developed at this sintering temperature.

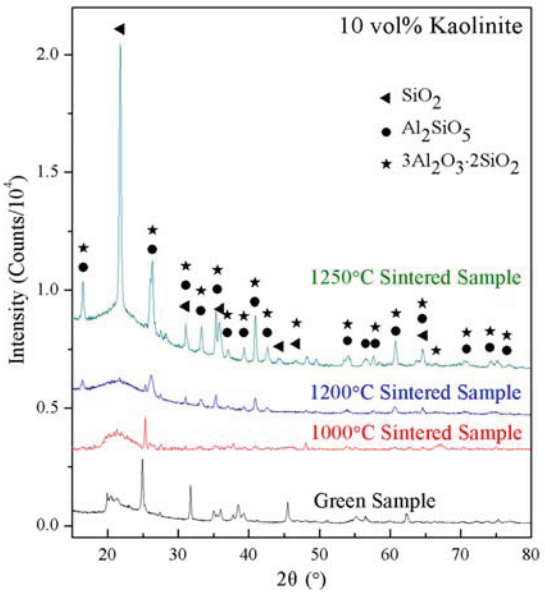

Fig. 4-10. XRD patterns for 10 vol% kaolinite-silica composite sintered at 1000°C, 1200°C, and 1250°C. The XRD pattern for a green sample is also shown for comparison.

Shown in Fig. 4-11 is a comparison of the XRD results for a pure kaolinite sample, a pure silica sample, a 6 vol% kaolinite sample, and a 10 vol% kaolinite sample, all of which were sintered at 1250°C. At this sintering temperature, the silica-only sample conserves the α-cristobalite crystalline structure, while the kaolinite-only sample evolves into a mixture of mullite, sillimanite, and hexagonal silica phases. Although the profile for the composite sample

shows many similarities with that of the pure kaolinite, there are also clear differences, suggesting that the silica and kaolinite species have now merged to form additional phases. First, the peak around 21.69° in the composite XRD profile is slightly different from the typical peak (21.99°) for α-cristobalite phase. In addition, many small peaks in the silica-only XRD profile are missing from that of the composite. These phenomena indicate that the new phases developed in the composite are different from the α-cristobalite phase formed by the silica-only sample although it displays a tetragonal crystalline structure. The 6 vol% kaolinite composite shows much lower peak intensities than either the silica-only sample or the 10 vol% kaolinite composite, suggesting that pure silica phase transformation is inhibited by kaolinite addition and the excessive silica in the composite is still in the middle of phase transformation. It is my hypothesis that the new features identified in the 1250°C sintered composite correspond to the interfacial species that bonds mullite/sillimanite and amorphous silica together. In this case, only the silica contents at the interface transform to pseudo-α-cristobalite phase.

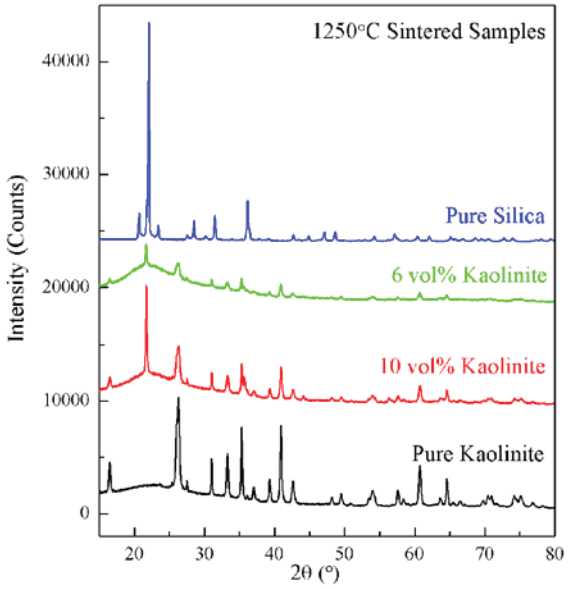

Fig. 4-11. XRD patterns for a pure silica sample, a pure kaolinite sample, a 6 vol%, and a 10 vol% kaolinite-silica composite, all of which are sintered at 1250°C. The indexing of the peaks is not shown as they are the same as in Fig. 4-5 and Fig. 4-10.

In summary, these results indicate that upon sintering at 1000°C, the transformation of the silica nanoparticles from an amorphous phase to α-cristobalite is hindered by the presence of

the kaolinite. Nonetheless, the reduction in size of the nanoparticles, especially as a function of the concentration of added kaolinite and time, indicates that the two species are clearly interacting, possibly through diffusion of material from the silica to the kaolinite.

Upon increasing the sintering temperature to 1250°C, additional peaks are found in the XRD pattern of the composite material that are not observed in the patterns of either pure silica or pure kaolinite samples sintered at identical conditions. This finding suggests that at this higher temperature, an additional interfacial phase with crystal structure close to α-cristobalite forms. Such formation of transitioning interfacial phase that bonds mullite/sillimanite and amorphous silica phase is consistent with the SEM images (Fig. 4-4) in which boundaries between the silica and kaolinite phases can no longer be discerned, and the DSC results (Fig. 4-6) in which the thermal response of the composite sample at these higher temperatures differs from that of either the pure silica or pure kaolinite samples. The material diffusion from silica nanoparticles to kaolinite particles and the formation of the interfacial species results in the improvement of mechanical strength, which will be elaborated in the following chapter.

4.3 Conclusions

Silica nanomaterial and kaolinite-silica nanocomposite were fabricated by sintering of the corresponding freeze-cast samples. Pure silica nanoparticles experience grain and pore growth when sintered at 1000°C, transforming from an amorphous structure into an α-cristobalite crystalline structure at approximately 850°C. In the presence of sufficient concentrations of kaolinite platelets (roughly 4 vol% kaolinite or higher), however, this phase transformation is almost completely inhibited. Nonetheless, significant reductions in the size of the nanoparticles after sintering suggest that diffusion between the nanoparticles and kaolinite platelets occurs.

Upon increasing the sintering temperature to 1250°C, boundaries between the two species can no longer be discerned in the SEM images. In addition, new features are observed in the XRD pattern of the composite material that cannot be seen in the patterns of the silica-only or kaolinite-only samples sintered at identical conditions. This suggests that an interfacial phase with pseudo-α-cristobalite crystalline structure has formed at this higher temperature and that the new interfacial phase bonds the mullite/sillimanite and amorphous silica phases.

CHAPTER 5. STRENGTHENING EFFECT OF KAOLINITE ON THE SILICA NANOPARTICLE-BASED COMPOSITES*

Abstract

This chapter examines the effects of kaolinite on the mechanical strength and porosity of freeze-cast kaolinite-silica composites. Measurement of the equibiaxial flexural strength shows that, after sintering at 1250°C for 1 h, a ceramic containing 10 vol% kaolinite and 8 vol% silica has a strength that is 52 times greater than a ceramic containing only 18 vol% silica and 2.5 times greater than one containing only 18 vol% kaolinite, yet while also being 69% porous (i.e. the porosity after sintering). It is proposed that this greater strength arises from three mechanisms. First, the kaolinite and silica particles bond together to form a connected network in which the much larger kaolinite platelets distribute the applied stress over a larger region of the sample (this increased strength is even seen in the freeze-cast green bodies prior to sintering). Second, X-ray diffraction measurements indicate that upon sintering at 1250°C, new phases are formed when both silica and kaolinite are present, which I postulate contribute greatly to the strength of the composite. Third, the pore walls in samples containing both kaolinite and silica are much more continuous and unbroken than in samples containing only kaolinite.

5.1 Experimental procedure

5.1.1 Materials and sample preparation

Ludox TMA colloidal silica suspension (34 wt%, Sigma Aldrich, St. Louis, MI), kaolinite powder (Hydrite Flat-D, Imerys Performance Materials, Dry Branch, GA), sodium chloride (NaCl, AR grade, Mallinckrodt, Paris, KY), sodium hydroxide (NaOH, Mallinckrodt, Paris, KY), and de-ionized water were used as received to prepare the samples. In this chapter, well-dispersed suspensions were firstly prepared by sequentially adding certain amounts of Ludox, de-ionized water, NaOH, and kaolinite into a processing vial. After mixing by a vortexer (Fisher Scientific Inc, Bohemia, NY), NaCl was introduced into the suspension to generate a sol-to-gel transition process, which was found to improve the interaction of two species and the

* Chapter 5 is accepted by *Journal of Materials Science in June, 2012*

homogeneity of the porous structure of the resulting composites. The concentrations of NaCl in all suspensions were maintained at 0.5 M. To promote the gelation, NaOH was added to the suspensions before the introduction of salt to adjust the suspension pH to ~7.8. Immediately after the injection of salt, suspensions were mixed and transferred into silicone rubber molds (50 mm diameter, 2 mm deep), where the suspensions were kept for 1 h to complete the sol-to-gel transition. Afterwards, gels along with the molds were put into an Advantage Freeze Dryer (SP Industries VirTis, Gardiner, NY) to execute freezing and sublimation. The freezing and sintering conditions are same as to those in Chapter 4.

To facilitate comparisons between samples of different compositions and confirm that all of the observed phenomena were caused by kaolinite addition instead of changes in the total solids loading, the total solids concentration (silica nanoparticles plus kaolinite platelets) was fixed at 18 vol% in each sample, meaning that as the kaolinite content increased, the silica content decreased by an equal amount. Aqueous suspensions containing kaolinite concentrations of 0, 6, 10, 14, and 18 vol% were prepared. Again, the freeze casting for 18 vol% kaolinite (0 vol% silica) was performed immediately after the sample was poured into the silicone mold to minimize sedimentation of the kaolinite platelets.

5.1.2 Characterization

The microstructures of the composites were observed using a field emission scanning electron microscope (SEM, LEO1550, Carl Zeiss MicroImaging Inc., Thornwood, NY), with a 3 nm Au-Pt layer coating applied before the examination. Images of the cross-sections of the composite samples were obtained by breaking the samples by hand and imaging one of the exposed surfaces. The phase transformations that occurred during sintering were monitored using X-ray diffraction (X'Pert PRO diffractometer, PANalytical B.V., EA Almelo, The Netherlands). The absolute densities were measured by a pycnometer (AccuPyc 1330, Micromeritics, Norcross, GA), the actual sample weight was measured by a balance, and the sample volumes were measured using a caliper. The relative densities were calculated and the open porosities were obtained based on these relative densities. The equibiaxial flexural strength of the freeze-cast composites was measured by a strength test apparatus. The details and the instrument schematic illustration have been elaborated in Chapter 3. Typical values of the Poisson's ratio for the composite ranged between 0.21 and 0.30.

5.2 Results

5.2.1 Microstructure observations

A homogeneous microstructure with interconnected pores is obtained after freeze casting (Fig. 5-1a). The pore walls consist of kaolinite platelets and silica nanoparticles bonded together (Fig. 5-1a insert) and this process has been extensively discussed in previous chapters. The subsequent sintering process causes diffusion between the kaolinite and silica materials and results in changes in this microstructure. While the porous microstructure is conserved, the near-spherical pores seen in the green body become more elongated upon sintering at 1000°C (Fig. 5-1b). Both individual silica nanoparticles and kaolinite platelets are still present, and the pore walls are still formed by these bonded particles (Fig. 5-1b insert). In chapter 4, I presented the results of silica nanoparticle size evolution upon sintering at 1000°C, by measuring the nanoparticle sizes in the SEM images . The size of the silica nanoparticles was found to decrease significantly upon sintering, indicating diffusion from the silica to the kaolinite. When the sintering temperature is increased to 1250ºC, the pore shape becomes even more elongated (Fig. 5-1c). Individual silica nanoparticles and kaolinite platelets can no longer be identified, as both species have fused to form the pore walls (Fig. 5-1c insert). This sharp modification in microstructure indicates enhanced diffusion between kaolinite and silica species and the formation of new phases, which is discussed in greater detail below (Section 5.3.2).

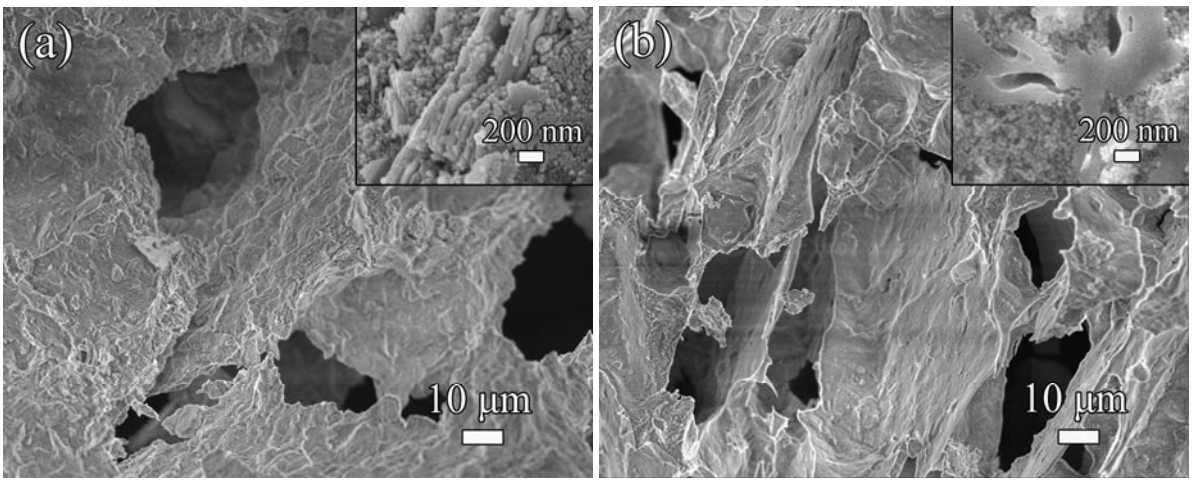

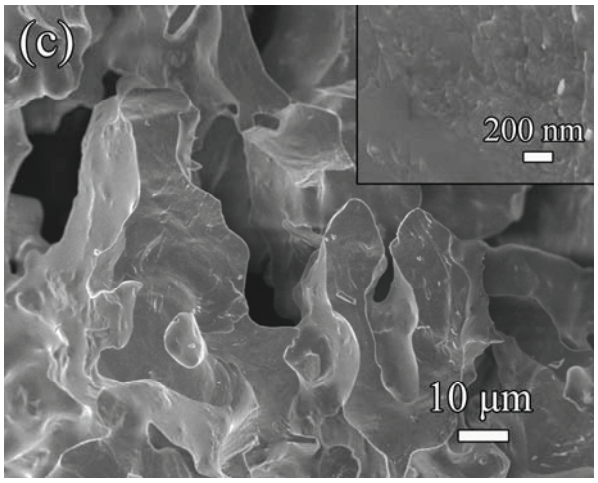

Fig. 5-1. Microstructures of the kaolinite-silica nanocomposites (10 vol% kaolinite, 8 vol% silica): (a) freeze-cast green sample, (b) 1000°C sintered sample, (c) 1250°C sintered sample.

5.2.2 Strength measurements

Fig. 5-2 shows the results from the flexural strength measurements. The graph plots strength versus kaolinite concentration for the freeze-cast green body and for the samples sintered at either 1000°C or 1250°C. There are several observations from these graphs that should be noted.

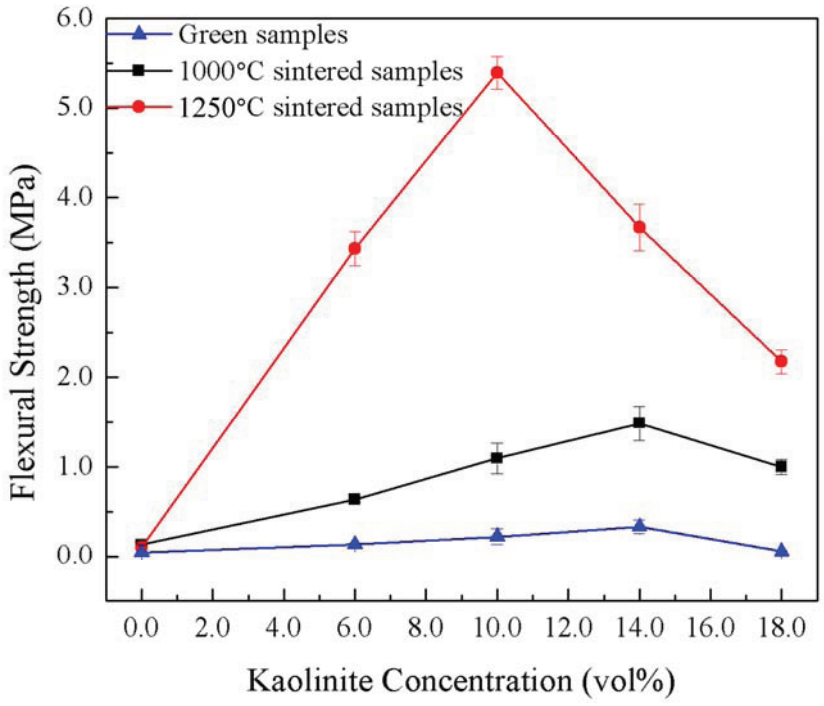

Fig. 5-2. Results of equibiaxial flexural strength measurements for the freeze-cast and sintered samples as a function of kaolinite content. The error bars represent the standard deviation of 5 measurements for each sample. Some of the error bars are very small and are overlapped by the symbols.

First, as expected, sintering increases the strength for all the samples, regardless of the kaolinite content. Furthermore, for all the samples except for the silica-only sample, increasing the sintering temperature increases the strength. (For the silica-only sample, sintering to 1000°C increases the strength by roughly a factor of three compared to the green sample, however, no further increase in strength is achieved by sintering at 1250°C.)

Second, the samples containing a binary mixture of kaolinite and silica are always stronger than those containing only silica or only kaolinite. For the green samples, the maximum strength occurs at 14 vol% kaolinite, and the strength is approximately 8 times higher than that of the pure silica. As explained in Chapter 3, my hypothesis is that the silica nanoparticles bond the structure together while the large kaolinite platelets distribute any applied stress over a larger area. There is thus a clear synergistic effect of having both materials present. In the 1000°C sintered sample, the maximum strength again occurs at 14 vol% kaolinite, and this maximum strength is approximately 11 times greater than that of the silica-only sample.

Third, upon increasing the sintering temperature to 1250°C, the composition providing the maximum strength shifts slightly to 10 vol% kaolinite. The flexural strength of the material also increases substantially. Specifically, the strength of the 10 vol% kaolinite sample is now approximately 52 times greater than that of the silica-only sample, and 3.6 times greater than that of the 14 vol% kaolinite sample sintered at 1000°C.

5.2.3 Porosity measurements

While sintering clearly increases the strength of the materials, the overall porous microstructure is preserved in all of the investigated samples. Plots of the measured porosity of these samples are shown in Fig. 5-3. The dashed line in this figure gives the porosity of the green sample, which is assumed to be a constant value of 82% since all of the samples had a constant solids loading of 18 vol%. Note that in general, the porosity of the freeze-cast green samples is influenced by several factors, including wetting of the particles by the dispersing medium,

rejection of the suspended particles at the solidification front, and volume expansion of the dispersing medium.[57] For the particular samples described here, very little change in sample volume was observed during freeze casting, meaning that the porosity should be approximately equal to the water volume fraction of the suspension (i.e. 82%). The two solid lines give the porosity for the samples sintered at 1000°C and 1250°C. A number of observations should be noted about these results.

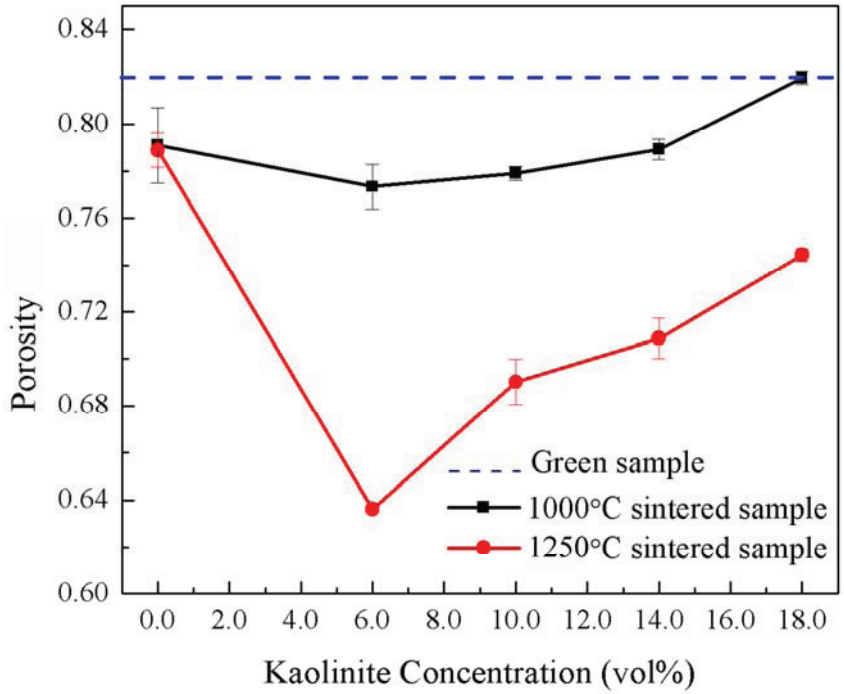

Fig. 5-3. Results of porosity measurements for freeze-cast green samples and sintered samples as a function of kaolinite content. The error bars represent the standard deviation of 5 measurements for each sample. Some of the error bars are very small and are covered by the symbols.

First, for the pure silica sample, sintering at 1000°C causes a slight drop in porosity (from 82% to approximately 79%), however, increasing the sintering temperature further to 1250°C causes no further porosity decrease. This is consistent with X-ray diffraction studies conducted previously in which no significant changes in the patterns for pure silica were seen upon raising the sintering temperature (as explained in Chapter 4). For the kaolinite-only sample, no change in porosity is seen upon sintering at 1000°C, though the diffraction patterns for the kaolinite-only

samples showed a marked loss of crystallinity (as explained in Chapter 4). Upon sintering at 1250°C, a significant drop in porosity (to 76%) is observed for the kaolinite-only sample.

The second observation is that sintering binary mixtures of the silica and the kaolinite produces samples that have a lower porosity than that of either the silica-only or kaolinite-only samples. Thus as with the strength measurements, this observation clearly suggests that the kaolinite and silica nanoparticles are interacting together.

Third, the strength peak and the porosity minima are not present at the same kaolinite concentration for either the 1000°C or 1250°C sintered composites. In spite of the fact that the composition at which the maximum strength occurs shifts with increasing sintering temperature, the minimum porosity remains at 6 vol% kaolinite – the lowest kaolinite concentrations used for the composite samples. In previous studies, it was found that during sintering the silica nanoparticles actually shrink and diffuse into the kaolinite platelets (as explained in Chapter 4). The results presented here suggest that this diffusion not only involves those nanoparticles adjacent to the kaolinite platelets but nanoparticles further into the bulk as well. As a result, composite samples containing greater amounts of silica display greater shrinkage.

Finally, by comparing the results of Figs. 5-2 and 5-3, it can be seen that at the compositions of maximum strength (14 vol% kaolinite for the 1000°C sample and 10 vol% kaolinite for the 1250°C sample), the samples still maintain a relatively high porosity (79% and 69%, respectively) after sintering. Furthermore, I believe that these pores are interconnected, as water could be passed easily through circular disks of the sintered samples upon application of a slight differential pressure.

5.3 Discussion

It is my hypothesis that the ability of the kaolinite to increase the strength of the composites arises from three factors. First, the relatively large size and inherent strength of the platelets, especially when stacked together, allows for the distribution of any applied load over a larger volume of the sample, which reduces the local stress at any single point. Second, new species form at the kaolinite-silica interface upon sintering at 1250°C and these interfacial phases provides additional enhancement of the strength. For the composite, the new phases (mullite and sillimanite) also strengthen the samples since transgrain fracture is present. Third, SEM images of the pore walls in the sintered composite samples show that as the relative concentration of

silica is increased, the walls become much more continuous and unbroken. Each of these mechanisms is discussed in greater detail below.

5.3.1 Distribution of applied stress by the kaolinite platelets

As mentioned above, the kaolinite particles used in my study are plate-like with diameters ranging from 200 nm to 6 μm and thicknesses between 50 nm and 200 nm. This primarily two-dimensional geometry provides strength and stiffness in the plane of the disks. In addition, the plates can be packed more closely than fibers or spherical particles when aligned in a parallel arrangement.[153] Because of their relatively large size compared to the nanoparticles and the two-dimensional structure, the platelets are able to distribute any applied stress over a large number of connected nanoparticles, thus preventing localized stress fractures. In addition, the randomly arrayed platelets (or packed stacks) offer resistance to fatigue cracks.[153, 154] It should be noted that fibers and particles have been used to improve the mechanical properties of other ceramic composites, such as needle-like mullite in a zirconia matrix[155] and SiC whiskers or ZrO_2 particles in mullite[156]. Although these previous works used particles with different shapes from mine, many of the basic strengthening mechanisms are similar (load transfer[155] and resistance to crack propagation[154]). In these composites, the matrix materials bond the added particles together and transferred applied load more uniformly to the particles in the network.[153] Because the new phase observed upon sintering to 1250^{o}C are not seen in either the green samples or in samples sintered at 1000°C, it is likely that this first mechanism, namely distribution of applied stress, is the dominant strengthening mechanism in these materials (i.e., those not sintered at 1250^{o}C).

It is interesting to note that having too much kaolinite present actually leads to weaker samples. I hypothesize that the silica nanoparticles are necessary to form a network connecting the platelets together. Specifically, because of their plate-like shape, kaolinite platelets by themselves would have very few contact points and thus would be significantly weaker than composites containing silica and kaolinite, which is exactly what is observed here.

The explanation that the strength results from having both kaolinite platelets (to distribute the load) and silica nanoparticles (to bond the network together) suggest that the maximum strength would occur when all of the nanoparticles present participate in bonding the kaolinite platelets together. As a first approximation, I assume that this will occur when the silica-to-

kaolinite concentrations are such that each platelet is coated with a monolayer of adsorbed silica nanoparticles.

The amount of kaolinite surface area per unit volume of suspension can be expressed as $S_{kaolinite} \cdot \rho_{kaolinite} \cdot V_{kaolinite}$, where $S_{kaolinite}$ is the specific surface area of the kaolinite (reported by the supplier as 7 m^2/g), $\rho_{kaolinite}$ is the kaolinite density (measured by water replacement as 2560 kg/m^3), and $V_{kaolinite}$ is the volume fraction of kaolinite used in the suspension.

As shown in Figure 5-4, the adsorbed silica nanoparticles are arranged in a hexagonal close-packed array on the kaolinite platelets, such that the area that each silica sphere occupies is $\sqrt{3}d^2/2$, and the amount of area per unit volume of suspension that can be covered by the silica nanoparticles can be expressed by $3\sqrt{3}V_{silica}/\pi d$, where V_{silica} is the volume fraction of silica used in the suspension and d is the average diameter of the silica nanoparticles (22 nm). Equating these two expressions yields:

$$\frac{3\sqrt{3}(V - V_{kaolinite})}{\pi d} = S_{kaolinite} \cdot \rho_{kaolinite} \cdot V_{kaolinite} \tag{5-1}$$

where I have used the identity $V_{kaolinite} + V_{silica} = V$, where V is the total solids loading in the suspension (18% in this work). Solving Eq. (5-1) for $V_{kaolinite}$ yields a kaolinite concentration of 14.5 vol%, which is remarkably close to the value of 14 vol% found experimentally in the green samples and 1000°C sintered samples (Fig. 5-2). This agreement confirms my hypothesis regarding the number of nanoparticles needed for maximum strength and indicates the multilayers of nanoparticles on each platelet actually weaken the sample strength compared to monolayer coverage.

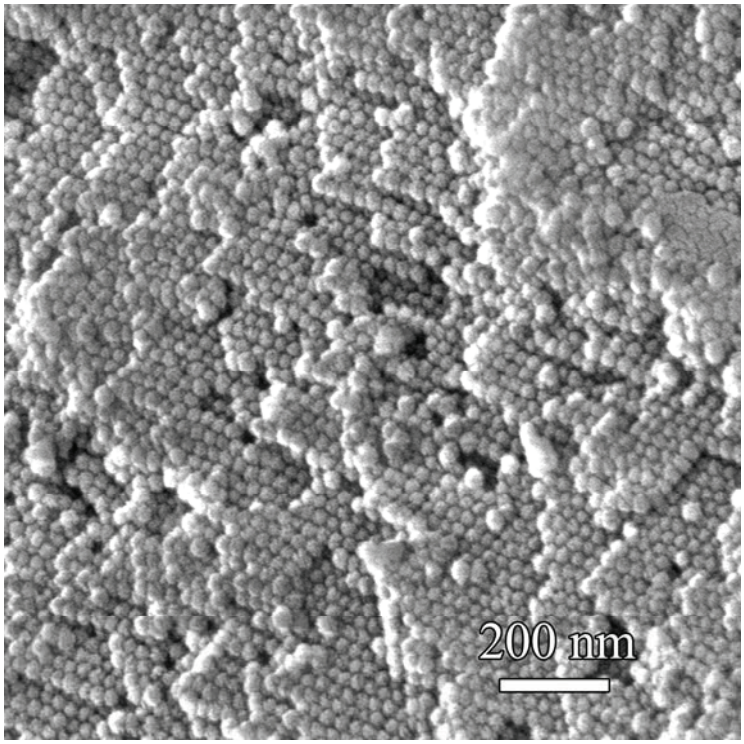

Fig. 5-4. SEM image showing hexagonal packing of the nanoparticles

5.3.2 Interfacial phase reinforcement

Upon increasing the sintering temperature to 1250°C, experiments show that the maximum strength occurs at a lower kaolinite loading, specifically at 10 vol% kaolinite and 8 vol% silica. This shift suggests that the formation of an interfacial phase at the higher temperature, along with the phase transformation of kaolinite itself, is an important factor in maximizing the sample strength. This additional interfacial species possesses a transitioning crystal structure close to α-cristobalite that bonds mullite/sillimanite and silica phases. The relative fraction of the interfacial species in the composite with different initial compositions can be analyzed by comparing their XRD patterns (Fig. 5-5a). The typical peak for this interfacial phase appears in the XRD profiles at 21.69° and is only observed when the sintering temperature reaches 1250°C. This peak is higher for the 10 vol% kaolinite sample than for either 6 vol% or 14 vol% kaolinite sample, indicating that the 10 vol% kaolinite sample contains the highest fraction of the interfacial species. This observation suggests that the amount of interfacial interaction between silica and kaolinite is maximized in samples containing only 10 vol% kaolinite and 8 vol% silica. My speculation is that the formation of the interfacial species

involves not only the silica nanoparticles adjacent to the kaolinite platelets but also nanoparticles further away from the kaolinite platelets. However, the lowest peak intensities of the 6 vol% kaolinite sample suggest that there is a range limit for the nanoparticles to participate in the formation of the interfacial phase. This least crystallinity for the composite with highest silica content indicates the pure silica phase transformation is inhibited by the present of kaolinite and the excessive silica is still amorphous at this stage and participating the complex phase transformation with kaolinite species. The optimal composition for the new phase formation is around 10 vol% kaolinite plus 8 vol%. This high interfacial phase fraction in the 10 vol% kaolinite sample in combination with a better distribution of silica, mullite, and sillimanite phases provides the composite with improved strength.

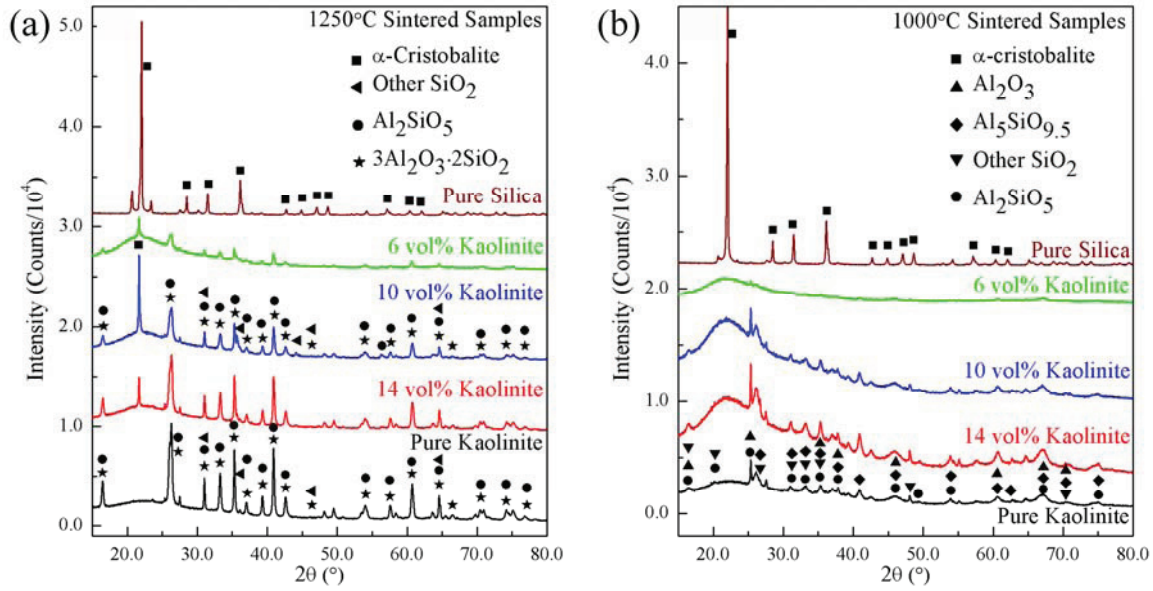

Fig. 5-5. X-ray diffraction patterns on samples containing varying amounts of silica and kaolinite: (a) 1250°C sintered sample, (b) 1000°C sintered sample.

As shown in Figure 5-5b, expect for the silica-only sample that possesses a tetragonal crystalline structure similar to that sintered at 1250°C, the 1000°C sintered kaolinite-only sample and composites have less prominent peaks and appears to be in the middle of the phase transformation. This phenomenon indicates that the interfacial phase does not form until sintering temperature increased to 1250°C, and this interfacial phase reinforcement only effective at high sintering temperature (>1250°C).

5.3.3 Reduction of stress concentrator

The third strengthening mechanism proposed involves the observed structure of the pore walls in the 1250°C sintered samples. Shown in Fig. 5-6 are SEM images of the composite samples containing 6, 10, 14 and 18 vol% kaolinite. Comparing the four images, it is clear that as the kaolinite concentration decreases (silica concentration increases), the pore walls become much more continuous and contain fewer voids. In addition, much more granularity can be seen in the sample containing 18 vol% kaolinite (Fig. 5-6d). My hypothesis is that these voids in the pore walls are caused by irregular packing of the plate-like kaolinite particles, which furthermore can be filled by the silica nanoparticles when a sufficient concentration of the latter is present.

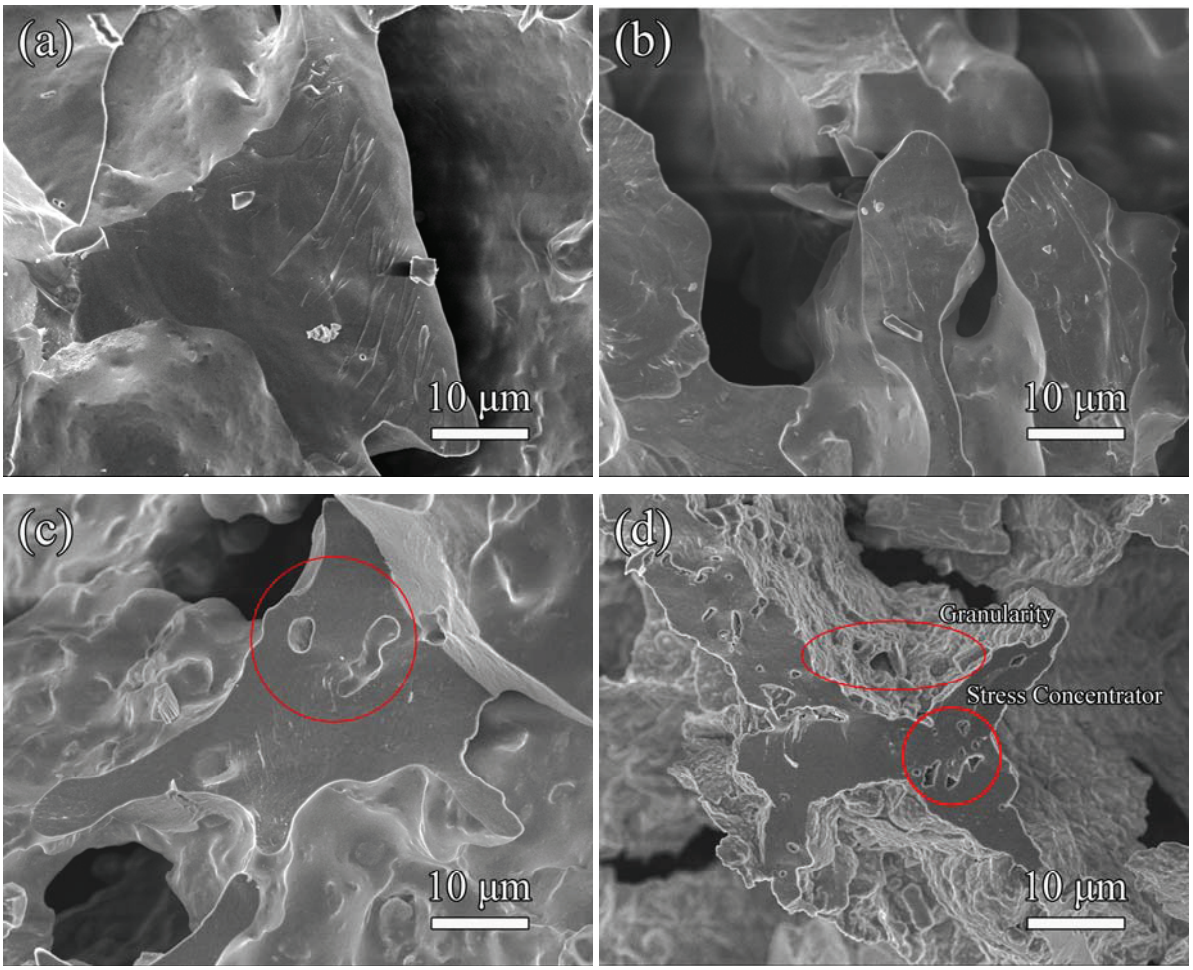

Fig. 5-6. SEM images showing the microstructure of the pore walls for the 1250^{o}C sintered composite samples with varying composition: (a) 6 vol% kaolinite, (b) 10 vol% kaolinite, (c) 14 vol% kaolinite, (d) 18 vol% kaolinite.

Whatever the exact cause, it seems clear that such voids and granularity could affect the overall strength of the composite. Specifically, these micron-sized voids and the rough pore wall surfaces may serve as stress concentrators when an external load is applied. Cracks initiated from these locations could spawn fast fracture. If the number of such voids increases, such as is seen in the samples with higher kaolinite loadings, a greater number of cracks can be formed, leading to faster failure.

Perhaps one of the more interesting findings from this work is that the composition of the sample that provides the highest strength is not the same as the one that yields the lowest porosity. While the shrinkage of the sample during sintering could help increase the strength, this effect is obviously not as important as some of the other mechanisms presented here. This slight disconnection between porosity and strength means that it is possible to design samples with high porosities without a significant loss of strength.

Finally, it should be mentioned that these three different mechanisms of strength enhancement (*i.e.*, bonded network for load distribution, formation of new phases, and reduction of stress concentrators) may also be applicable to other ceramic composite systems besides the kaolinite-silica system used here. While the ability of large platelets to distribute load is a general phenomenon that would be broadly applicable, the key issue would be whether new and stronger phases (or interfacial species), along with continuous and dense pore walls could be formed at appropriate sintering conditions.

5.4 Conclusions

It has been shown that the plate-like kaolinite particles present in sintered silica-kaolinite nanocomposites can substantially improve the strength of the material. When sintered at 1000°C, the kaolinite content for the optimum strength occurs in samples containing 14 vol% kaolinite and the equibiaxial strength at this concentration is 11 times greater than that of silica-only samples. For the samples sintered at 1250°C, at the optimum kaolinite content (10 vol% kaolinite and 8 vol% silica for the samples used here), the equibiaxial strength (5.4 MPa) is 52 times

greater than the samples containing only silica and 2.5 times greater than the samples containing only kaolinite. In addition, these increases in strength can be achieved without a significant sacrifice in porosity (*i.e.*, 69% porosity for the optimum concentrations, versus 79% and 76% porosity for the samples containing only silica or only kaolinite, respectively).

I hypothesize that this strength increase arises from three independent effects. First, the large size and inherent strength of the kaolinite platelets allow distribution of any applied load over a much larger region of the connected network, which reduces local stresses. Second, at the 1250°C sintering temperature, the kaolinite and silica diffuse together to form a new interfacial phase and the kaolinite itself transforms into stronger phases, further increasing the sample strength. Third, the silica nanoparticles are able to 'fill in' the voids in the walls of the porous structure caused by irregular packing of the kaolinite platelets, which eliminates fracture sites.

CHAPTER 6. SOLIDS LOADING EFFECT ON THE KAOLINITE-SILICA COMPOSITES*

Abstract

Kaolinite-silica nanocomposites with a green porosity ranging from 75% to 87% were prepared using a freeze-casting technique. The initial solids loading values (kaolinite platelets plus silica nanospheres) was varied between 12 and 24 vol% and was found to greatly influence both the sintering behavior as well as the phase and strength of the resulting porous composites. The composites with lower solids loading exhibited faster sintering (e.g. larger shrinkage, more extensive thickening of the pore walls) when sintered at 1250°C, which, in turn, resulted in a rapid increase in mechanical strength. All the composites maintained a high porosity (above 50%) after sintering at 1250°C for 72 hrs, while the flexural strength of the composites increased up to 13.3 MPa. It is believed that solids loading affects kaolinite-silica packing during the sol-to-gel transition as a minimum amount of silica nanoparticles is required to build the gel network. This particle packing difference influences the amount of kaolinite-silica interface, which in turns affects the strength. The strength increase through solids loading change is a combined effect of changes in the porous structure during sintering plus the development of a new phase at the silica-kaolinite interface.

6.1 Experimental procedure

6.1.1 Raw materials and sample preparation

Details of the materials used and the sample preparation procedure were described in Chapters 3 and 5. The kaolinite-to-silica ratio in all of the samples was fixed at 1:1, while a series of composites with solids loadings of 12%, 18%, and 24% were examined. After freeze casting, the samples were de-molded and sintered at 1250°C for 1 hr, 12 hrs, 24 hrs and 72 hrs, respectively, with heating and cooling rate of 5°C/min.

* Chapter 6 is to be submitted to *Journal of the American Ceramic Society*

6.1.2 Characterization

The porosity and linear shrinkage of the sintered samples were calculated using the measured dimensions and weights. The absolute densities of the dense composites were measured by a pycnometer (AccuPyc 1330, Micromeritics, Norcross, GA). The microstructures of the porous composites were observed using a field emission scanning electron microscope (SEM, LEO1550, Carl Zeiss MicroImaging Inc., Thornwood, NY), with a 3 nm Au-Pt layer coating applied before the examination. Images were taken from the cross-sections of the samples, which were obtained by breaking the samples by hand. X-ray diffraction (X'Pert PRO diffractometer, PANalytical B.V., EA Almelo, The Netherlands) was used to identify the phase evolution of the composites during the sintering process. Equibiaxial flexural strength measurements were carried out following ASTM C 1499,[146] using a strength test apparatus with a 1 kN load cell (Instron 4204, Instron, Norwood, MA). Details of the flexural strength test and the instrument schematic illustration were elaborated in Chapter 3. Poisson's ratio for a pore-free composite was obtained by linear interpolation between the Poisson's ratios of pure silica (0.17) and pure kaolinite (0.45)[147] using the known concentrations of these components in the samples. Typical values of the Poisson's ratio for the composite ranged between 0.20 and 0.24.

6.2 Results and discussion

6.2.1 Densification at different solids loading

6.2.1.1 Porous microstructure observation

During freeze casting, the pores are fabricated when the solidified dispersing medium (i.e. ice crystals) is displaced, such that the pore morphologies replicate those of the ice crystals. The microstructure evolves with the subsequent sintering process. In this work, homogeneous freeze casting is applied and the directional growth of the ice crystals is inhibited as demonstrated by the homogeneous porous microstructure. Specifically, negligible temperature gradient (i.e. thin sample thickness and low freezing rate) and high particle resistance to the moving solidification fronts (i.e. large disk-like kaolinite particles and gel state) ensure a uniform distribution of ice crystals, and therefore a homogeneous porous microstructures. Shown in Fig. 6-1a are SEM images displaying the cross-sectional microstructures of the 12 vol% (left) and 24 vol% (right) solids loading composites at green state. The pores at this stage appear to be

interconnected. The low solids loading sample (12 vol%) possesses higher porosity and larger pore size; the pore walls also appear denser and smoother. This is because the higher solids loading sample (24 vol%) has more surfaces acting as nucleation sites, and the increased solids restrict the continuous growth of the ice crystals and subsequently results in more but smaller pores. Because of their small sizes (i.e. nanometer and micrometer), all particles in the suspensions can be effectively repulsed from the solidification fronts due to the relatively low cooling rate. Thus, the small number of ice crystals in the low solids loading sample can continuously grow for a relatively long distance as a result of less solid restriction.

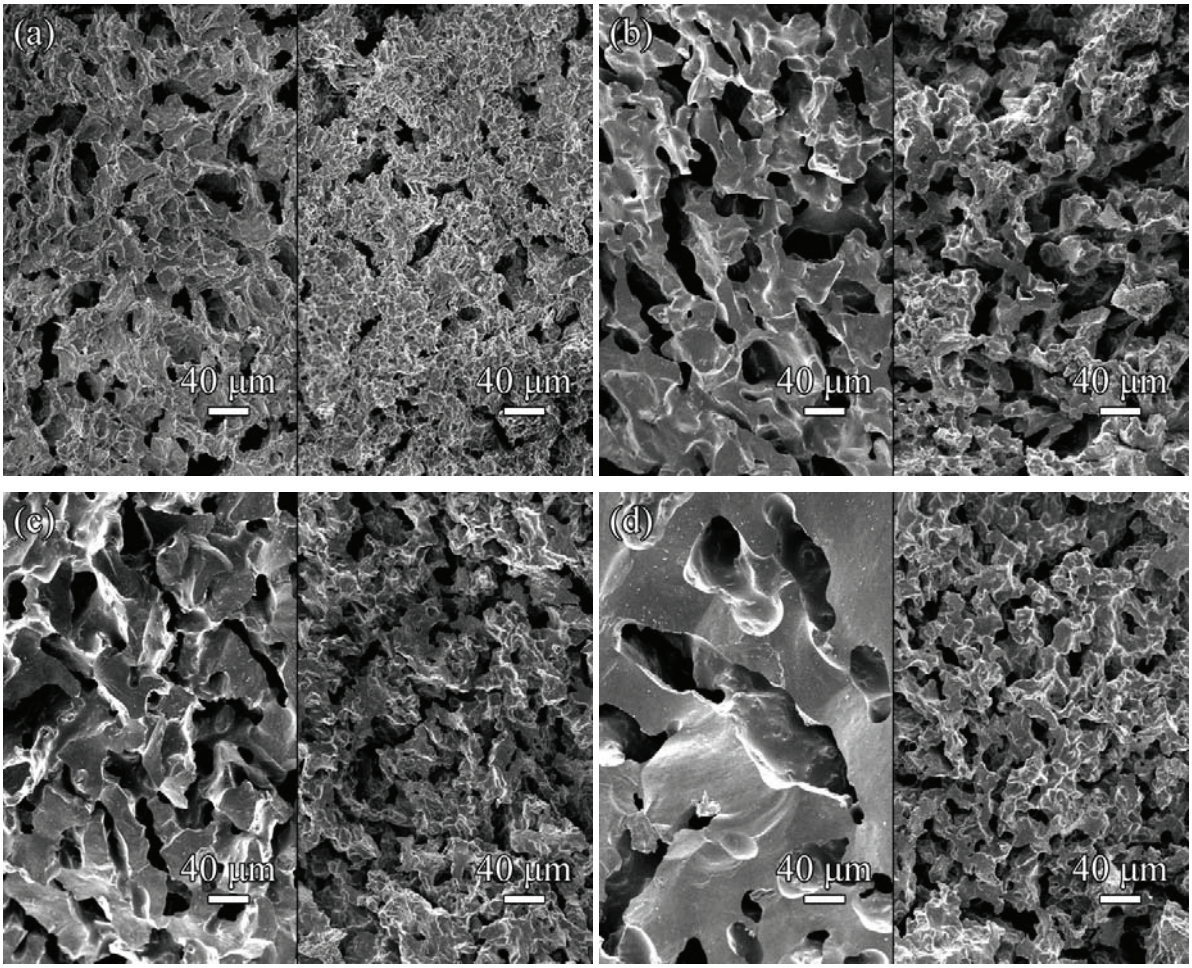

Fig. 6-1. Porous microstructures of composites at: (a) green state, (b) 1250°C sintering for 1 hr, (c) 1250°C sintering for 24 hrs, and (d) 1250°C sintering for 72 hrs. In all the images, the left side shows the 12 vol% solids loading sample, while the right side shows the 24 vol% solids loading sample.

The microstructure evolution with the sintering time is shown in Fig. 6-1b to 6-1d for the composites with 12 vol% and 24 vol% solids loadings. The pore morphology evolves throughout the sintering process, and the general trend is shared by all the samples regardless of the solids loading. At the beginning of the sintering process (i.e. green state to 1 hr sintering at 1250°C), small pores merge into larger ones. In other words, large pores (i.e. micron pores) grow at the consumption of small pores (i.e. nano-pores and sub-micron pores).[117,157] At the same time, both densification and grain growth occur during this stage. From a closer view, no individual silica nanoparticles or kaolinite platelets identified in the green state can be found in the sintered samples. Particle surface energy reduction and reactions between the two species (elaborated in section 3(2)) provide the driving force for the sintering during this stage. The pore walls are densified at the expense of the particle surface area reduction. The pore sizes increase in both samples (Fig. 6-1b), though the pores in the 12 vol% solids loading sample are elongated while the pores in the 24 vol% solids loading sample are more circular.

From 1 hr to 24 hrs of sintering time, the densification is accompanied by pore shrinkage and thickening of the pore walls (Fig. 6-1c). The shrinkage of the pores suggests diffusion plays an important role during the sintering process. The pores are still elongated in this stage and appear interconnected. The microstructure evolution slows down compared to earlier sintering state as the sintering driving force decreases with the loss of the surface area.

When the sintering time further increases to 72 hrs, the removal of the pores continues, and the small pores again merge into larger ones (Figure 1d). Although the pore walls thicken in all the samples, the pore morphology evolution in the 12 vol% solids loading sample is more pronounced. The pore walls thicken by a factor of ~2 and the pores grow to hundreds of microns in size, though the elongated shape is conserved. In contrast, the pore size in the 24 vol% solids loading sample only slightly increases, and the pore morphology remains unchanged. This phenomenon suggests that the low solids loading samples have more rapid sintering than the high solids loading samples at this stage.

One remarkable difference associated with the solids loading is demonstrated by the pore wall structure. The low solids loading sample always has thicker pore walls than the high solids loading sample. The former also exhibits more fracture surface through the pore walls (>50%). This phenomenon suggests that initial solids loading may directly affect mechanical strength.

6.2.1.2 Loss of porosity

In general, the porosity of the freeze-cast green sample does not depend only on the solids loading, but is a function of a variety of factors, such as wetting of the dispersing medium on the particles, rejection of the suspended particles at the solidification front, and volume expansion of the dispersing medium.[57] In this work, these factors do not seem to be significant, as the final porosities of the samples are very close to the initial solids loadings. For the 12 vol%, 18 vol%, and 24 vol% solids loading samples, the porosities are at ~87%, ~80%, and ~75%, respectively, as plotted in Fig. 6-2.

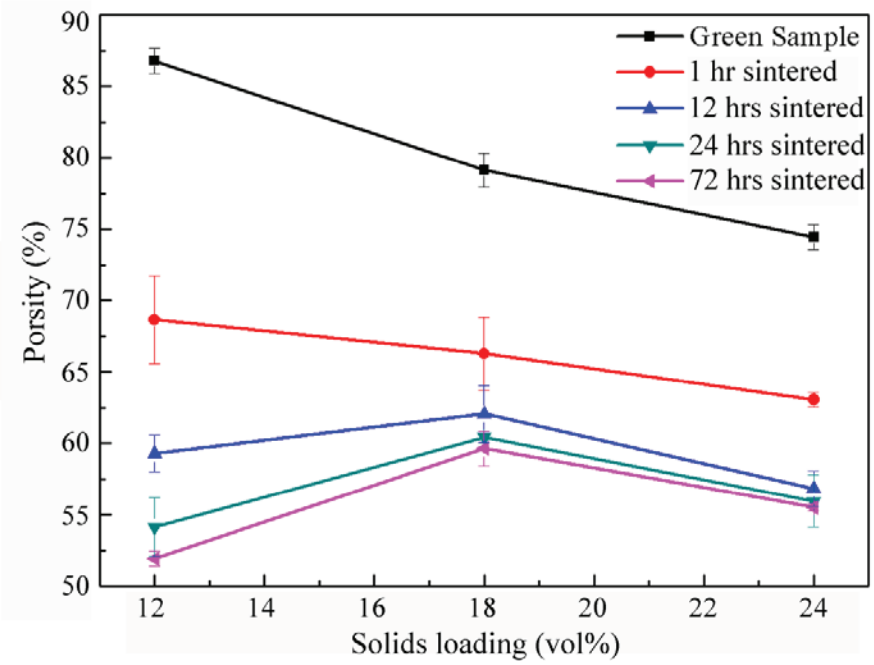

Fig. 6-2. Porosity evolution with sintering time at 1250°C for composites with initial solids loading of 12 vol%, 18 vol%, and 24 vol%.

The porosity evolution with sintering time for the samples with different initial solids loadings is also plotted in Fig. 6-2, and several observations can be made. First, all the samples shrink as the sintering time increases regardless of the solids loading; however, high porosities (greater than 50%) are conserved after 72 hrs of sintering at 1250°C. Second, the densification rate decreases with time as a result of loss of sintering driving force (i.e. loss of surface energy

and slow-down of the chemical reactions). Third, the porosity evolution varies with the solids loading. At the beginning of the sintering, all three samples have rapid densification; the loss of porosity is 18.1%/hr, 12.8%/hr, and 11.1%/hr for the 12 vol%, 18 vol%, and 24 vol% solids loading samples, respectively. Densification increases with solids loading decrease. My explanation is that thicker pore walls in the low solids loading sample facilitate the diffusion of the species and the densification. However, with sintering time increase (i.e. 1 hr to 24 hrs at 1250°C), densification decreases from 12 vol%, to 24 vol%, and to 18 vol% solids loading samples (from 0.63%/hr, to 0.30%/hr, and to 0.25%/hr). Although the 24 vol% solids loading sample has the thinnest pore walls, it possesses the most interlocked solid network. This higher level network provides more pathways for the diffusing species and promotes the sintering diffusion. It is my hypothesis that both the thicker pore walls for the low solids loading sample and the larger number of diffusing pathways for the high solids loading sample facilitate the densification. As a result, the 18 vol% solids loading sample with a microstructure in-between the two extremes is left with lower shrinkage rate. With longer sintering time (i.e. 24 hrs to 72 hrs), all the samples have slow densification (less than 0.05%/hr), while the 12 vol% solids loading sample still has the largest shrinkage. The 18 vol% solids loading sample always has the highest porosity when the holding time exceeds 12 hrs.

6.2.2 Phase transformation during sintering

In addition to the porous structure, the chemical reactions that lead to phase transformation in the kaolinite-silica composites are another issue that complicates the sintering behaviors. At the green state, the silica nanoparticles are amorphous and the kaolinite platelets have a typical kaolinite ($Al_2Si_2O_5(OH)_4$) crystal structure. Fig. 6-3 shows the phase evolution of the composites with the solids loading from 12 vol% to 24 vol% and the sintering time from 1 hr to 24 hrs. Continuous phase development occurs in all the samples. The composites gradually develop into a mixture of mullite, sillimanite, and crystallized silica phases. A sharp peak develops around 21.69° in all the composites corresponding to the formation and development of a tetragonal transitioning interfacial phase, which has been analyzed and discussed in Chapter 4. With sintering time increase, significant development of the interfacial phase is identified.

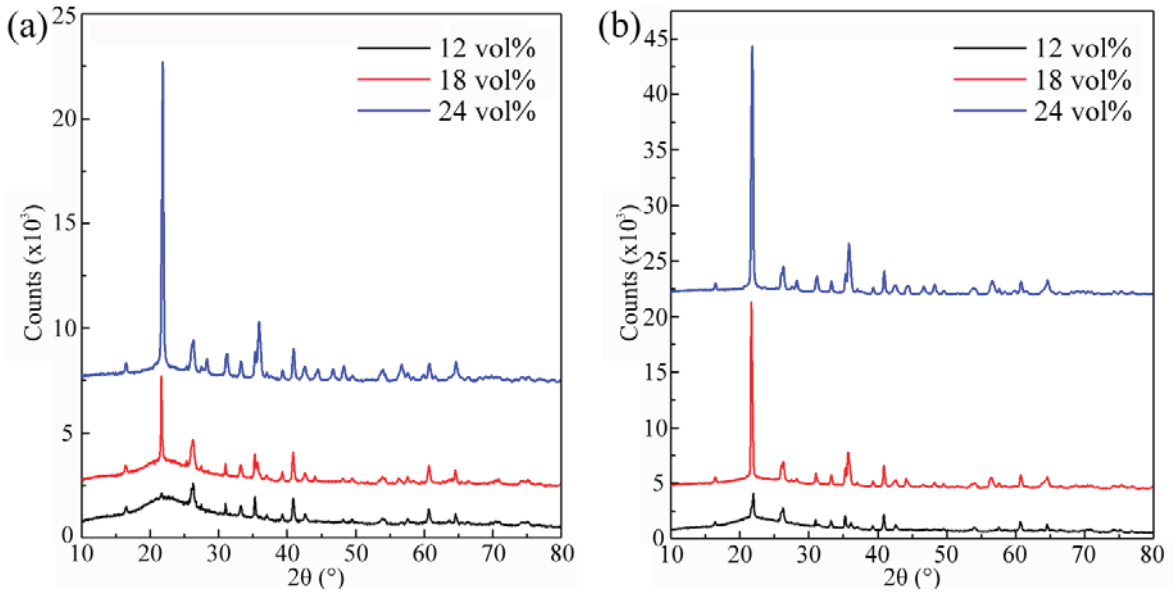

Fig. 6-3. XRD diffraction patterns of composites with 12 vol%, 18vol%, and 24vol% solids loading: (a) sintered at 1250°C for 1 hr, (b) sintered at 1250°C for 24 hrs. The indexing of the peaks is not shown as they are the same as in Fig. 4-5 and Fig. 4-10.

One surprising finding is that the amount of the interfacial tetragonal phase differs with solids loading, although all the composites have the same relative composition. The interfacial tetragonal phase percentage in each composite can be quantified by calculating the peak areas in the XRD patterns and the results are shown in Table 6-1. The interfacial tetragonal phase content increases with both sintering time and solids loading increases.

Table 6-1. Interfacial tetragonal phase percentage based on calculations from XRD peak areas.

Initial solids loading	Green	1 h sintering at 1250°C	24 h sintering at 1250°C	72 h sintering at 1250°C
12 vol%	0	11.63%±0.06%	12.79%±0.08%	12.86%±0.24%
18 vol%	0	13.40%±0.23%	16.29%±0.22%	16.33%±0.26%
24 vol%	0	16.70%±0.17%	17.41%±0.45%	17.86%±0.24%

This interfacial tetragonal phase is believed to develop through the reactions between kaolinite and silica particles and requires the two species to be close. The difference in the phase percentage with the solids loading indicates that the initial solids loading affects the particle

packing. Specifically, the 12 vol% solids loading sample possesses the lowest amount of the interfacial phase at each stage, suggesting that the low solids loading leads to fewer kaolinite-silica contacts. My explanation is that there exists a required amount of silica content to build the gel network during the sol-to-gel transition and only the silica nanoparticles left can effectively participate in the interaction with kaolinite platelets. Previously, Baird and Walz found that a minimum amount of silica nanoparticles (5.5 vol% for 0.5 M NaCl) is required to form the solid-like gel phase.[33] These nanoparticles bond together to form the network and result in large agglomeration of silica nanoparticles. In the 12 vol% solids loading sample (i.e. 6 vol% kaolinite plus 6 vol% silica), only 0.5 vol% silica can move freely to interact and bond with the 6 vol% kaolinite, and the silica-to-kaolinite ratio is 1-to-12. In contrast, the 24 vol% solids loading sample (i.e. 12 vol% kaolinite plus 12 vol% silica) has 6.5 vol% silica nanoparticles to bond with the 12 vol% kaolinite, and the silica-to-kaolinite ratio is slightly larger than 1-to-2. In each sample, those self-assembled silica nanoparticles are far from the kaolinite species and can hardly participate in the formation of the interfacial species. This huge particle packing efficiency difference results in lower interfacial phase formation in the low solids loading samples, while much more interfacial phase develops in the high solids loading sample. With sintering time increase from 1 hr to 72 hrs, the diffusion and the reaction of the two species continue and the amount of the interfacial phase develops in all the composites.

6.2.3 Strength evolution

Sintering bonds discrete particles together into a solid structure.[117, 125, 158] Therefore, one of the most significant effects of sintering on the macroscopic properties is the strengthening of the composite. Although a fully solid structure is not fabricated in this work, the sintering process does improve the strength of the porous composites by densifying the pore walls, modifying the pore structures, and inducing a phase transformation. The flexural strength evolution with solids loading and sintering time are shown in Fig. 6-4. Again, several observations can be made.

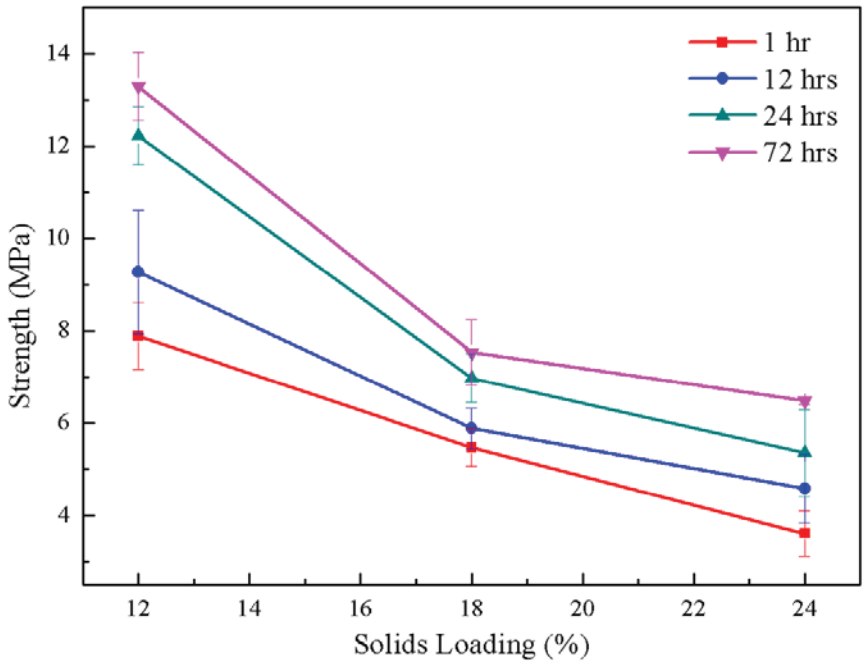

Fig. 6-4. Flexural strengths of 12 vol%, 18 vol%, and 24 vol% solids loading composites after sintering at 1250°C for 1 hr, 12 hrs, 24 hrs, and 72 hrs.

First, all the samples show a continuous increase in strength during sintering, regardless of the solids loading. From 1 hr to 72 hrs, the strengths of the 12 vol%, 18 vol%, and 24 vol% solids loading samples increase by a factor of 1.69, 1.38, and 1.80, respectively. The relative relationship is different from that with the loss of porosity (i.e. 18 vol% solids loading sample has the smallest shrinkage, while the 12 vol% solids loading sample has the largest). The large strength increase of the 24 vol% solids loading sample suggests that the strengthening is controlled by more than one factor.

Second, the flexural strength decreases with the increase of the solids loading, regardless of the sintering time; and this difference increases with sintering time. According to the previous finding, the interfacial phase reinforces the porous composites. The disagreement between the interfacial phase amount and the strength for the samples with different solids loading again indicates that the strengthening effect involves multiple factors. The strengthening mechanisms can be generally divided into two aspects: the microstructure evolution and the phase change.

The first contribution to strengthening comes from the microstructure evolution. Specifically, the densification and thickening of the pore walls (Fig. 6-1), the loss of the porosity

(Fig. 6-2), and the decrease of the pore size (Fig. 6-1) strengthen the porous composites. Since all these processes continue with the sintering time, this mechanism results in continuous increase in the strength. On the other hand, the low solids loading sample possesses denser and thicker pore walls, thus the strength of the sintered samples increase with a decrease of the initial solids loading.

The second contribution in strengthening relies on the interfacial phase development. As this new phase develops continuously with the sintering time, it contributes to the improvement of the composite strength with time.

Overall, both the microstructure evolution and phase development lead to the strength increase with sintering time, however the decrease of the strength as solids loading increases suggests the first mechanism is dominant. Shown in Fig. 6-5 are the microstructures of epoxy-filled/polished cross-sections for the 12 vol% and 24 vol% samples. The lighter phases are the composite materials while the darker areas are the epoxy. In comparison, the pore walls in the lower solids loading sample is denser and thicker than those of the higher solids loading sample. In addition, although there are some thick pore walls in the 24 vol% solids loading sample, the thickness of the pore walls shows a large variation. There are very thin "bridges" (as circled in Fig. 6-5b) connecting denser and thicker walls. These thin "bridges" act as stress concentrators under an applied load and compromise the strength of the porous composite. The SEM images in Fig. 6-1 show that the low solids loading sample (Fig. 6-1c and 6-1d left) has more transgrain fracture than the higher solids loading sample (Fig. 6-1c and 6-1d right). The fracture surfaces of the 12 vol% solids loading sample are more even, while the fracture surfaces of the 24 vol% composite are rougher, indicating the sample breaks through the thin "bridges". Also for the 24 vol% solids loading composite, the microstructure evolution with sintering time is not as significant as the low solids loading samples. Thus, the interfacial species in the 24 vol% composite plays a greater role in strengthening than that in the lower solids loading samples, resulting in a higher strength increase factor (i.e. 1.80) from 1 hr to 72 hrs of sintering.

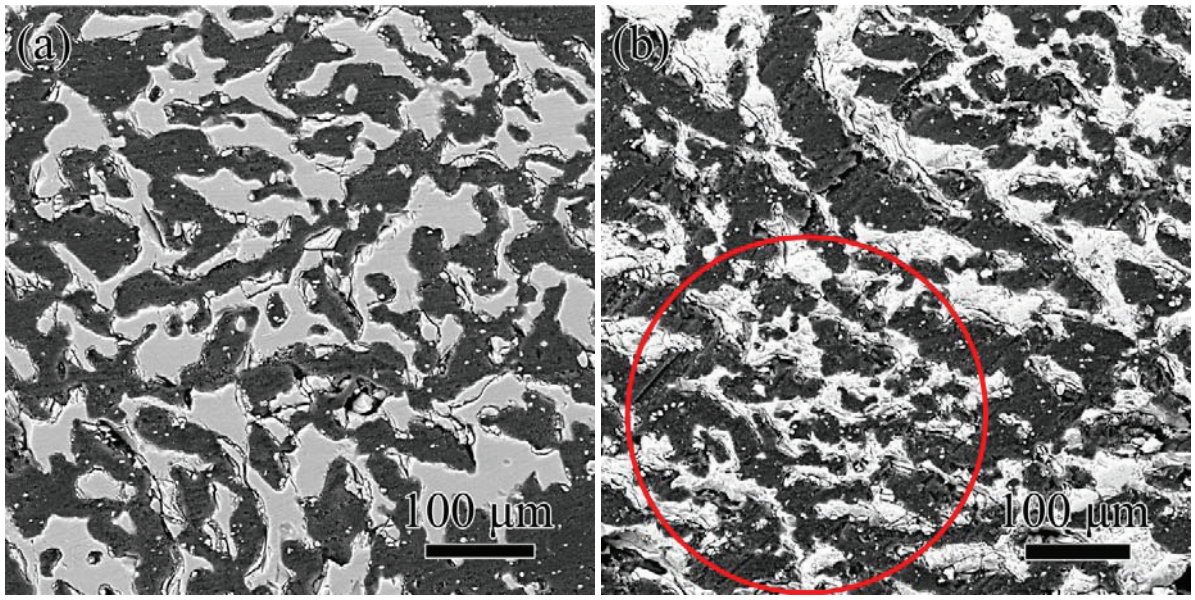

Fig. 6-5. SEM images showing cross-sections of the epoxy-filled porous composites after sintering at 1250°C for 24 hrs with solids loading at (a) 12 vol% and (b) 24 vol%. The circle in (b) points out the thin "bridges".

6.3 Conclusions

In this work, the effects of solids loading on the sintering behavior of freeze-cast kaolinite-silica porous composites are investigated. Although considerable densification occurs in all the samples, the composites have porosities higher than 50% even after 72 hrs of sintering, regardless of the solids loading. The low solids loading sample has faster densification and more considerable microstructure evolution, which, in turn, leads to higher flexural strength. The sintering process is not a simple diffusion process but involves chemical reactions between the kaolinite and silica species. An interfacial species is developed and the amount of this phase depends on both solids loading and sintering time. While the microstructure evolution and the interfacial phase development both impact the strength, the first mechanism is dominant, especially in lower solids loading samples. As a result, the flexural strength for the porous composite increases with the sintering time but decreases with increasing solids loading.

CHAPTER 7. CONTROL OF THE SPECIFIC SURFACE AREA BY SUSPENSION INFILTRATION*

Abstract

I describe a novel method for creating porous ceramics with high specific surface area and high strength. The fabrication procedure involves infiltrating aqueous suspensions of silica nanoparticles into a porous ceramic scaffold. The samples are then freeze-dried to maintain a homogeneous distribution of nanoparticles, followed by partial sintering to bond the infiltrated nanoparticles into place. By repeating this infiltration process multiple times, the specific surface area of the composite can be varied from less than one to well over 100 m^2/g. It is also found that this infiltration increases the mechanical strength of the composite. Water flux experiments demonstrate the potential use of these materials as liquid membranes, with no significant damage to the structure observed after these flux tests.

7.1 Experimental procedure

7.1.1 Raw materials

A 34 wt% silica nanoparticle suspension, kaolinite powder, sodium hydroxide, sodium chloride, and deionized water were used as received to fabricate the porous scaffolds. Ludox TMA (34 wt% silica suspension with 22 nm particles) and Ludox AM (30 wt% silica suspension with 12 nm particles) were used to carry out the suspension infiltration. The density of the silica nanoparticles was 2.37 g/cm^3.[144, 145]

7.1.2 Fabrication of the porous composite scaffold

The fabrication procedure for the porous composite scaffold was described previously in Chapter 5. The initial solids loading in the suspension was 10 vol% kaolinite and 8 vol% Ludox TMA. The porous composites were freeze cast with a freezing rate of 2°C/min and sintered at

* Chapter 7 is to be submitted to *Nature Materials*

1250°C for 1 h, yielding a porous ceramic with a porosity of approximately 70%. The resulting scaffolds were circular disks approximately 40 mm in diameter and 2 mm in thickness.

An SEM micrograph of one of these scaffolds is shown in Fig. 7-1. As seen, the scaffold is highly porous with elongated pores. The pores are of tens of microns in size and apparently well interconnected, as water would easily pass through the material under a slight applied pressure.

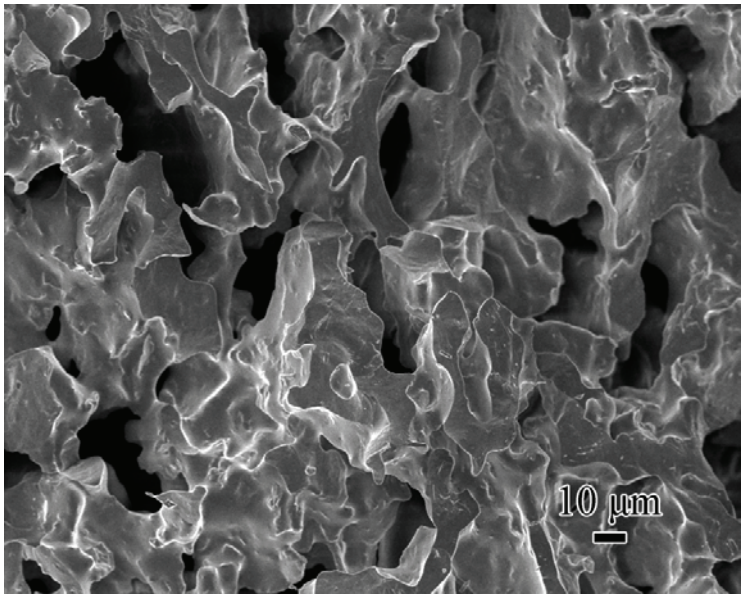

Fig. 7-1. SEM microscopy of the porous scaffolds prior to infiltrating nanoparticles.

7.1.3 Infiltration of the nanoparticles

The porous scaffolds were soaked in the as-received colloidal silica suspensions (i.e. Ludox TMA or Ludox AM) overnight, allowing all the open pores to be fully filled by the suspension. Next, a rapid freezing was applied to the liquid-filled samples by immersion in liquid nitrogen. After freezing, the sample disks were placed into an Advantage Freeze Dryer (SP Industries VirTis, Gardiner, NY) for sublimation. The samples were kept at -35°C and ~1.34 Pa for 400 min to remove the ice crystals. Finally, the dried samples were partially sintered (600°C for Ludox TMA and 400°C for Ludox AM) for 4 h to bond the silica nanoparticles while maintaining their morphology and surface areas. The sintering temperature for each nanoparticle type was separately evaluated, as smaller particles sinter more easily and require lower

temperature to maintain the surface area. The above steps were repeated up to 5 times in order to infiltrate a desired amount of nanoparticles into the samples.

A few comments should be made here regarding the freezing process used. In the initial fabrication tests, the liquid-filled samples after infiltration were allowed to air dry before sintering. This created two problems. First, a significant amount of suspension (and hence nanoparticles) would flow out of the sample during the drying. Second, and most importantly, because evaporation of the liquid occurred from the boundaries of the sample (i.e., faces and edges), there was a net flow of liquid to these boundaries during the drying. This resulted in a very non-uniform distribution of nanoparticles, with the micron-sized pores of the scaffold near the boundaries being completely filled while those in the center of the sample being nearly devoid of nanoparticles. This high concentration of nanoparticles near the boundaries significantly reduced the effectiveness of additional infiltration steps. Immersing the samples into liquid nitrogen followed by vacuum drying overcame both of these issues. (It should be mentioned, however, that the ability to have the infiltrated nanoparticles concentrated near the faces and edges of the samples could be useful in specific applications.)

Another benefit of this freeze-drying is that a secondary structure is created in the infiltrated nanoparticles by the growing ice crystals. This 'mesoscale' porosity could be an advantage in a membrane separation application, as it could facilitate the transport of water through the structure.

7.1.4 Characterization

The absolute densities of the samples were measured by a pycnometer (AccuPyc 1330, Micromeritics, Norcross, GA). The porous microstructures of the infiltrated composites were observed using a field emission scanning electron microscope (SEM, LEO1550, Carl Zeiss MicroImaging Inc., Thornwood, NY). A 3 nm Au-Pt layer coating was applied before the examination. Images were taken from the cross-sections of the samples, which were obtained by breaking the samples by hand. Nitrogen adsorption measurement was carried out by a BET instrument (Autosorb-1 C, Quantachrome Instruments, Boynton Beach, FL) to determine the specific surface area of the samples. Equibiaxial flexural strength measurements were carried out following ASTM C 1499.[146] Details of the apparatus and procedure used for these strength measurements are provided in Chapter 3.

Because use of these materials as a liquid separation membrane is one possible application, a set of water flux measurements were also conducted. To perform the tests, samples were first masked with an alumina foil, leaving a round area with a known diameter in the middle of the sample face. Afterwards, deionized water was applied to the samples under a fixed differential pressure (30, 40, and 50 kPa) in a sealed system. The water that passed through the samples in a specified time period was collected and weighed, allowing calculation of the water flux rate (volume/time-area) and permeability (volume/time-area-thickness-pressure). To investigate possible damage to the morphology of the samples caused by the flux tests, a set of samples used in the tests were re-examined using SEM and nitrogen adsorption.

7.2 Results and discussion

7.2.1 Porous Microstructure

The cross-sectional microstructures infiltrated with 22 nm nanoparticles are shown in Fig 7-2. Due to the disk-like scaffold geometry, the thermal gradient in the axial direction during immersion into liquid nitrogen is much higher than that in the radial direction. As a result, a pronounced directional order is observed in the structure of the infiltrated nanoparticles after the first infiltration step (Fig. 7-2a). However, because this secondary porous structure forms within the pores of the scaffold, the directional growth of the ice crystals is blocked by the scaffold framework. Nonetheless, the composite is still quite porous and thus additional infiltration steps are possible.

Shown in Fig. 7-2b is the microstructure after three infiltration steps, from which several observations can be made. First, the nanoparticle content has substantially increased, meaning that the micron-scales pores in the original scaffold are nearly completely filled. Second, the degree of directional order observed after one infiltration step is significantly reduced. This is because the directional growth of the growing ice is distorted by the existing structures and the ice thus grows more randomly. Third, the surfaces of the original scaffold are now fully covered by the adsorbed nanoparticles (Fig. 7-2d). This provides a pure silica surface that can be easily functionalized for selected applications.

After five infiltration steps (Fig. 7-2c), the pores have become nearly completely filled with the infiltrated nanoparticles. Nonetheless, the porous structure of these nanoparticles is clearly visible.

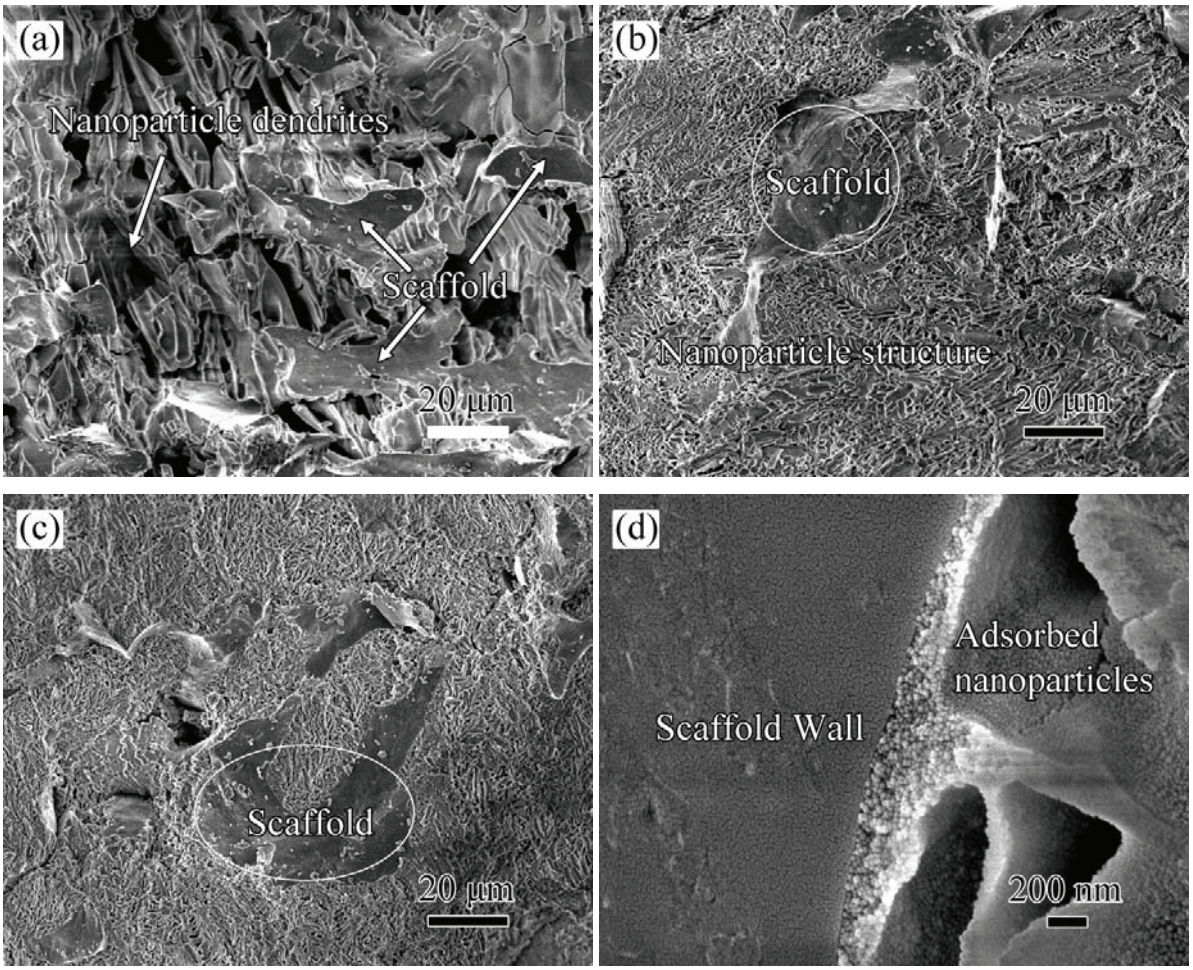

Fig. 7-2. The microstructures of scaffolds after 1 (a), 3 (b) and 5 (c) infiltrations with 22 nm nanoparticles, (d) High magnification image of the scaffold after 3 infiltration steps showing the scaffold-nanoparticle interface.

7.2.2 Specific Surface Area and Pore Size

Before presenting the measured specific surface areas, I first present a simple equation for predicting the effects of infiltration on this property. This equation would be useful, for example, in designing a composite with a desired specific surface area. The primary assumption

made is that the infiltrated nanoparticles experience only point-to-point contact such that their individual surface area is preserved during sintering.

On this basis, the specific surface area (S) of the fabricated nanocomposite is a function of the volume fraction of nanoparticles in the infiltrating suspension (c), nanoparticle diameter (d), and number of infiltration steps (n), and is given by

$$S_n = \frac{S_{scaffold}\rho_{scaffold}V_{scaffold} + S_{nanoparticle}\rho_{nanoparticle}V_n}{\rho_{scaffold}V_{scaffold} + \rho_{nanoparticle}V_n} \quad (1)$$

where ρ is density, and V is volume fraction. The subscripts denote either the specific component (i.e., scaffold or nanoparticle) or the number of infiltration steps (e.g., S_n denotes the specific surface area of the sample after n step infiltration steps). The specific surface area of the scaffold ($S_{scaffold}$) is below the detection limit of the BET instrument and is assumed to be 0.1 m^2/g based on a rough approximation made using the measured pore sizes (20 ~ 50 μm). The densities of the scaffold ($\rho_{scaffold}$) and nanoparticles ($\rho_{nanoparticle}$) are 2.49 g/cm^3 (measured by a pycnometer) and 2.37 g/cm^3, respectively. The volume fraction of the scaffold ($V_{scaffold}$) was determined in Chapter 5 as ~0.3. The specific surface area of the nanoparticles was calculated by their diameter (d) and density based on the relationship $S_{nanoparticle} = 6/(d\cdot\rho_{nanoparticle})$, which was confirmed by BET measurement (115 m^2/g for 22 nm nanoparticles, 211 m^2/g for 12 nm nanoparticles). The volume fraction of the nanoparticles after n step infiltration is $V_n = V_{n-1}+(V_{pore}-V_{n-1})\cdot c$, where n = 1, 2, 3, 4, or 5 and $V_0 = 0$.

The theoretical specific surface area of the nanocomposites after n suspension infiltrations with different sized nanoparticles is shown in Fig. 7- 3 (dashed lines). It is clear that the specific surface area of the composites can be dramatically increased, up to hundreds of square meters per gram in this system. As expected, smaller nanoparticles produce higher specific surface areas.

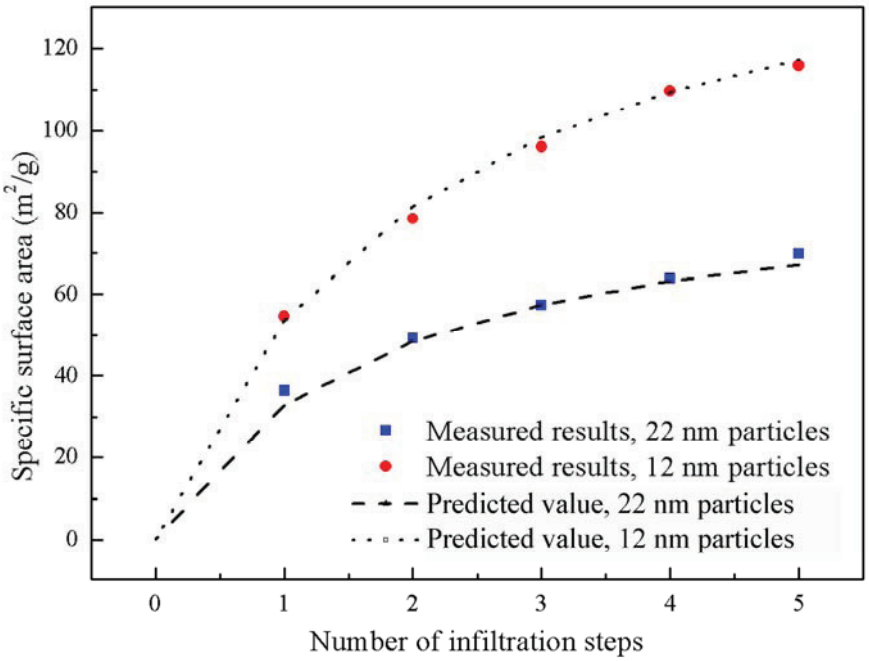

Fig. 7-3. Predicted and measured specific surface area of the composites versus the number of infiltration steps.

Also shown in Fig. 7-3 are the measured specific surface areas versus number of infiltration steps for both 12 and 22 nm nanoparticles. As seen, the agreement between theory and experiment is extremely good, supporting the validity of the assumption about point-to-point contact of the nanoparticles. It is also clear that while the specific surface area continues to increase with each infiltration step, the increases becomes smaller each time. This is because each infiltration step reduces the amount of free volume available in the sample, meaning that fewer nanoparticles are able to enter the sample during subsequent infiltrations.

The distribution of pore sizes, obtained from the BET measurements, for the samples after 1, 3 and 5 infiltrations with 22 nm nanoparticles is shown in Fig. 7-4. Note that the micron-sized pores of the scaffold are not detected in these measurements. As seen, after one infiltration, a pore size of approximately 11 nm is observed. After the 3rd and 5th infiltrations, a binary distribution of pore sizes develops, with peaks at approximately 4 and 9 nm. The reason for this binary distribution is not understood at this time. However, the fact that it is not seen after only one infiltration suggests that it is somehow caused by repeated freeze drying and

sintering of the infiltrated nanoparticles. It is possible that repeated sintering shrinks some of the pores formed during the early infiltration process.

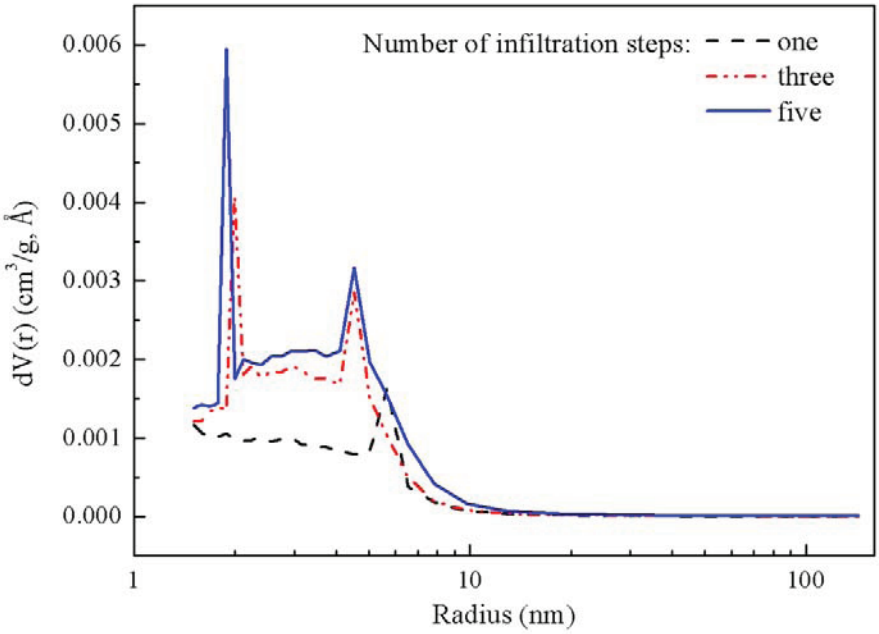

Fig. 7-4. Pore size distributions of the composites after 1, 3 and 5 infiltration steps with 22 nm nanoparticles.

7.2.3 Strength

The measured flexural strength of the scaffolds as a function of the number of infiltration steps is shown in Fig. 7-5. Two observations can be made. First, the strength of the scaffold increases steadily after each infiltration step. Even though the strength is mainly provided by the scaffold (i.e., the strength with no infiltrated nanoparticles forms the bulk of the sample strength), the secondary porous structure clearly contributes. Second, the flexural strength increases slowly after the first two infiltrations, rapidly increases after the third infiltration, and then increases more gradually again. One possible explanation for this jump can be gained from the SEM images of the microstructure, shown as inserts in Fig. 7-5. After two infiltration steps (left insert), large pores are clearly visible in the structure of the infiltrated nanoparticles. After three infiltrations (right insert), however, these pores are no longer visible. I hypothesize that for the particular materials and suspension concentrations used here, a connected network of

nanoparticles is established inside the pores of the scaffold after three infiltrations (i.e., the network of nanoparticles spans the pore spaces of the scaffold). After this point, further infiltrations reinforce and strengthen this network.

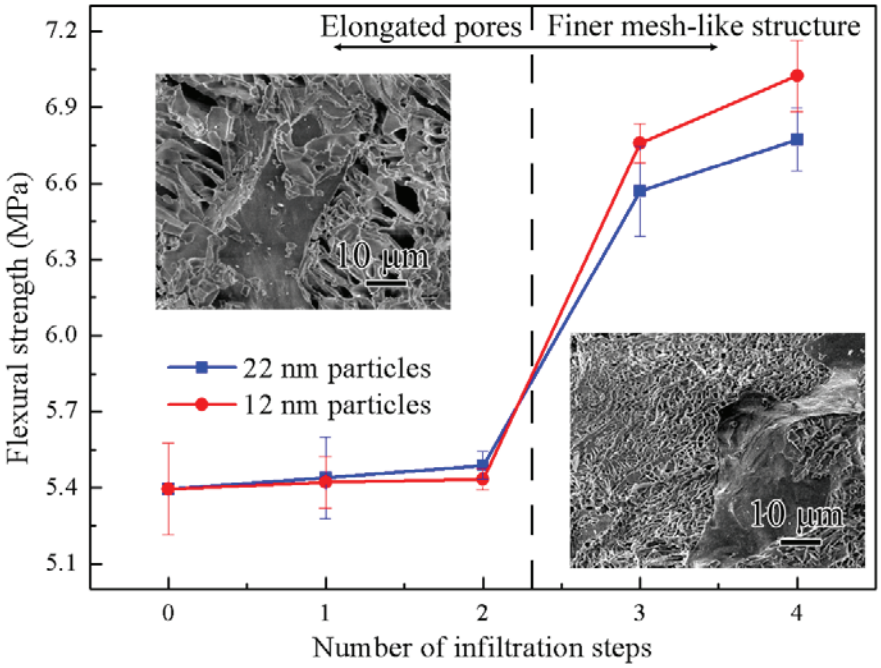

Fig. 7-5. Strength evolution with the infiltration steps with 12 and 22 nm particles. The inserted images display the cross-sectional microstructures of the scaffolds infiltrated with the 22 nm nanoparticles after two (upper left) and three (lower right) infiltration steps.

7.2.4 Permeability

One of the potential applications of these composites created here is as liquid membranes (e.g., removing suspended solutes from water). To test the feasibility of such an application, I performed some simple tests to determine whether water could be made to pass through one of the samples under an applied differential pressure.

The results of these tests are shown in Fig. 7-6. Shown in Fig. 7-6a are the measured flux rates versus the number of infiltration steps with 22 nm nanoparticles at applied differential pressures of 30, 40 and 50 kPa. As seen, the flux rates decrease almost linearly for the first three infiltrations as the micron-scale pores in the scaffold fill with nanoparticles. After the 3rd

infiltration, the flux rate again decreases for all three applied differential pressures, though the decrease is noticeably smaller. This suggests that the pore of the scaffold have become nearly full (roughly consistent with the strength results presented in Fig. 7-5).

Dividing these flux rates by the applied pressure and membrane thickness gives the permeability of the sample, which is plotted in Fig. 7-6b for experiments made using both 12 and 22 nm nanoparticles. As seen, the flux rates at the various different pressures all collapse to a single value for each number of infiltration steps, verifying the expected proportionality between flux and differential pressure. In addition, the permeabilities obtained using both 12 and 22 nm nanoparticles are very similar over the first three infiltration steps but differ by a factor of approximately three after the fourth infiltration step.

It should be mentioned that five different flux measurements were made on each sample, and error bars corresponding to the standard deviation of these measurements are actually plotted on the graphs (for all plots). However, the variability was so small that the error bars are actually hidden by the symbols used in the graphs.

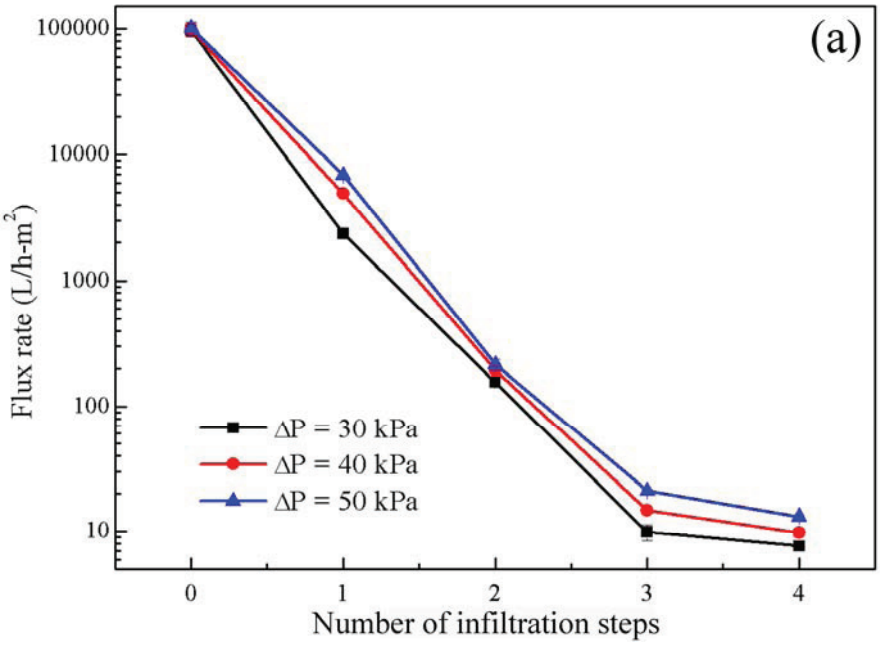

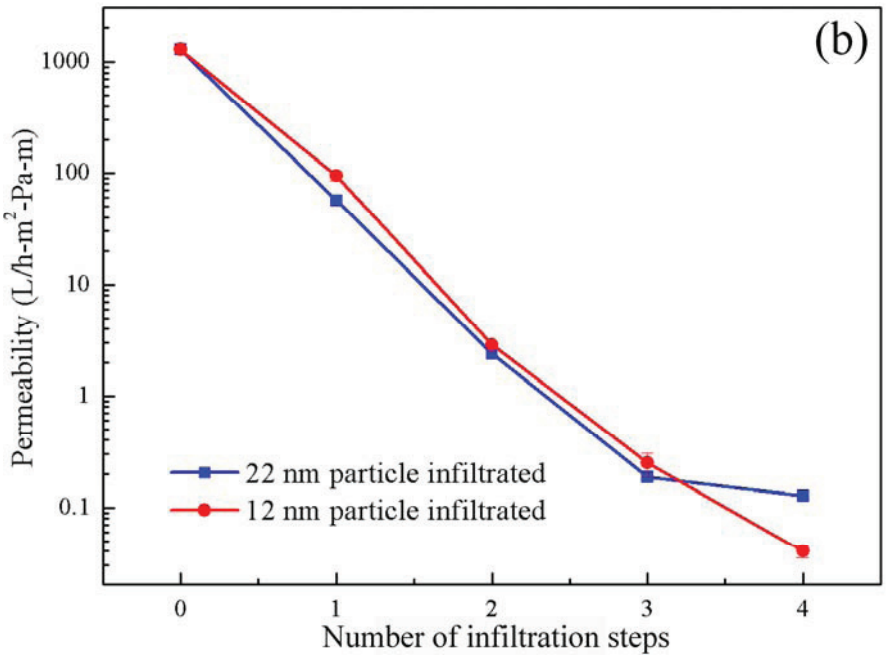

Fig. 7-6. Flux rates and permeabilities versus number of infiltration steps: (a) flux data at various differential pressures upon infiltrating 22 nm nanoparticles, and (b) permeability results with both 12 and 22 nm nanoparticles.

The permeability of these samples after three infiltration steps is of order 0.1 L/s-m^2-Pa-m), and as shown in Fig. 7-3, the specific surface area after three infiltrations is approximately 60 m^2/g for 22 nm particles and 100 m^2/g for 12 nm particles. These values are comparable or even better than those of commercially-available membranes. For example, Wiesner *et al.* report a permeability of 0.18 L/s-m^2-Pa-m for alumina anodisc membranes (0.2 μm pore size),[159] while Majouli *et al.* report a permeability of 0.19 L/s-m^2-Pa-m for an alumina membrane (0.2 μm pore size).[160] Regarding specific surface area, a measurement performed in my laboratory on a commercial alumina membrane yielded a value of 20.2 m^2/g (0.2 μm pore size, Anodisc, Whatman). Work on optimizing the structure of these membranes would likely result in significant improvement in the properties.

7.2.5 Integrity

The final characterization test performed was the integrity of the composites. The specific issue was to determine whether the infiltrated nanoparticles were disturbed by the flux tests.

Shown in Fig. 7-7 are SEM images taken after the flux tests on scaffolds that had undergone one (Fig. 7-7a) and three (Fig. 7-7b) infiltration steps. The pore structure is seen to be very similar to that found prior to the flux tests (Fig. 7-2). It should be mentioned that the cracks in the secondary microstructures (indicated by the circles) are caused when breaking the samples by hand to obtain the fracture surfaces and not created by the passing water. (Similar cracks are also evident in the samples that had not been used in the flux tests, shown in Fig. 7-2.)

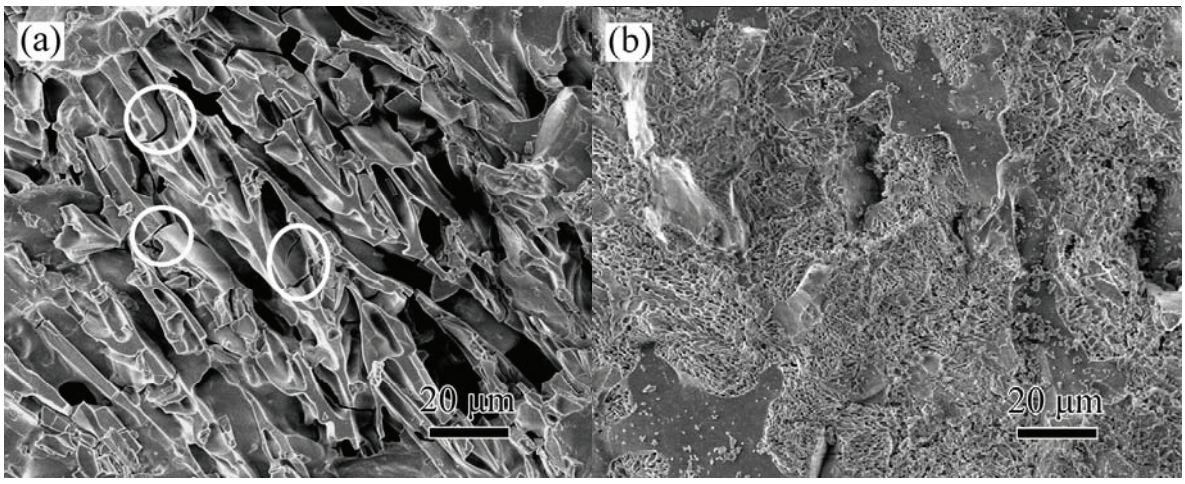

Fig. 7-7. Microstructures of 22 nm particle infiltrated scaffolds after water flux test with one (a) and three (b) infiltration steps. The circles indicate cracks formed when breaking the samples.

BET measurements to determine the specific surface area of the composites were also performed on the samples after the flux tests and the results for both the 12 and 22 nm nanoparticles are shown in Fig. 7-8. As seen, no significant change in the specific surface area is observed for any of the samples tested.

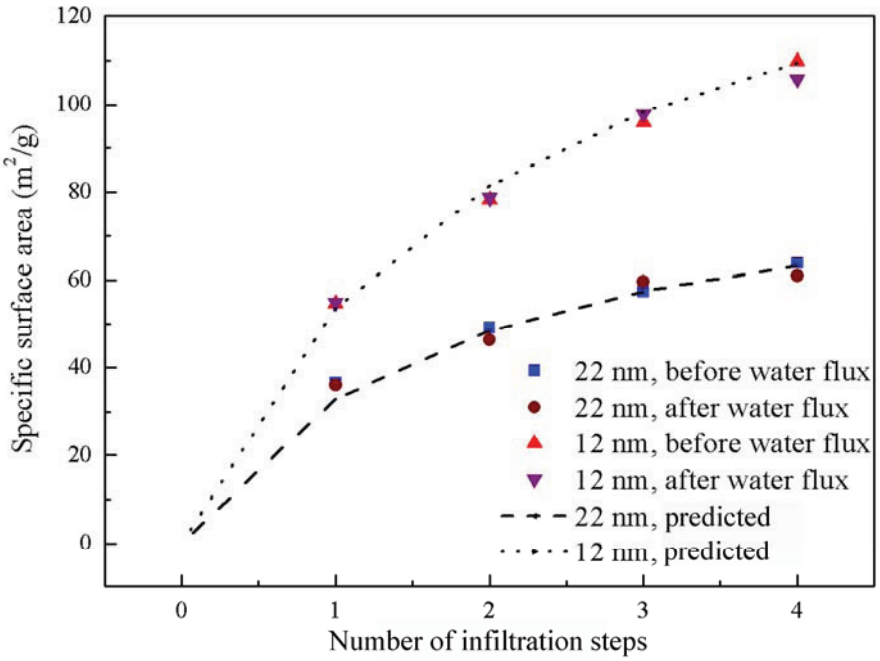

Fig. 7-8. Specific surface area versus number of infiltration steps for the samples after the flux test.

Finally, the results of flexural strength tests performed on samples after the flux tests are shown in Fig. 7-9. Again, no significant change is observed upon comparing these results to those obtained on samples that had not been used in the flux tests.

In summary, these tests confirm that the simple water flux tests performed here cause no significant change in the structure or properties of the infiltrated composites.

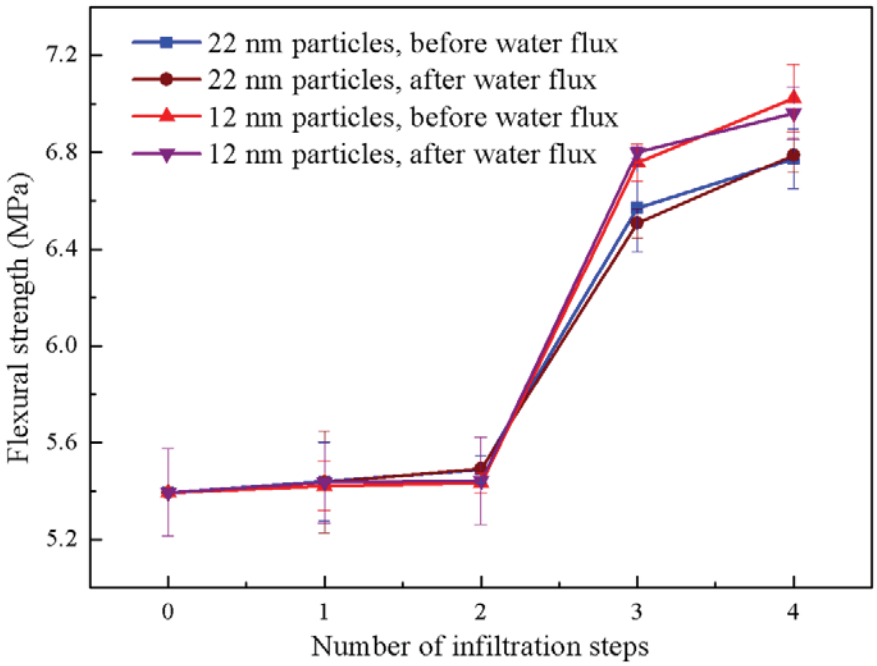

Fig. 7-9. Strengths before and after the water flux test versus number of infiltration steps for the 12 and 22 nm nanoparticles.

7.3 Conclusions

I have described a novel method for creating high surface area, porous ceramic composites without loss of mechanical strength. The infiltration method is simple and inexpensive, and by altering the size and concentration of nanoparticles infiltrated, the pore size and specific surface area of the resulting composites can be precisely controlled.

Simple water flux tests demonstrated the potential use of these materials as liquid membranes. Although not studied, by altering the infiltration procedure, it should allow selectively depositing nanoparticles in only a thin, 'active' layer near one boundary of the scaffold. In this way, the majority of the scaffold structure would simply provide the mechanical strength of the membrane without altering its permeability (i.e., the permeability would be controlled by the active layer).

One of the attractive features of this method is that it could be widely applied to a range of starting frameworks. Infiltrating different types of particles (different size, materials, etc.) would be relatively straightforward.

CHAPTER 8. EFFECTS OF ROD-LIKE PARTICLES ON THE MICROSTRUCTURE AND STRENGTH OF FREEZE CAST POROUS SILICA NANOPARTICLE COMPOSITES*

Abstract

This chapter describes the results of an investigation into the effects of the addition of rod-like silica nanoparticles on the properties of freeze-cast green bodies formed from silica nanospheres. Rod-like silica particles with ~220 nm diameter and tunable aspect ratio from ~1 to ~12 (length/diameter) were prepared and added to aqueous suspensions containing 22 nm spherical silica particles. After freeze-casting, porous composites were created with all aspect ratio rods, which is shown to be consistent with the results of a simple analysis in which the experimental freezing rate is compared to the critical rate at which the dispersed particles can no longer be expelled from the growing ice front. In addition, the pores with rods of aspect ratio one (i.e., near-spheres) were smoother and more spherical. Finally, it was found that the rod-like particles improve the flexural strength of the composites and this strengthening effect intensifies with increasing aspect ratio. This study provides a strategy for fabricating porous materials of improved properties and performance without compromising the porosity or changing the material composition.

8.1 Experimental procedure

8.1.1 Materials

The silica nanorods were synthesized with the method of Kuijk *et al*. [31] using 1-pentanol (≥99%), polyvinylpyrrolidone (PVP, average molecular weight M_n=40.000), absolute ethanol, sodium citrate dihydrate (99%), ammonia (25 wt% in water), and tetra-ethyl orthosilicate (TEOS). These chemicals were purchased from Sigma-Aldrich and were used as received. In addition, 34 wt% silica colloidal suspension (Ludox TMA, Sigma-Aldrich, St. Louis, MI), sodium chloride (NaCl, AR grade, Mallinckrodt, Paris, KY), and de-ionized water were mixed

* Chapter 8 has been submitted to *Journal of the American Ceramic Society*

together with the nanorods to form the solutions to be freeze cast. The silica nanospheres in the Ludox suspension had a nominal diameter of 22 nm (manufacturer reported), a density of 2.37 g/cm^3,[144, 145] and were well-dispersed in de-ionized water.

8.1.2 Preparation of rod-like silica particles with tunable aspect ratio

Following the method of Kuijk *et al.*, rod-like silica particles with tunable aspect ratio were prepared by a one-pot synthesis method.[31] PVP was firstly dispersed in 1-pentanol with a ratio of 0.1 g/mL, and the mixture was kept overnight and then ultra-sonicated for 30 min to ensure the dissolution of PVP. Afterwards absolute ethanol, de-ionized water and 0.18 M sodium citrate dehydrate solution were added to the PVP/1-pentanol solution in volume ratios (relative to the volume of 1-pentanol) of 1:10, 0.28:10 and 0.1:10, respectively, followed by manual shaking. A specific amount of an ammonia solution (25 wt% ammonia in water) was then added to the solution in volume ratios (relative to the initial volume of 1-pentanol) ranging between 0.1:10 to 0.5:10 and the mixture was shaken again. (As described elsewhere, the amount of added ammonia determines the resulting aspect ratio of the rods.) After an injection of TEOS (0.1:10 volume ratio relative to 1-pentanol) and a third shaking, the emulsion was kept overnight (~ 17 h) for nucleation and growth of particles. Every 10 mL of 1-pentanol produces approximately 0.017 g silica particles, and this procedure was repeated to synthesize enough particles for fabricating the porous silica composites.

The prepared silica particles were then isolated from the suspension using cetrifugation at 1500 *g* for 1 h, and were washed 2 times with ethanol, 2 times with de-ionized water and each time centrifuged at 1500 *g* for 15 min. To improve the size distribution, the particles were further washed 2 times with ethanol and centrifuged at 700 *g* for 15 min. The as-prepared silica particles were then dried and stored for use.

8.1.3 Freeze-casting of the composite

In a 10 mL vial, a specific amount of prepared silica nanorods was dispersed in a solution containing Ludox and de-ionized water. The suspension was ultra-sonicated for 2 h and shaken with a rotator overnight. Next, a desired amount of NaCl was added into the vial (the NaCl concentration in the suspension was kept at 0.5 M). This salt addition was used to screen the

electrostatic forces between the particles, which allowed bonding of the nanoparticles and improved both the homogeneity of the suspensions and the resulting porous composites. After mixing, the suspension was transferred into silicone rubber molds (31 mm diameter, 2 mm deep). Along with the molds, the suspensions were placed in an Advantage Freeze Dryer (SP Industries VirTis, Gardiner, NY) immediately for freezing and sublimation. Samples were frozen at -35°C and ~1.34 Pa for 400 min with a cooling rate of 2°C/min. The freeze-cast porous green composites were de-molded and stored for further use.

8.1.4 Characterization

The morphology of the silica nanorods and the microstructure of the freeze-cast porous composites were examined by field emission scanning electron microscopy (SEM, LEO1550, Carl Zeiss MicroImaging Inc., Thornwood, NY), with a 3 nm Au-Pt layer coating applied before imaging. The images of the porous composites were taken from the cross-sections, which were obtained by breaking the sample by hand. The absolute density of the silica nanorods was measured by a pycnometer (AccuPyc 1330, Micromeritics, Norcross, GA). X-ray diffraction (X'Pert PRO diffractometer, PANalytical B.V., EA Almelo, The Netherlands) was performed to identify the crystallinity of the silica nanorods.

The equibiaxial flexural strength measurements were carried out following ASTM C 1499,[146] the details have been discussed in Chapter 3. The equibiaxial flexural strength and the Poisson's ratios for each porous composite (ν_p) were calculated following Eq. 3-1 and Eq. 3-3. Poisson's ratio for pore-free silica was given as 0.17 by Ledbetter et al.[161]

8.2 Results

8.2.1 Properties of the silica nanorods

Fig. 8-1 displays the morphologies of the prepared silica nanorods. The anisotropic growth of the silica can be either promoted or hindered by controlling the concentration of ammonia. (The proposed growth mechanisms were discussed by Kuijk *et al.*[31]) In this study, ammonia injections (25 wt% in water) were introduced into the solution in volume ratios (relative to the initial volume of 1-pentanol) ranging between 0.1:10 to 0.5:10 to obtain silica particles with aspect ratios from 12 (Fig. 8-1a) to 1 (Fig. 8-1c). The one dimensional growth of

the silica particles is favored by lowering the ammonia amount, and the prepared rod-like particles are bullet-shaped with one end rounded and the other flat (visible in Fig. 8-1b). When the amount of ammonia is increased up to or above a ratio of 0.5:10, the anisotropic growth of silica particles is inhibited and the rod-like particles are reduced to nearly spherical particles (Fig. 8-1c). All the rod-like particles share a similar diameter, ~220 nm, regardless of the length differences. The average diameter of the spheres is slightly larger, ~280 nm. Even though there are still size distributions in both the length and the diameter of particles, the difference is minor considering the major morphology differences among the samples. This consistency of the diameters among the synthesized rods/spheres simplifies the variables in the composites and facilitates the study of the properties of the freeze cast porous materials.

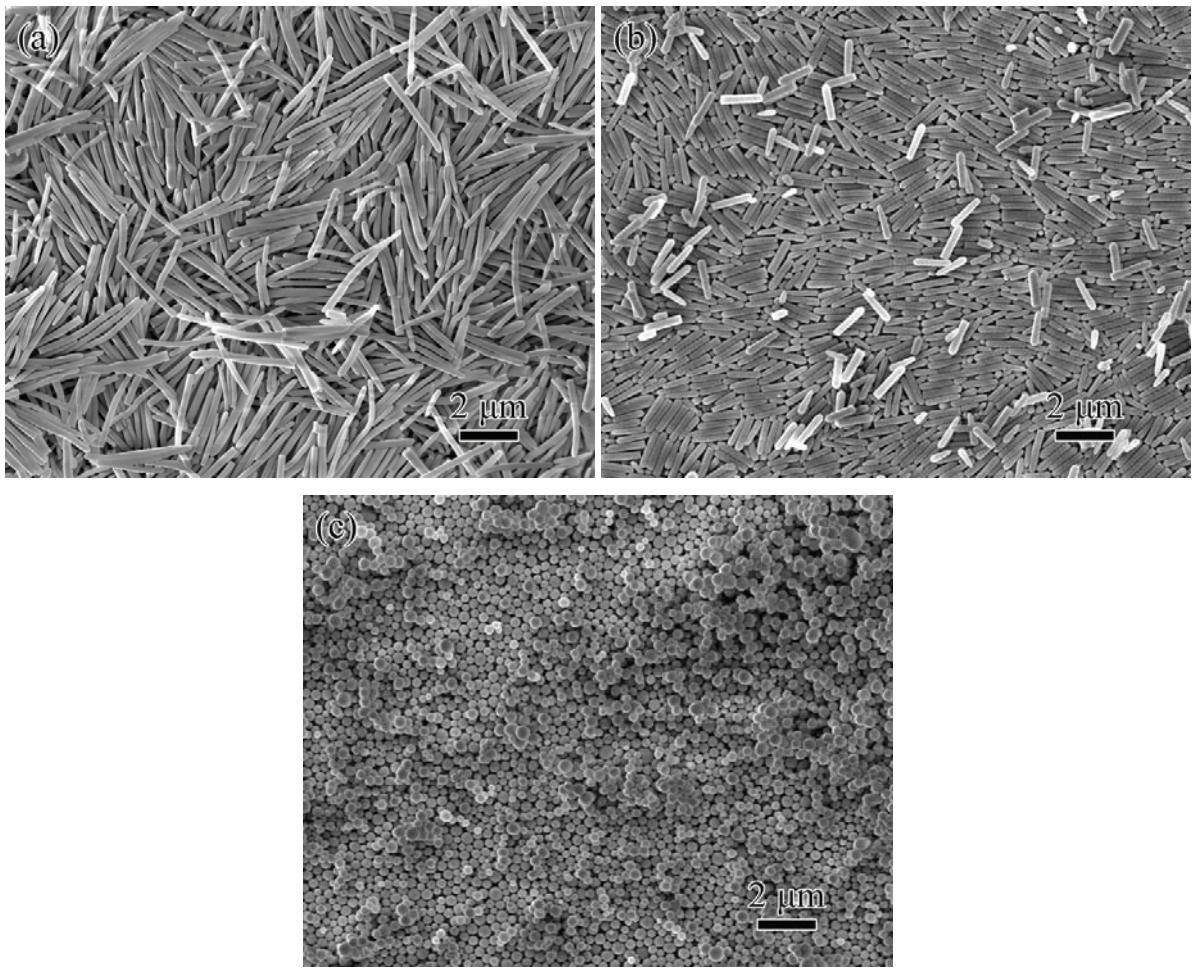

Fig. 8-1. SEM images of the synthesized silica particles with different aspect ratio: (a) ~12, (b) ~4.5, (c) ~1.

The density of the silica nanorods was directly measured by a pycnometer and found to be approximately 2.1 g/cm^3, which was used to determine the amount of the silica nanorods needed to make samples with specific compositions. The XRD examinations indicate that both the silica nanorods and the Ludox silica nanospheres are amorphous.

8.2.2 Determination of the appropriate concentration of nanorods and nanospheres

In order to maintain the stability of the suspension and the corresponding uniformity of the porous composites, the total silica loading in this work was fixed at 18 vol%. Solids loadings higher than this value resulted in rapid sol-to-gel transition that made it difficult to mold the sample (especially for long rods). Suspensions containing silica loading below 18 vol% had low viscosities that allowed larger particles to rapidly settle.

Since the purpose of this study was to investigate the particle morphology effects (namely the aspect ratio of the silica nanorods) on the properties of the porous composite, the composition of the studied composites was chosen such that silica nanospheres provide roughly monolayer coverage of the larger nanorods. If silica nanospheres are assumed to arrange in a hexagonal close-pack structure on the nanorods, the area that each nanosphere occupies is $\sqrt{3}D^2/2$ (D is the diameter of the silica nanospheres, 22 nm). A simple balance of surface area on the rods yields

$$\frac{3\sqrt{3}(V - V_{nanorods})}{\pi D} = S_{nanorods}\rho_{nanorods}V_{nanorods} \tag{8-1}$$

where V is the total silica loading (18 vol%), $S_{nanorods}$ is the specific surface area of the nanorods (10.51 m^2/g for rods with aspect ratio of 12, 11.44 m^2/g for spheres), $\rho_{nanorods}$ is the density of the silica nanorods (2.1 g/cm^3). The calculation suggests that this condition should involve ~14 vol% nanorods plus ~4 vol% nanospheres. However, experimental observations indicate that 4 vol% nanospheres is not sufficient for full coverage of the rods. As shown in Fig. 8-2a, the rods in the composite with 6 vol% nanoparticles still have patches of uncovered surfaces (circled areas). One possible explanation is that some aggregation of the nanospheres occurs upon the addition of NaCl. Further exploration of the microstructure with different compositions showed that in samples containing 10 vol% nanorods and 8 vol% nanospheres the rods were covered fairly

uniformly with the nanospheres (Fig. 8-2b). Subsequently, all composites in this study contained 18 vol% total solids loading with 10 vol% nanorods and 8 vol% nanospheres.

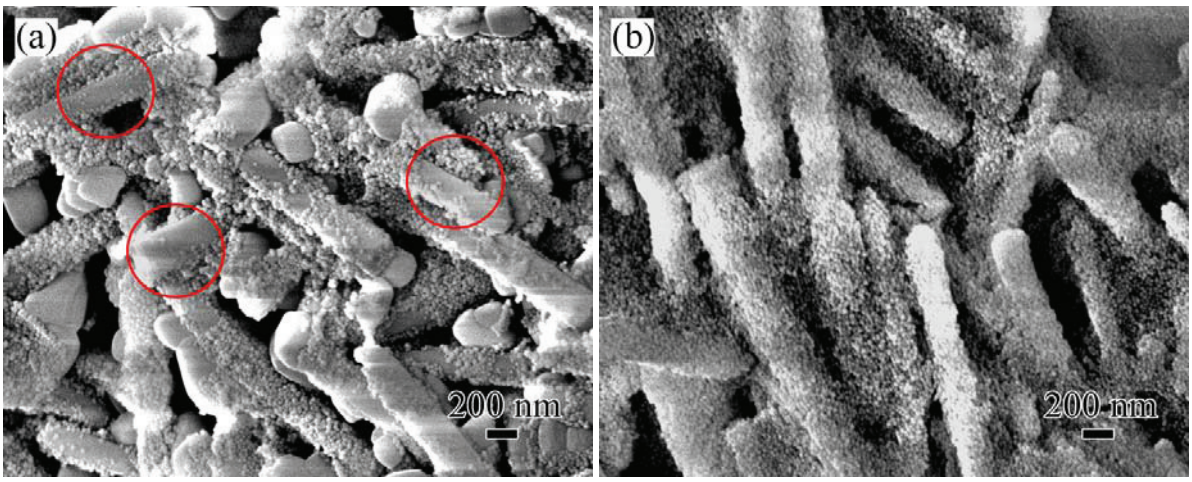

Fig. 8-2. SEM images taken on a freeze-dried composite containing: (a) 12 vol% nanorods of aspect ratio 12 plus 6 vol% silica nanospheres, (b) 10 vol% nanorods of aspect ratio 12 plus 8 vol% silica nanospheres. The circles indicate portions of the rods that are not covered by the nanospheres.

8.2.3 Porous microstructure of the composites

One of the most significant effects of particle morphology (e.g., aspect ratio in this chapter) is modifying the porous microstructure of the freeze-cast composite. In freeze casting, the suspension is frozen to a solid state and afterwards the ice crystals are removed through sublimation. If the dispersed particles are expelled from the ice front, then the porous structure should replicate the morphology of the ice crystals. Assuming the thermal gradient in the sample during freezing is low (i.e. thin samples and low freezing rate), the suspension should experience homogeneous freeze casting, such that ice crystals grow randomly without preferred orientation.

Fig. 8-3 shows the microstructure of the composite consisting of 10 vol% silica nanorods with aspect ratio α = 1 and 8 vol% silica nanospheres. The primary pores are spherical with an average pore size of approximately 30 μm. At a larger magnification (Fig. 8-3c), the pore wall is found to consist of tightly packed spheres and the walls of the pores are relatively smooth.

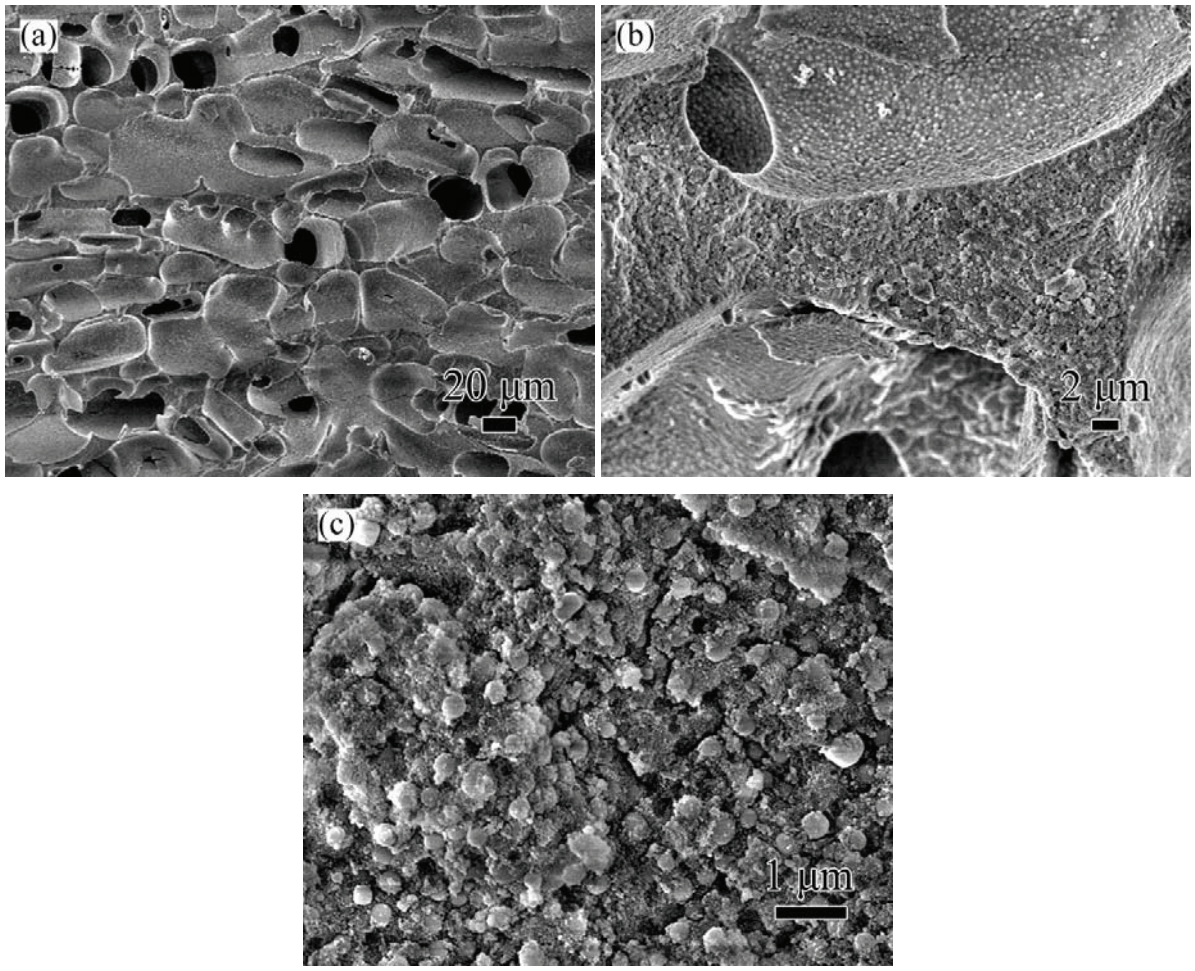

Fig. 8-3. SEM images of the freeze-cast silica composites with rods at aspect ratio 1: (a) 500x, (b) 5kx, (c) 25kx.

The porous microstructure changes as the aspect ratio of the nanorods increases. SEM images of a silica composite with 10 vol% nanorods of aspect ratio ~4.5 and 8 vol% nanospheres are shown in Fig. 8-4. Compared to Fig. 8-3, the pores are irregular shaped with a larger distribution in size (ranging from 20 μm to 100 μm). The large flat faces consist of rods and nanoparticles (Fig. 8-3c) arranged randomly and the pore walls are rougher than those in Fig. 8-3.

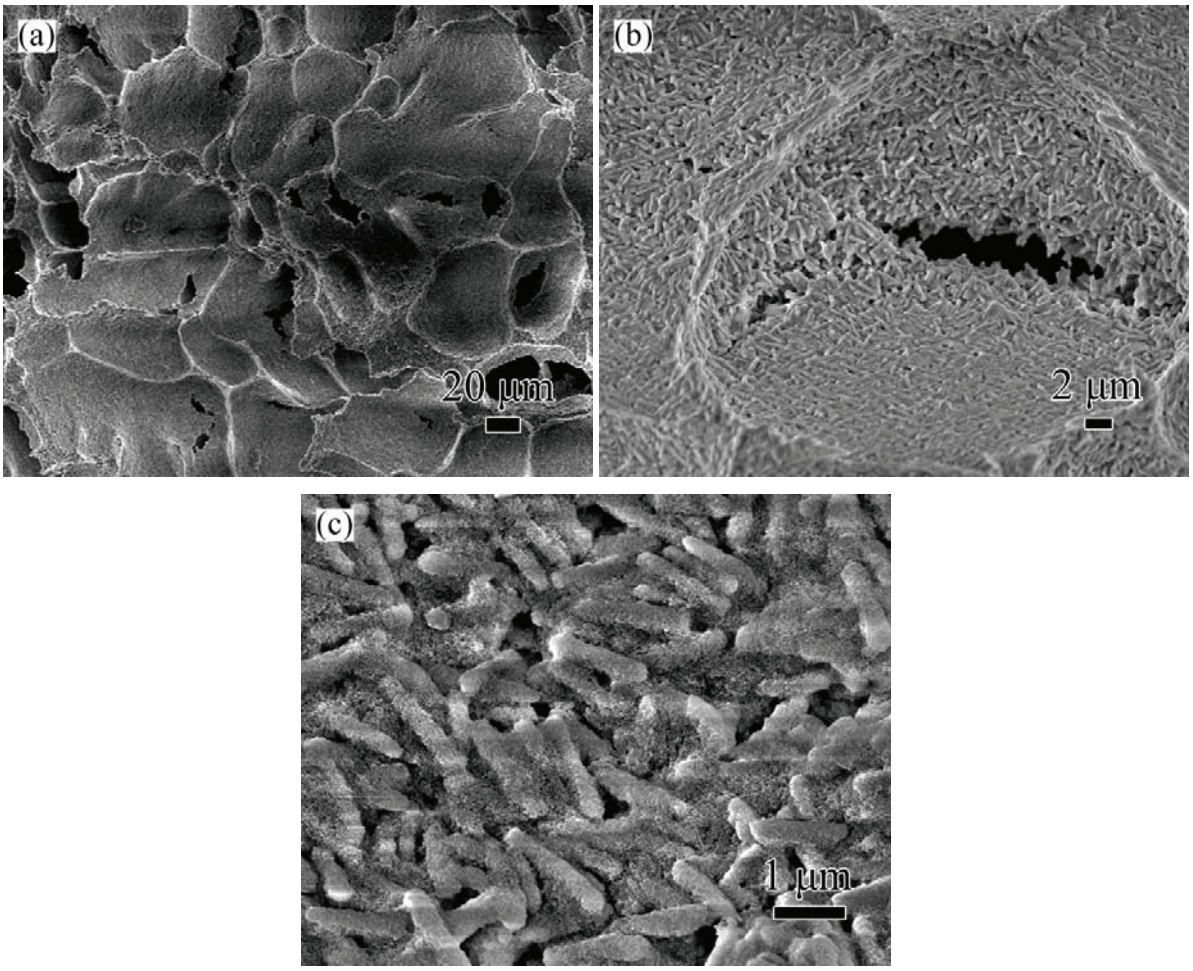

Fig. 8-4. SEM images of the freeze-cast silica composites with rods at aspect ratio ~4.5: (a) 500x, (b) 5kx, (c) 25kx.

Upon increasing the aspect ratio of the rods to 12 (Fig. 8-5), the pores again display an elongated shape, the characteristic sizes of the pores range from ~20 μm to ~40 μm (roughly same as the composites made with nanorods of aspect ratio ~1 (Fig. 8-3a), but somewhat smaller than those made with nanorods of aspect ratio ~4.5 (Fig. 8-4a)). In addition, as seen in Fig. 8-5b, the walls of the pores become noticeably rougher and consist of loosely packed rods and nanospheres (Fig. 8-5c).

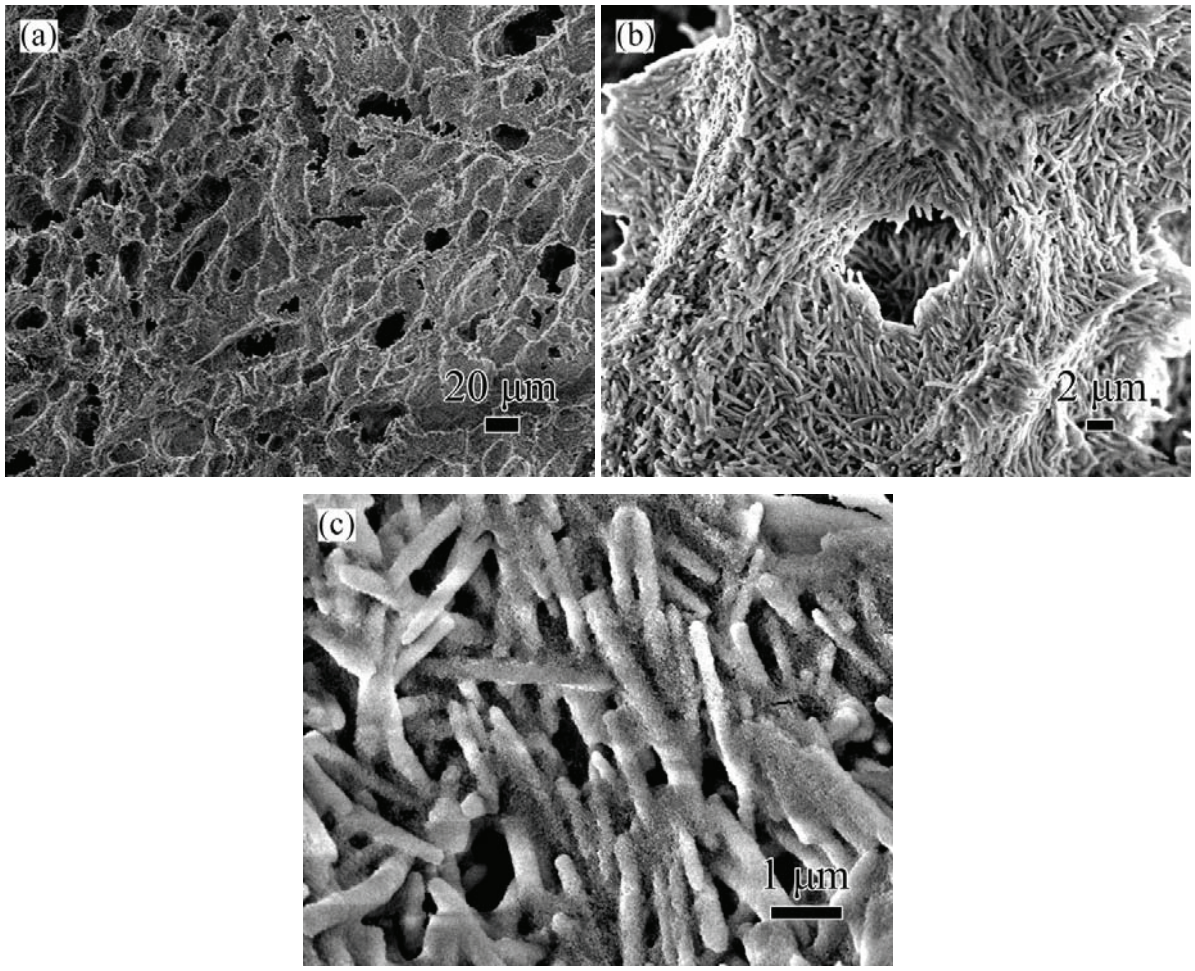

Fig. 8-5. SEM images of the freeze-cast silica composites with rods at aspect ratio ~12: (a) 500x, (b) 5kx, (c) 25kx.

A summary of the observations on the microstructure with the different aspect ratio rods is given in Table 8-1.

Table 8-1. Trends observed in SEM images of the silica composite microstructures.

Composition: 8 vol% nanospheres plus 10 vol% nanorods			
Property	$\alpha = 1$	$\alpha = 4.5$	$\alpha = 12$
Pore morphology	Spherical	Irregular	Elongated
Pore size	~30 μm	20 μm to 100 μm	20 μm to 40 μm
Particle packing in pore walls	Close packed	Well packed but with open voids	Loosely packed
Nature of pore wall	Smooth	Rough	Rough

8.2.4 Mechanical strength of composites

One benefit provided by the rod addition is improvement of the mechanical strength of the composites. The flexural strength results are shown in Fig. 8-6. It is remarkable that the flexural strength increases continuously with the increase of the rod aspect ratio. Specifically, as the aspect ratio increases from 1 to 12, the flexural strength increases from 0.07 MPa to 0.41 MPa – roughly a factor of six.

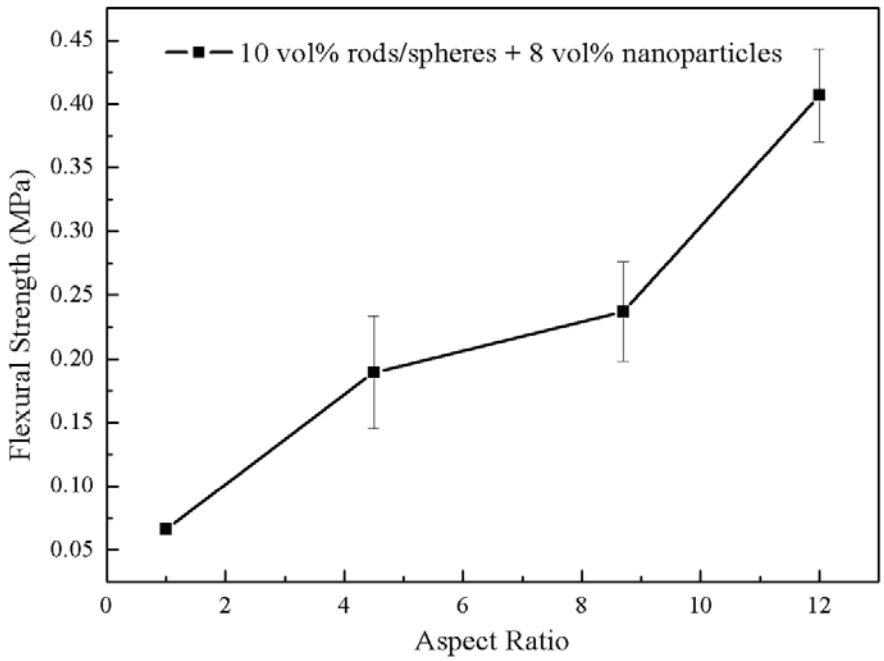

Fig. 8-6. Flexural strength of the freeze-cast porous silica composite as a function of the aspect ratio of the added rods.

8.3 Discussion

8.3.1 Formation of the porous microstructure

The porous microstructure of freeze-cast materials is formed primarily during the actual freezing step. Although other processes, such as suspension preparation, can affect the structure, the interaction between the solidification front (growing crystals) and the dispersed particles is critical in determining the nature of the composite.

In order to form a porous material, there are three basic criteria that must be met.[11] First, the suspended particles must be dispelled from the solidification front. For particle repulsion to be favored thermodynamically, engulfment of the particles by the ice must produce an increase in the overall surface free energy, σ (or conversely, repulsion must decrease the overall surface free energy). The change in free energy upon engulfment of a particle in an ice crystal is given by

$$\Delta\sigma = \sigma_{sp} - \left(\sigma_{sl} + \sigma_{pl}\right) \tag{8-2}$$

where σ_{sp}, σ_{sl}, and σ_{pl} are the interfacial energies of the solid-particle, solid-liquid, and particle-liquid interfaces, respectively. Although values for each of these terms are not easy to find, especially for the solid-particle interface, typical values of $\Delta\sigma$ of 10^{-2} J/m^2 have been reported,[63, 87, 162] indicating that repulsion of the particles is favored thermodynamically.

The second criterion necessary to form a porous solid is that the solidification front must have a non-planar morphology, as illustrated in Fig. 8-7, as this will lead to redistribution of particles between solid ice crystals. (If the ice front were planar, then repulsion of the particles would simply result in all of the suspended particles being pushed to one side of the sample.) Experimental evidence has shown that a non-planar morphology is the norm, as suspended particles will typically cause a deformation of the moving ice front. Mechanisms explaining the cause of this deformation include Mullins-Sekerka instability[66] and differences in thermal conductivity between the fluid and suspended particle.[163, 164]

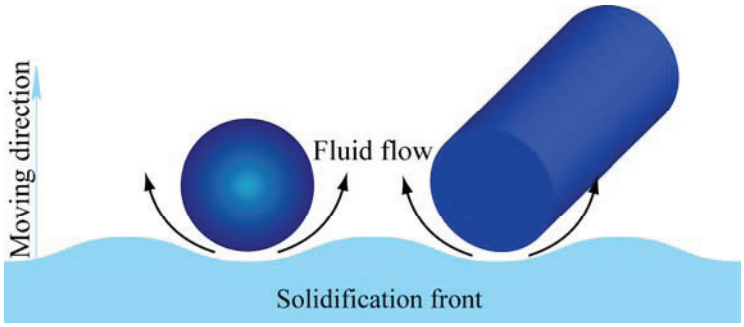

Fig. 8-7. Illustration of interaction between the solidification front and suspended particles.

The third criterion necessary for repulsion of the particles involves the kinetics of particle transport. Specifically, to be excluded, the rate at which particles are transferred away from the solidification front must be greater than the solidification velocity. The rate at which the particles are repelled is a balance between the disjoining pressure that is acting on the particles, which arises from differences in interfacial energies, and the hydrodynamic resistance experienced by the particles as they flow away from the solid ice crystals.

The following equation for the disjoining force acting on a spherical particle due to the differences in interfacial energies was provided by Korber et al.[63]

$$\left(F_{\sigma}\right)_{sphere} = 2\pi R\Delta\sigma\left(\frac{a_o}{d}\right)^n \tag{8-3}$$

where a_o is the intermolecular distance in the liquid, d is the thickness of the thin film between the particle and the ice front, and n is a constant ranging from 1 to 5. The intermolecular distance, a, is essentially the smallest thickness of the liquid film that can exist between the ice front and the particle. While accurate estimates of a and n are difficult to determine, Deville *et al.*[87] suggested that reasonable values would be a equal to 10^{-8} m and n equal to one.

For a spherical particle approaching a solid-fluid interface at velocity v, the drag force on the particle can be written as[63, 67, 87, 162, 165]

$$\left(F_D\right)_{sphere} = 6\pi\eta\frac{R^2}{d}v \tag{8-4}$$

where η denotes the viscosity of the liquid suspension, R is the radius of the spheres, and d again is the distance between the solidification front and the particle. It should be mentioned that for well-dispersed suspensions and small particles, the force of gravity can be ignored.

The critical velocity (v_c) of the solidification front, above which the particles will be engulfed, can be obtained by equating these two forces ($F_\sigma = F_D$), yielding

$$\left(v_c\right)_{sphere} = \frac{d}{3\eta R}\Delta\sigma\left(\frac{a}{d}\right)^n \tag{8-5}$$

To obtain a rough estimate of this critical velocity, the following values were inserted in this equation: $\Delta\sigma = 10^{-2}$ J/m^2, $a = 10^{-8}$ m, $\eta = 10^{-3}$ Pa-s (viscosity of liquid water), $n = 1$, and R equal to either 10^{-7} m or 10^{-8} m (approximately equal to the radii of the nanorods and nanospheres, respectively). The resulting critical velocity is of order 10^5 μm/s for the nanorods and 10^6 μm/s for the nanoparticles. By comparison, the solidification velocity in these experiments was estimated to be of order 10^{-1} μm/s, which was determined from observations of the time required to completely freeze the sample (approximately 50 min) and the half-thickness of the sample (1 mm). Thus based on this simple analysis, both the silica nanorods (with aspect ratio of 1) and the nanospheres should be effectively rejected from the ice front, as the actual freezing velocity is orders of magnitude lower than the critical velocity at which the forces balance. The large circular pores seen in Fig. 8-3a thus replicate the ice crystals formed during the freezing process. Because of the relatively low thermal gradient in the sample during freezing, the ice crystals are randomly oriented, yielding a homogenous freeze-cast composite.

The situation for rod-like particles is obviously more complicated because of the anisotropic shape and, not surprisingly, little prior work has been done on the expulsion of such particles. Fortunately, however, a rough analysis can be done with a few simple assumptions.

Because the disjoining force arises from differences in surface energies between phases, its magnitude is related to the surface area of the suspended particle. Through simple geometry, it can be shown that the ratio of the surface area of a rod to a sphere, both of equal radii, will be approximately equal to the aspect ratio, α. I can thus modify Eq. 8-3 as

$$\left(F_\sigma\right)_{rod} \sim 2\pi R\alpha\Delta\sigma\left(\frac{a}{d}\right)^n \tag{8-6}$$

Because of their anisotropic geometry, the hydrodynamic friction factor for a rod in the bulk depends on its direction of motion relative to the rod axis (e.g., parallel or normal to the rod axis). Doi and Edward[166] present equations for these two friction factors that only differ by a factor of two. Likewise, the correction factors for motion near a solid wall also depend on the direction of motion (relative to both the rod axis and the wall). Padding and Briels[167] present

equations for these corrections that all reduce to $2R/d$, where d is the closest distance between the rod and the wall when $d << 2R$ (i.e., near contact). Using these expressions, the following approximate equation for the drag force on a rod near a solid wall can be written:

$$\left(F_D\right)_{rod} \sim b4\pi\eta \frac{RL}{d\ln\left(L/2R\right)}v \tag{8-7}$$

where the constant b is equal to 1 for motion along the rod's axis and 2 for motion normal to the axis.

Equating Eqs. 8-6 and 8-7 yields the following approximate expression for the critical velocity for the rods

$$\left(v_c\right)_{rod} \sim \frac{\Delta\sigma\left(a/d\right)^n d\ln\left(\alpha\right)}{4b\eta R} \tag{8-8}$$

Using the same assumptions about the values of the parameters in this equation as above yields critical velocities of order 10^5 μm/s for the rods with aspect ratios of either 4.5 or 12. Again, this value is orders of magnitude larger than the actual freezing velocity, meaning that, like the spheres, the rods should also be easily expelled from the ice front.

It should be mentioned, however, that unlike the rods with an aspect ratio of one (i.e., nearly spherical), the true rod-like particles could display an orientation preference during transport from the ice front. In addition, the packing of the rods in the non-planar front will likely not be as efficient as with the more spherical particles. These considerations could possibly explain both the elongated pore shape and the increased roughness of the pore walls observed in Figs. 4 and 5. Another possibility is that short nanorods (aspect ratio ~4.5) can arrange into somewhat planar arrays (see Fig. 8-4c), which could result in relatively large and flat pore faces and irregular pore shapes. By comparison, longer rods (aspect ratio ~12) pack less efficiently, leading to elongated pores.

8.3.2 Increased strength from rods

In Chapters 3 and 5, it was found that adding relatively large kaolinite platelets to a silica nanoparticle suspension led to a significant increase in the mechanical strength of both the freeze-cast and sintered composites created from the suspension. The suggested reason for this increase was that the platelets were capable of distributing any applied stress over a larger portion of the sample, which would reduce the likelihood of stress being concentrated at any one

point. Such a distribution of stress would also occur with the rod-like particles, which would explain the strength results presented in Fig. 8-6.

This strategy of improving the strength of the porous materials would be benefit to most potential applications, such as separation filters, catalyst supports, microelectronics, gas distributors, insulators, and biotechnology. The added rods improve the integrity of the freeze cast composites and offer a higher strength than many other materials with either larger or smaller particles (i.e. some particles collapse right after freeze drying and bulk materials are not available). I demonstrated that this methodology works well for green composites before sintering. With proper sintering condition applied, the rod-like particle addition is supposed to further increase the strength due to enhanced bonding between nanorods and nanospheres.

8.4 Conclusions

Porous silica composites composed of silica nanoparticles and synthesized silica rods with varying aspect ratio were fabricated by freeze casting the aqueous suspensions of these materials. Through a simple analysis of the forces acting on a particle above a moving ice front, the formation of a porous microstructure could be predicted. For all of the materials used in these experiments (i.e., nanospheres or rods with aspect ratios varying from 1 to 12), the freezing velocity was orders of magnitude below the critical velocity at which particle engulfment would occur. For the rods with aspect ratio close to one (i.e., nearly spherical), the pores were found to be roughly circular and the pore walls were relatively smooth. As the aspect ratio increased, the pores became more elongated and the pore walls noticeably rougher. It is suggested that these effects could arise from a preferred orientation of the rods during expulsion from the ice front or from inefficient packing of the rods between the non-planar ice crystal fronts.

Adding the larger rods to the suspension increased the mechanical strength of the freeze-cast composite, and this effect increased as the rods became longer. This increased strength likely arises from the ability of the rods to distribute any applied stress over a larger portion of the sample.

This work demonstrates a method of modifying the porous structure and improving the strength of a composite without compromising the porosity or altering the composition. Because the interaction here is not believed to be material specific, the improvement observed in strength should also be achievable with materials other than silica. In addition, the work presented here

used rods with a maximum aspect ratio of 12. It would be interesting to see whether the observed trend of improved strength with increasing aspect ratio would be maintained for rods with much high aspect ratios (e.g., ceramic fibers).

CHAPTER 9. SUMMARY AND PERSPECTIVES

Although many efforts have been devoted to the investigation of porous materials, many existing issues, such as the need for expensive reagents/organic solvents and the lack of strength associated with increasing porosity, suggest the necessity for further exploration in this field. This dissertation focused on a unique silica-nanoparticle-based porous composite fabricated by freeze casting and sintering.

Through the experiments, a basic understanding of the freeze casting and sintering behaviors of the silica-nanoparticle-based composites has been established. During freeze casting, both kaolinite platelets and silica nanorods were able to alter the solidification behaviors of the ice fronts and subsequently modify the resulting pore morphologies. Specifically, large kaolinite platelets create large and more interconnected pores, while silica nanorod addition led to pore shape evolution (from circular, to irregular, then to elongated spherical pores) with increasing aspect ratio. Both of the anisotropic particles caused a higher roughness of the pore walls due to their inefficient packing during expulsion from the ice fronts. The specific surface area of the freeze cast composites can be precisely predicted as there is no significant area loss for any particle during freeze casting.

The sintering behavior of the silica nanoparticles were modified by kaolinite addition. The phase transformation from an amorphous structure into an α-cristobalite crystalline structure at approximately 850°C for pure silica nanoparticles was inhibited by sufficient concentrations of kaolinite platelets (roughly 4 vol% kaolinite or higher). The silica nanoparticles close enough to the kaolinite platelets were found to decrease in size during sintering, indicating diffusion between the two species occurs. When the sintering temperature was raised to 1250°C, boundaries between the two species could no longer be discerned and new features were observed in the XRD pattern, which indicated the formation of an interfacial phase with pseudo-α-cristobalite crystalline structure.

In addition to the fundamental principles, the properties of the porous composites and their relationship to the relevant factors have been evaluated. The addition of anisotropic particles can effectively improve the strength of porous composites without comprising the porosity. In the green state, the large size and inherent strength (i.e. for kaolinite) of the

anisotropic particles allowed distribution of any applied load over a much larger region of the connected network, which reduced local stresses. For the kaolinite-silica composites sintered at 1250°C, the new interfacial phase and the densified scaffold walls further increased the sample strength. At 1250°C, a ceramic containing 10 vol% kaolinite and 8 vol% silica had a strength that was 52 times greater than a ceramic containing only 18 vol% silica and 2.5 times greater than one containing only 18 vol% kaolinite, yet still being 69% porous. The initial solids loading of the suspension was found to affect the particle packing, and therefore influenced the interfacial phase formation and the strength. The flexural strength for the kaolinite-silica porous composite increased with the sintering time but decreased with the solids loading (i.e. within the range of 12 vol% to 24 vol%).

To improve the specific surface area of the porous composite while maintaining the mechanical strength, a novel method involving infiltration of an aqueous suspension containing nanoparticles into a porous scaffold, followed by freeze drying and partial sintering, was developed. By altering the size and concentration of nanoparticles infiltrated, the specific surface area could be precisely controlled from less than one to well over 100 m^2/g. Water flux tests demonstrated the potential application of the porous composite as separation membranes.

This work provided a promising method of improving the strength of a porous material/composite without compromising the porosity (or even purity). The studying system here included nothing more than silica, kaolinite, water, and salts, which are inexpensive and environmentally friendly. Because the interaction during freeze casting was not believed to be material specific, this strategy should also be applicable to materials other than silica or kaolinite. In addition, the fundamental principles learned in this dissertation are believed to be valuable for other material systems.

CHAPTER 10. FUTURE WORK

The versatile strategy and promising properties of the freeze cast silica nanoparticle-based composites suggest a promising future for continued study. Future work could develop along two fronts: optimizing the properties of these composites to facilitate applications, or exploiting the method to other materials.

In this dissertation, I described fundamental principles and pointed out ways to improve the physical properties of the silica-nanoparticle-based composites. However, efforts have not been devoted to optimize the properties. For example, the specific surface area can be further improved up to 200 m^2/g by utilizing smaller nanoparticles, the pore size can be further reduced by continuing suspension infiltration beyond five steps, and the silica nanorod-nanosphere composite can be strengthened by partial sintering. On the other hand, some of the properties compete with each other, such as permeability vs. specific surface area, strength vs. porosity, and strength vs. specific surface area. Therefore, before use in any applications, the porous composite must be carefully designed to optimize parameters for specific fields.

In this study, only disk-like composite samples were prepared. Although freeze casting is notable for fabricating samples with complex geometries, technical issues (e.g. demold, microstructure homogeneity, drying) arise when samples are of large dimensions and complicated shapes.

Since the potential use as liquid membranes was demonstrated in this dissertation, future work could also focus on the exploration of ceramic separation membranes. Such investigations could development of a tube-like scaffold, depositing the nanoparticles on only an 'active' thin layer, and functionalizing the silica surfaces.

The other approach would be to apply the strategy to other functional materials (e.g. TiO_2, ZnO). The scaffolds can either be made of TiO_2/ZnO nanoparticles or coated by those nanoparticles by suspension infiltration. This design should be able to broaden the applications in such fields as photocatalysis, biotechnology, and solid state fuel cell.

REFERENCES

1. X. B. Ke, H. Y. Zhu, X. P. Gao, J. W. Liu, and Z. F. Zheng: 'High-performance ceramic membranes with a separation layer of metal oxide nanofibers', *Adv Mater*, 2007, **19**(6), 785-790.
2. H. W. Liang, L. Wang, P. Y. Chen, H. T. Lin, L. F. Chen, D. A. He, and S. H. Yu: 'Carbonaceous nanofiber membranes for selective filtration and separation of nanoparticles', *Adv Mater*, 2010, **22**(42), 4691-4695.
3. M. M. Pendergast and E. M. V. Hoek: 'A review of water treatment membrane nanotechnologies', *Energ Environ Sci*, 2011, **4**(6), 1946-1971.
4. P. Colombo, C. Vakifahmetoglu, and S. Costacurta: 'Fabrication of ceramic components with hierarchical porosity', *J Mater Sci*, 2010, **45**(20), 5425-5455.
5. M. E. Davis: 'Ordered porous materials for emerging applications', *Nature*, 2002, **417**(6891), 813-821.
6. R. D. Miller: 'Device physics - In search of low-k dielectrics', *Science*, 1999, **286**(5439), 421-423.
7. A. C. Patel, S. X. Li, J. M. Yuan, and Y. Wei: 'In situ encapsulation of horseradish peroxidase in electrospun porous silica fibers for potential biosensor applications', *Nano Lett*, 2006, **6**(5), 1042-1046.
8. B. J. Scott, G. Wirnsberger, and G. D. Stucky: 'Mesoporous and mesostructured materials for optical applications', *Chem Mater*, 2001, **13**(10), 3140-3150.
9. I. I. Slowing, B. G. Trewyn, S. Giri, and V. S. Y. Lin: 'Mesoporous silica nanoparticles for drug delivery and biosensing applications', *Adv Funct Mater*, 2007, **17**(8), 1225-1236.
10. A. H. Lu and F. Schuth: 'Nanocasting: A versatile strategy for creating nanostructured porous materials', *Adv Mater*, 2006, **18**(14), 1793-1805.
11. S. Deville: 'Freeze-casting of porous ceramics: A review of current achievements and issues', *Adv Eng Mater*, 2008, **10**(3), 155-169.
12. F. Caruso, R. A. Caruso, and H. Mohwald: 'Nanoengineering of inorganic and hybrid hollow spheres by colloidal templating', *Science*, 1998, **282**(5391), 1111-1114.

13. A. Herzog, R. Klingner, U. Vogt, and T. Graule: 'Wood-derived porous SiC ceramics by sol infiltration and carbothermal reduction', *J Am Ceram Soc*, 2004, **87**(5), 784-793.
14. P. Sepulveda and J. G. P. Binner: 'Processing of cellular ceramics by foaming and in situ polymerisation of organic monomers', *J Eur Ceram Soc*, 1999, **19**(12), 2059-2066.
15. S. Deville, E. Saiz, and A. P. Tomsia: 'Freeze casting of hydroxyapatite scaffolds for bone tissue engineering', *Biomaterials*, 2006, **27**(32), 5480-5489.
16. T. Uchino: 'Structure and properties of amorphous silica and its related materials: Recent developments and future directions', *J Ceram Soc Jpn*, 2005, **113**(1313), 17-25.
17. H. H. Yang, S. Q. Zhang, X. L. Chen, Z. X. Zhuang, J. G. Xu, and X. R. Wang: 'Magnetite-containing spherical silica nanoparticles for biocatalysis and bioseparations', *Anal Chem*, 2004, **76**(5), 1316-1321.
18. M. Qhobosheane, S. Santra, P. Zhang, and W. H. Tan: 'Biochemically functionalized silica nanoparticles', *Analyst*, 2001, **126**(8), 1274-1278.
19. F. Torney, B. G. Trewyn, V. S. Y. Lin, and K. Wang: 'Mesoporous silica nanoparticles deliver DNA and chemicals into plants', *Nat Nanotechnol*, 2007, **2**(5), 295-300.
20. A. Burns, H. Ow, and U. Wiesner: 'Fluorescent core-shell silica nanoparticles: towards "Lab on a Particle" architectures for nanobiotechnology', *Chem Soc Rev*, 2006, **35**(11), 1028-1042.
21. J. Eastoe, M. J. Hollamby, and L. Hudson: 'Recent advances in nanoparticle synthesis with reversed micelles', *Adv Colloid Interfac*, 2006, **128**, 5-15.
22. D. G. Shchukin and G. B. Sukhorukov: 'Nanoparticle synthesis in engineered organic nanoscale reactors', *Adv Mater*, 2004, **16**(8), 671-682.
23. R. Mueller, L. Madler, and S. E. Pratsinis: 'Nanoparticle synthesis at high production rates by flame spray pyrolysis', *Chem Eng Sci*, 2003, **58**(10), 1969-1976.
24. G. Cao: 'Nanostructures and nanomaterials: Synthesis, properties and applications', 2004, Imperial College Press, Covent Garden, London.
25. B. G. Trewyn, I. I. Slowing, S. Giri, H. T. Chen, and V. S. Y. Lin: 'Synthesis and functionalization of a mesoporous silica nanoparticle based on the sol-gel process and applications in controlled release', *Accounts Chem Res*, 2007, **40**(9), 846-853.

26. M. W. Ambrogio, C. R. Thomas, Y. L. Zhao, J. I. Zink, and J. F. Stoddartt: 'Mechanized silica nanoparticles: A new frontier in theranostic nanomedicine', *Accounts Chem Res*, 2011, **44**(10), 903-913.
27. K. Dick, T. Dhanasekaran, Z. Y. Zhang, and D. Meisel: 'Size-dependent melting of silica-encapsulated gold nanoparticles', *J Am Chem Soc*, 2002, **124**(10), 2312-2317.
28. F. Q. Tang, L. L. Li, and D. Chen: 'Mesoporous silica nanoparticles: synthesis, biocompatibility and drug delivery', *Adv Mater*, 2012, **24**(12), 1504-1534.
29. J. F. Wang, J. P. Zhang, B. Y. Asoo, and G. D. Stucky: 'Structure-selective synthesis of mesostructured/mesoporous silica nanofibers', *J Am Chem Soc*, 2003, **125**(46), 13966-13967.
30. J. F. Wang, C. K. Tsung, R. C. Hayward, Y. Y. Wu, and G. D. Stucky: 'Single-crystal mesoporous silica ribbons', *Angewandte Chemie-International Edition*, 2005, **44**(2), 332-336.
31. A. Kuijk, A. van Blaaderen, and A. Imhof: 'Synthesis of monodisperse, rodlike silica colloids with tunable aspect ratio', *J Am Chem Soc*, 2011, **133**(8), 2346-2349.
32. X. B. Ke, H. Y. Zhu, X. P. Gao, J. W. Liu, and Z. F. Zheng: 'High-performance ceramic membranes with a separation layer of metal oxide nanofibers', *Adv Mater*, 2007, **19**(6), 785-790.
33. J. C. Baird and J. Y. Walz: 'The effects of added nanoparticles on aqueous kaolinite suspensions I. Structural effects', *J Colloid Interf Sci*, 2006, **297**(1), 161-169.
34. W. A. Deer, R. A. Howie, and J. Zussman: 'An introduction to the rock-forming minerals', 1992, Harlow: Longman.
35. V. Gupta, A. H. Marc, A. V. Nguyen, and J. D. Miller: 'Crystal lattice imaging of the silica and alumina faces of kaolinite using atomic force microscopy', *J Colloid Interf Sci*, 2010, **352**(1), 75-80.
36. H. V. Olphen: 'An introduction to clay colloid chemistry: for clay technologists, geologists, and soil scientists'; 1977, New York, Wiley.
37. W. M. Carty: 'The colloidal nature of kaolinite', *Am Ceram Soc Bull*, 1999, **78**(8), 72-76.
38. J. Lemaitre and B. Delmon: 'Study of sintering mechanism of kaolinite at 900 and 1050-degrees-C-influence of mineralizers', *J Mater Sci*, 1977, **12**(10), 2056-2064.

39. M. Bulens and B. Delmon: 'Kinetic control of formation of high-temperature phases in kaolinite-mullite reaction sequence', *B Soc Chim Belg*, 1977, **86**(6), 405-411.
40. M. Bellotto, A. Gualtieri, G. Artioli, and S. M. Clark: 'Kinetic-study of the kaolinite-mullite reaction sequence. 1. Kaolinite dehydroxylation', *Phys Chem Miner*, 1995, **22**(4), 207-214.
41. A. Gualtieri, M. Bellotto, G. Artioli, and S. M. Clark: 'Kinetic-study of the kaolinite-mullite reaction sequence. 2. Mullite formation', *Phys Chem Miner*, 1995, **22**(4), 215-222.
42. V. Viswabaskaran, F. D. Gnanam, and M. Balasubramanian: 'Effect of MgO,Y_2O_3 and boehmite additives on the sintering behaviour of mullite formed from kaolinite-reactive alumina', *J Mater Process Tech*, 2003, **142**(1), 275-281.
43. C. Y. Chen, G. S. Lan, and W. H. Tuan: 'Preparation of mullite by the reaction sintering of kaolinite and alumina', *J Eur Ceram Soc*, 2000, **20**(14-15), 2519-2525.
44. Y. F. Liu, X. Q. Liu, S. W. Tao, G. Y. Meng, and O. T. Sorensen: 'Kinetics of the reactive sintering of kaolinite-aluminum hydroxide extrudate', *Ceram Int*, 2002, **28**(5), 479-486.
45. H. R. Rezaie, W. M. Rainforth, and W. E. Lee: 'Mullite evolution in ceramics derived from kaolinite, kaolinite with added alpha-alumina, and sol-gel precursors', *Brit Ceram T*, 1997, **96**(5), 181-187.
46. K. Shih and J. O. Leckie: 'Nickel aluminate spinel formation during sintering of simulated Ni-laden sludge and kaolinite', *J Eur Ceram Soc*, 2007, **27**(1), 91-99.
47. M. Panneerselvam and K. J. Rao: 'Novel microwave method for the synthesis and sintering of mullite from kaolinite', *Chem Mater*, 2003, **15**(11), 2247-2252.
48. K. H. Yang, J. H. Wu, C. S. Hsi, and H. Y. Lu: 'Morphologically textured mullite in sintered tape-cast kaolin', *J Am Ceram Soc*, 2011, **94**(3), 938-944.
49. H. R. Baharvandi and A. M. Hadian: 'Investigation on addition of kaolinite on sintering behavior and mechanical properties of B_4C', *J Mater Eng Perform*, 2009, **18**(4), 433-437.
50. W. Li, K. Lu, and J. Y. Walz: 'Freeze casting of porous materials: review of critical factors in microstructure evolution', *Int Mater Rev*, 2012, **57**(1), 37-60.
51. T. Moritz and H. J. Richter: 'Ice-mould freeze casting of porous ceramic components', *J Eur Ceram Soc*, 2007, **27**(16), 4595-4601.

52. K. H. Zuo, Y. P. Zeng, and D. L. Jiang: 'Properties of microstructure-controllable porous yttria-stabilized ziroconia ceramics fabricated by freeze casting', *Int J Appl Ceram Tec*, 2008, **5**(2), 198-203.
53. X. W. Zhu, D. L. Jiang, S. H. Tan, and Z. Q. Zhang: 'Improvement in the strut thickness of reticulated porous ceramics', *J Am Ceram Soc*, 2001, **84**(7), 1654-1656.
54. K. Araki and J. W. Halloran: 'Porous ceramic bodies with interconnected pore channels by a novel freeze casting technique', *J Am Ceram Soc*, 2005, **88**(5), 1108-1114.
55. H. Yoshikawa, N. Tamai, T. Murase, and A. Myoui: 'Interconnected porous hydroxyapatite ceramics for bone tissue engineering', *J R Soc Interface*, 2009, **6**, S341-S348.
56. H. Lu, Z. Qu, and Y. C. Zhou: 'Preparation and mechanical properties of dense polycrystalline hydroxyapatite through freeze-drying', *J Mater Sci-Mater M*, 1998, **9**(10), 583-587.
57. S. W. Sofie and F. Dogan: 'Freeze casting of aqueous alumina slurries with glycerol', *J Am Ceram Soc*, 2001, **84**(7), 1459-1464.
58. J. Laurie, C. M. Bagnall, B. Harris, R. W. Jones, R. G. Cooke, R. S. Russellfloyd, T. H. Wang, and F. W. Hammett: 'Colloidal suspensions for the preparation of ceramics by a freeze casting route', *J Non-Cryst Solids*, 1992, **147**, 320-325.
59. K. Araki and J. W. Halloran: 'Room-temperature freeze casting for ceramics with nonaqueous sublimable vehicles in the naphthalene-camphor eutectic system', *J Am Ceram Soc*, 2004, **87**(11), 2014-2019.
60. R. F. Chen, C. A. Wang, Y. Huang, L. G. Ma, and W. Y. Lin: 'Ceramics with special porous structures fabricated by freeze-gelcasting: Using tert-butyl alcohol as a template', *J Am Ceram Soc*, 2007, **90**(11), 3478-3484.
61. Y. Chino and D. C. Dunand: 'Directionally freeze-cast titanium foam with aligned, elongated pores', *Acta Mater*, 2008, **56**(1), 105-113.
62. S. A. Barr and E. Luijten: 'Structural properties of materials created through freeze casting', *Acta Mater*, 2010, **58**(2), 709-715.
63. C. Korber, G. Rau, M. D. Cosman, and E. G. Cravalho: 'Interaction of particles and a moving ice-liquid interface', *J Cryst Growth*, 1985, **72**(3), 649-662.

64. S. S. L. Peppin, M. G. Worster, and J. S. Wettlaufer: 'Morphological instability in freezing colloidal suspensions', *P R Soc A*, 2007, **463**, 723-733.
65. S. S. L. Peppin, J. A. W. Elliott, and M. G. Worster: 'Solidification of colloidal suspensions', *J Fluid Mech*, 2006, **554**, 147-166.
66. W. W. Mullins and R. F. Sekerka: 'Stability of a planar interface during solidification of a dilute binary alloy', *J Appl Phys*, 1964, **35**(2), 444-451.
67. P. Casses and M. A. Azouniaidi: 'A General Theoretical approach to the behavior of foreign particles at advancing solid-liquid interfaces', *Adv Colloid Interfac*, 1994, **50**, 103-120.
68. A. W. Rempel and M. G. Worster: 'Particle trapping at an advancing solidification front with interfacial-curvature effects', *J Cryst Growth*, 2001, **223**(3), 420-432.
69. R. Trivedi and K. Somboonsuk: 'Pattern-formation during the directional solidification of binary-systems', *Acta Metall Mater*, 1985, **33**(6), 1061-1068.
70. R. Trivedi: 'Theory of dendritic growth during the directional solidification of binary-alloys', *J Cryst Growth*, 1980, **49**(2), 219-232.
71. W. Kurz and R. Trivedi: 'Solidification microstructures--recent developments and future-directions', *Acta Metallurgica Et Materialia*, 1990, **38**(1), 1-17.
72. W. J. Boettinger, S. R. Coriell, A. L. Greer, A. Karma, W. Kurz, M. Rappaz, and R. Trivedi: 'Solidification microstructures: Recent developments, future directions', *Acta Mater*, 2000, **48**(1), 43-70.
73. J. A. Sekhar and R. Trivedi: 'Solidification microstructure evolution in the presence of inert particles', *Mat Sci Eng a-Struct*, 1991, **147**(1), 9-21.
74. M. Asta, C. Beckermann, A. Karma, W. Kurz, R. Napolitano, M. Plapp, G. Purdy, M. Rappaz, and R. Trivedi: 'Solidification microstructures and solid-state parallels: Recent developments, future directions', *Acta Mater*, 2009, **57**(4), 941-971.
75. J. J. Hoyt, M. Asta, and A. Karma: 'Atomistic and continuum modeling of dendritic solidification', *Mat Sci Eng R*, 2003, **41**(6), 121-163.
76. A. W. Rempel and M. G. Worster: 'The interaction between a particle and an advancing solidification front', *J Cryst Growth*, 1999, **205**(3), 427-440.
77. C. A. Knight: 'Ice nucleation in the atmosphere', *Adv Colloid Interfac*, 1979, **10**, 369-395.

78. V. Y. Smorodin: 'Mechanisms of heterogeneous ice nucleation onto mixed ice nuclei in the atmosphere', *J Aerosol Sci*, 1990, **21**, S249-S253.
79. V. F. Petrenko and R. W. Whitworth: 'Physics of ice', 2006, Oxford University Press, Oxford.
80. L. Granasy and D. W. Oxtoby: 'Cahn-Hilliard theory with triple-parabolic free energy. II. Nucleation and growth in the presence of a metastable crystalline phase', *J Chem Phys*, 2000, **112**(5), 2410-2419.
81. S. Bauerecker, P. Ulbig, V. Buch, L. Vrbka, and P. Jungwirth: 'Monitoring ice nucleation in pure and salty water via high-speed imaging and computer simulations', *J Phys Chem C*, 2008, **112**(20), 7631-7636.
82. E. A. L. Levi, L. Lubart: 'Structure of ice grown from droplet accretion and solidification process', *J Cryst Growth*, 1974, **22**(4), 303-310.
83. M. C. Gutierrez, M. L. Ferrer, and F. del Monte: 'Ice-templated materials: Sophisticated structures exhibiting enhanced functionalities obtained after unidirectional freezing and ice-segregation-induced self-assembly', *Chem Mater*, 2008, **20**(3), 634-648.
84. S. Deville, E. Maire, A. Lasalle, A. Bogner, C. Gauthier, J. Leloup, and C. Guizard: 'In situ X-ray radiography and tomography observations of the solidification of aqueous alumina particle suspensions-Part I: Initial instants', *J Am Ceram Soc*, 2009, **92**(11), 2489-2496.
85. S. Deville, E. Maire, A. Lasalle, A. Bogner, C. Gauthier, J. Leloup, and C. Guizard: 'In situ X-ray radiography and tomography observations of the solidification of aqueous alumina particles suspensions. Part II: Steady state', *J Am Ceram Soc*, 2009, **92**(11), 2497-2503.
86. E. R. Rubinstein and M. E. Glicksman: 'Dendritic growth-kinetics and structure. 2. camphene', *J Cryst Growth*, 1991, **112**(1), 97-110.
87. S. Deville, E. Saiz, and A. P. Tomsia: 'Ice-templated porous alumina structures', *Acta Mater*, 2007, **55**(6), 1965-1974.
88. E. Munch, E. Saiz, A. P. Tomsia, and S. Deville: 'Architectural control of freeze-cast ceramics through additives and templating', *J Am Ceram Soc*, 2009, **92**(7), 1534-1539.

89. A. Szepes, A. Feher, P. Szabo-Revesz, and J. Ulrich: 'Influence of freezing temperature on product parameters of solid dosage forms prepared via the freeze-casting technique', *Chem Eng Technol*, 2007, **30**(4), 511-516.

90. S. W. Sofie: 'Fabrication of functionally graded and aligned porosity in thin ceramic substrates with the novel freeze-tape-casting process', *J Am Ceram Soc*, 2007, **90**(7), 2024-2031.

91. C. T. McKee and J. Y. Walz: 'Effects of added clay on the properties of freeze-casted composites of silica nanoparticles', *J Am Ceram Soc*, 2009, **92**(4), 916-921.

92. K. Lu, C. Hammond, and J. M. Qian: 'Surface patterning nanoparticle-based arrays', *J Mater Sci*, 2010, **45**(3), 582-588.

93. L. Qian and H. F. Zhang: 'Controlled freezing and freeze drying: a versatile route for porous and micro-/nano-structured materials', *J Chem Technol Biot*, 2011, **86**(2), 172-184.

94. D. Koch, L. Andresen, T. Schmedders, and G. Grathwohl: 'Evolution of porosity by freeze casting and sintering of sol-gel derived ceramics', *J Sol-Gel Sci Techn*, 2003, **26**(1-3), 149-152.

95. N. Pachulski and J. Ulrich: 'Production of tablet-like solid bodies without pressure by sol-gel processes', *Lett Drug Des Discov*, 2007, **4**(1), 78-81.

96. T. Waschkies, R. Oberacker, and M. J. Hoffmann: 'Control of lamellae spacing during freeze casting of ceramics using double-side cooling as a novel processing route', *J Am Ceram Soc*, 2009, **92**(1), S79-S84.

97. G. Liu, D. Zhang, C. Meggs, and T. W. Button: 'Porous Al_2O_3-ZrO_2 composites fabricated by an ice template method', *Scripta Mater*, 2010, **62**(7), 466-468.

98. E. Munch, J. Franco, S. Deville, P. Hunger, E. Saiz, and A. P. Tomsia: 'Porous ceramic scaffolds with complex architectures', *Jom-Us*, 2008, **60**(6), 54-58.

99. L. L. Ren, Y. P. Zeng, and D. L. Jiang: 'Fabrication of gradient pore TiO_2 sheets by a novel freeze-tape-casting process', *J Am Ceram Soc*, 2007, **90**(9), 3001-3004.

100. S. Deville, E. Maire, A. Lasalle, A. Bogner, C. Gauthier, J. Leloup, and C. Guizard: 'Influence of particle size on ice nucleation and growth during the ice-templating process', *J Am Ceram Soc*, 2010, **93**(9), 2507-2510.

101. Q. Fu, M. N. Rahaman, F. Dogan, and B. S. Bal: 'Freeze casting of porous hydroxyapatite scaffolds. I. Processing and general microstructure', *J Biomed Mater Res B*, 2008, **86B**(1), 125-135.
102. Q. Fu, M. N. Rahaman, F. Dogan, and B. S. Bal: 'Freeze casting of porous hydroxyapatite scaffolds. II. Sintering, microstructure, and mechanical behavior', *J Biomed Mater Res B*, 2008, **86B**(2), 514-522.
103. Y. M. Zhang, L. Y. Hu, J. C. Han, and Z. H. Jiang: 'Freeze casting of aqueous alumina slurries with glycerol for porous ceramics', *Ceram Int*, 2010, **36**(2), 617-621.
104. M. N. Rahaman and Q. Fu: 'Manipulation of porous bioceramic microstructures by freezing of suspensions containing binary mixtures of solvents', *J Am Ceram Soc*, 2008, **91**(12), 4137-4140.
105. Q. Fu, M. N. Rahaman, F. Dogan, and B. S. Bal: 'Freeze-cast hydroxyapatite scaffolds for bone tissue engineering applications', *Biomed Mater*, 2008, **3**(2) 1-7.
106. K. Lu: 'Microstructural evolution of nanoparticle aqueous colloidal suspensions during freeze casting', *J Am Ceram Soc*, 2007, **90**(12), 3753-3758.
107. N. Pachulski and J. Ulrich: 'New fields of application for sol-gel processes - Cold and vacuum-free 'compacting' of pharmaceutical materials to tablets', *Chem Eng Res Des*, 2007, **85**(A7), 1013-1019.
108. K. Lu and X. J. Zhu: 'Freeze casting as a nanoparticle material-forming method', *Int J Appl Ceram Tec*, 2008, **5**(3), 219-227.
109. Y. Zhang, K. Zuo, and Y. P. Zeng: 'Effects of gelatin addition on the microstructure of freeze-cast porous hydroxyapatite cerarmics', *Ceram Int*, 2009, **35**(6), 2151-2154.
110. K. H. Zuo, Y. P. Zeng, and D. L. Jiang: 'Effect of polyvinyl alcohol additive on the pore structure and morphology of the freeze-cast hydroxyapatite ceramics', *Mat Sci Eng C-Mater*, 2010, **30**(2), 283-287.
111. L. L. Ren, Y. P. Zeng, and D. L. Jiang: 'Preparation of porous TiO_2 by a novel freeze casting', *Ceram Int*, 2009, **35**(3), 1267-1270.
112. C. M. Pekor, P. Kisa, and I. Nettleship: 'Effect of polyethylene glycol on the microstructure of freeze-cast alumina', *J Am Ceram Soc*, 2008, **91**(10), 3185-3190.

113. Y. M. Zhang, L. Y. Hu, and J. C. Han: 'Preparation of a dense/porous biLayered ceramic by applying an electric field during freeze casting', *J Am Ceram Soc*, 2009, **92**(8), 1874-1876.
114. K. Nakagawa, N. Thongprachan, T. Charinpanitkul, and W. Tanthapanichakoon: 'Ice crystal formation in the carbon nanotube suspension: A modelling approach', *Chem Eng Sci*, 2010, **65**(4), 1438-1451.
115. N. N. Zhang, H. X. Qiu, Y. M. Si, W. Wang, and J. P. Gao: 'Fabrication of highly porous biodegradable monoliths strengthened by graphene oxide and their adsorption of metal ions', *Carbon*, 2011, **49**(3), 827-837.
116. R. M. German: 'Sintering theory and practice', 1996, Wiley-Interscience, New York.
117. Z. Z. Fang and H. Wang: 'Densification and grain growth during sintering of nanosized particles', *Int Mater Rev*, 2008, **53**(6), 326-352.
118. C. T. Campbell, S. C. Parker, and D. E. Starr: 'The effect of size-dependent nanoparticle energetics on catalyst sintering', *Science*, 2002, **298**(5594), 811-814.
119. K. K. Nanda, A. Maisels, F. E. Kruis, H. Fissan, and S. Stappert: 'Higher surface energy of free nanoparticles', *Phys Rev Lett*, 2003, **91**(10).
120. Z. Fang, P. Maheshwari, X. Wang, H. Y. Sohn, A. Griffo, and R. Riley: 'An experimental study of the sintering of nanocrystalline WC-Co powders', *Int J Refract Met H*, 2005, **23**(4-6), 249-257.
121. Z. J. Shen, H. Peng, J. Liu, and M. Nygren: 'Conversion from nano- to micron-sized structures: experimental observations', *J Eur Ceram Soc*, 2004, **24**(12), 3447-3452.
122. M. J. Mayo, D. C. Hague, and D. J. Chen: 'Processing nanocrystalline ceramics for applications in superplasticity', *Mat Sci Eng a-Struct*, 1993, **166**(1-2), 145-159.
123. G. Skandan, H. Hahn, B. H. Kear, M. Roddy, and W. R. Cannon: 'The effect of applied stress on densification of nanostructured zirconia during sinter-forging', *Mater Lett*, 1994, **20**(5-6), 305-309.
124. S. H. Risbud, C. H. Shan, A. K. Mukherjee, M. J. Kim, J. S. Bow, and R. A. Holl: 'Retention of nanostructure in aluminum-oxide by very rapid sintering at 1150-degrees-C', *J Mater Res*, 1995, **10**(2), 237-239.
125. K. Lu: 'Sintering of nanoceramics', *Int Mater Rev*, 2008, **53**(1), 21-38.

126. J. R. Groza and A. Zavaliangos: 'Sintering activation by external electrical field', *Mat Sci Eng a-Struct*, 2000, **287**(2), 171-177.
127. M. N. Rahaman: 'Ceramic Processing', 2007, Taylor & Francis, Boca Raton.
128. X. H. Wang, P. L. Chen, and I. W. Chen: 'Two-step sintering of ceramics with constant grain-size, I. Y_2O_3', *J Am Ceram Soc*, 2006, **89**(2), 431-437.
129. S. K. K. Ishizaki, M. Nanko: 'Porous Materials: Process technology and applications', 1998, Kluwer Academic Publishers, Boston.
130. F. Q. Tang, H. Fudouzi, T. Uchikoshi, and Y. Sakka: 'Preparation of porous materials with controlled pore size and porosity', *J Eur Ceram Soc*, 2004, **24**(2), 341-344.
131. H. S. Cruz, J. Spino, and G. Grathwohl: 'Nanocrystalline ZrO_2 ceramics with idealized macropores', *J Eur Ceram Soc*, 2008, **28**(9), 1783-1791.
132. F. Tang, H. Fudouzi, T. Uchikoshi, T. Awane, and Y. Sakka: 'Fabrication of ordered macroporous structures based on hetero-coagulation process using nanoparticle as building blocks', *Chem Lett*, 2003, **32**(3), 276-277.
133. D. Chakravarty, H. Ramesh, and T. N. Rao: 'High strength porous alumina by spark plasma sintering', *J Eur Ceram Soc*, 2009, **29**(8), 1361-1369.
134. M. Demertzis and N. P. Evmiridis: 'Potentials of ion-exchanged synthetic zeolite-polymer membranes', *J Chem Soc Farad T 1*, 1986, **82**, 3647-3655.
135. G. Gu, M. Schmid, P. W. Chiu, A. Minett, J. Fraysse, G. T. Kim, S. Roth, M. Kozlov, E. Munoz, and R. H. Baughman: 'V_2O_5 nanofibre sheet actuators', *Nat Mater*, 2003, **2**(5), 316-319.
136. Z. B. Wang, A. P. Mitra, H. T. Wang, L. M. Huang, and Y. S. Yan: 'Pure silica zeolite films as low-k dielectrics by spin-on of nanoparticle suspensions', *Adv Mater*, 2001, **13**(19), 1463-1466.
137. Z. B. Wang, H. T. Wang, A. Mitra, L. M. Huang, and Y. S. Yan: 'Pure-silica zeolite low-k dielectric thin films', *Adv Mater*, 2001, **13**(10), 746-749.
138. J. K. Yuan, X. G. Liu, O. Akbulut, J. Q. Hu, S. L. Suib, J. Kong, and F. Stellacci: 'Superwetting nanowire membranes for selective absorption', *Nat Nanotechnol*, 2008, **3**(6), 332-336.

139. Y. M. Wang, G. J. Du, H. Liu, D. Liu, S. B. Qin, N. Wang, C. G. Hu, X. T. Tao, J. Jiao, J. Y. Wang, and Z. L. Wang: 'Nanostructured sheets of Ti-O nanobelts for gas sensing and antibacterial applications', *Adv Funct Mater*, 2008, **18**(7), 1131-1137.
140. I. G. Giannakopoulos, D. Kouzoudis, C. A. Grimes, and V. Nikolakis: 'Synthesis and characterization of a composite zeolite-metglas carbon dioxide sensor', *Adv Funct Mater*, 2005, **15**(7), 1165-1170.
141. T. Bein: 'Synthesis and applications of molecular sieve layers and membranes', *Chem Mater*, 1996, **8**(8), 1636-1653.
142. G. Calzaferri, M. Pauchard, H. Maas, S. Huber, A. Khatyr, and T. Schaafsma: 'Photonic antenna system for light harvesting, transport and trapping', *J Mater Chem*, 2002, **12**(1), 1-13.
143. W. Li, K. Lu, and J. Y. Walz: 'Formation, structure and properties of freeze-cast kaolinite-silica nanocomposites', *J Am Ceram Soc*, 2011, **94**(4), 1256-1264.
144. M. Tourbin and C. Frances: 'Monitoring of the aggregation process of dense colloidal silica suspensions in a stirred tank by acoustic spectroscopy', *Powder Technol*, 2009, **190**(1-2), 25-30.
145. M. Tourbin and C. Frances: 'A survey of complementary methods for the characterization of dense colloidal silica', *Part Part Syst Char*, 2007, **24**(6), 411-423.
146. ASTM Designation C1499–04 American society for testing and materials international, 2004, West Conshocken, PA.
147. S. Lobo-Guerrero: 'The elastic moduli of soils with disperesed oversize particles', 2002, PhD Thesis, University of Pittsburgh, PA.
148. M. Arnold, A. R. Boccaccini, and G. Ondracek: 'Prediction of the Poisson's ratio of porous materials', *J Mater Sci*, 1996, **31**(6), 1643-1646.
149. J. C. Baird and J. Y. Walz: 'The effects of added nanoparticles on aqueous kaolinite suspensions II. Rheological effects', *J Colloid Interf Sci*, 2007, **306**(2), 411-420.
150. W. Li, K. Lu, and J. Y. Walz: 'Effects of added kaolinite on sintering of freeze-cast kaolinite-silica nanocomposite I. Microstructure and phase transformation', *J Am Ceram Soc*, 2012, **95**(3), 883-891.

151. R. A. Nyquist, R. O. Kagel, C. L. Putziq and M. A. Leugers: 'The handbook of infrared and raman spectra of inorganic compounds and organic salts', 1997, Academic Press ,San Diego.
152. J. A. Gadsden: 'Infrared spectra of minerals and related inorganic compounds', 1975, London: Butterworths.
153. R. K. Case SW: 'Fatigue of composite materials. In: Ritchie RO, Murakami Y (eds) Comprehensive structural integrity, vol 4', 2003, Elsevier Pergamon, San Diego.
154. M. F: 'Fatigure behavior of short fiber composite materials. In: Reifsnider KL (ed) Composite materials series: fatigure of composites, vol 4', 1990, Elsevier, New York**.**
155. C. K. Yoon and I. W. Chen: 'Superplastic flow of 2-phase ceramics containing rigid inclusions-zirconia mullite composites', *J Am Ceram Soc*, 1990, **73**(6), 1555-1565.
156. P. F. Becher and T. N. Tiegs: 'Toughening behavior involving multiple mechanisms-Whisker reinforcement and zirconia toughening', *J Am Ceram Soc*, 1987, **70**(9), 651-654.
157. A. Petersson and J. Agren: 'Rearrangement and pore size evolution during WC-Co sintering below the eutectic temperature', *Acta Mater*, 2005, **53**(6), 1673-1683.
158. E. A. Olevsky: 'Theory of sintering: from discrete to continuum', *Mat Sci Eng R*, 1998, **23**(2), 41-100.
159. Z. D. Hendren, J. Brant, and M. R. Wiesner: 'Surface modification of nanostructured ceramic membranes for direct contact membrane distillation', *J Membrane Sci*, 2009, **331**(1-2), 1-10.
160. A. Majouli, S. Tahiri, S. A. Younssi, H. Loukili, and A. Albizane: 'Elaboration of new tubular ceramic membrane from local Moroccan Perlite for microfiltration process. Application to treatment of industrial wastewaters', *Ceram Int*, 2012, **38**(5), 4295-4303.
161. H. Ledbetter, S. Kim, and D. Balzar: 'Elastic properties of mullite', *J Am Ceram Soc*, 1998, **81**(4), 1025-1028.
162. D. R. Uhlmann, B. Chalmers and K. A. Jackson: 'Interaction between particles and a solid-liquid interface', *J. Appl. Phys.*, 1964, **35**(10), 2986-2993.
163. L. Hadji and A. M. J. Davis: 'The influence of insoluble spherical particles on the stability of a planar solidifying interface', *J Cryst Growth*, 1998, **191**(4), 889-896.
164. L. Hadji: 'Morphological instability induced by the interaction of a particle with a solid-liquid interface', *Eur Phys J B*, 2004, **37**(1), 85-89.

165. P. Aubourg: 'Interaction of second-phase particles with a crystal growing from the melt', *PhD Thesis*, 1978, Massachusetts Institute of Technology, Cambridge, MA.

166. M. D. a. S. F. Edwards: 'The theory of polymer dynamics; pp 295-6. In: The international series of monographs on physics'. Edited by R. K. Adair, R. J. Elliott, H. Ehrenreich, C. H. Llewellyn Smith, W. Marshall, and M. Rees, 1986, Oxford University Press, New York.

167. J. T. Padding and W. J. Briels: 'Translational and rotational friction on a colloidal rod near a wall', *J Chem Phys*, 2010, **132**(5).